Charge, Spin and Pseudospin in Graphene

by

Dmitry A. Abanin

Submitted to the Department of Physics
in partial fulfillment of the requirements for the degree of

Doctor of Philosophy

at the

MASSACHUSETTS INSTITUTE OF TECHNOLOGY

September 2008

© Massachusetts Institute of Technology 2008. All rights reserved.

Author .....
Department of Physics
August 5, 2008

Certified by .....
Leonid S. Levitov
Professor of Physics
Thesis Supervisor

Accepted by .....
Thomas J. Greytak
Associate Department Head for Education

ARCHIVES

MASSACHUSETTS INSTITUTE OF TECHNOLOGY
OCT 09 2008
LIBRARIES

Charge, Spin and Pseudospin in Graphene

by

Dmitry A. Abanin

Submitted to the Department of Physics
on August 5, 2008, in partial fulfillment of the
requirements for the degree of
Doctor of Philosophy

Abstract

Graphene, a one-atom-thick form of carbon, has emerged in the last few years as a fertile electron system, highly promising for both fundamental research and applications. In this thesis we consider several topics in electronic and spin properties of graphene, with a particular emphasis on the quantum Hall effect (QHE) regime, where this material exhibits most interesting behavior.

We shall start with analyzing general properties of the two-terminal conductance for graphene mono- and bilayer samples. Using conformal invariance and the theory of conformal mappings, we characterize the dependence of conductance on the sample shape. We identify the features which distinguish monolayers and bilayers and illustrate the use of the two-terminal conductance as a tool for sample diagnostic.

Next, we present a microscopic study of the edge states in the QHE regime. This analysis provides a simple and general explanation of the half-integer Hall quantization in graphene. We discuss the edge states dispersion for different orientations of the boundary, and propose a way to image the edge states using STM spectroscopy.

Then, we extend the picture of edge states to describe QHE in spatially nonuniform systems, recently demonstrated p-n and p-n-p devices. We show that the bipolar p-n and p-n-p junctions can host counter-circulating QHE edge states, which mix at the p-n interfaces, giving rise to fractional and integer quantization of the two-terminal conductance, observed in this structures.

Graphene exhibits interesting spin- and valley-polarized QH ferromagnetic (FM) states. We show that spin-polarized QH state at zero doping hosts counter-circulating edge states carrying opposite spins, and propose to use this regime as a vehicle to study spin transport.

We study ordering in the valley-polarized QH state. Coupling of valley QHFM order parameter to random strain-induced vector potential yields an easy-plane-type ordering of the valley QHFM, giving rise to Berezinskii-Kosterlitz-Thouless transition, with fractionally charged vortices (merons) in the ordered state.

Thesis Supervisor: Leonid S. Levitov
Title: Professor of Physics

Acknowledgments

First and foremost I would like to thank my advisor, Leonid Levitov, who to a large extent determined the direction of the research presented in this thesis. His enthusiasm and remarkable breadth of knowledge make Leonid a great advisor and a real pleasure to work with. I find Leonid's way of thinking about physics to be insightful and elegant. With his ability to see phenomena at many different angles, an unlimited curiosity, a keen eye for an interesting problem and an impressive arsenal of mathematical skills, Leonid is a consummate theoretical physicist. I was very lucky to be his student, and he remains a role model for me.

Throughout my years at MIT, Leonid has brought various research topics to my attention, suggested an endless number of problems to work on, and helped me with solving some of them. I thank him for that. However, what I appreciate even more is that Leonid has been my mentor. Many hours of our discussions has largely shaped me as a scientist and made me understand, to a certain degree, how to do research on my own. He has been supportive, attentive, kind, and, maybe even more importantly, patient, which has made the learning process at MIT easy and enjoyable for me.

Another theorist who had a great influence on my development, as well as on this thesis, is Patrick Lee. Working with him was a privilege for me. Patrick has a remarkable physical intuition and an exceptional clarity of thinking; he is quick to find a clear and qualitative explanation for any physical phenomenon, no matter how complicated it may seem. I am very thankful to Patrick for sharing his skills; interacting with him helped me to see physics from a new perspective. Another Patrick's quality that I very much appreciate is his modesty. Despite being famous, he is always approachable, easy to talk to, and open to new ideas.

Experiment and theory in physics always go hand in hand. During my years at MIT I was lucky to interact with many outstanding experimentalists, who kindly shared their findings and made an effort to understand our theories. In fact, approximately half of what is presented below is the result of collaboration with experimentalists.

I owe a great deal of what I know about experiment to Charlie Marcus, as well as his former and current students, Dominik Zumbuhl, Leo DiCarlo, and especially Jimmy Williams. A meeting at MarcusLab would always be an opportunity to learn about exciting experimental results, get lots of questions and ideas, and drink excellent espresso. Working with Charlie and his students, and being exposed to their energy, optimism, great feel for physics, and hilarious sense of humous, has been a joy for me.

It was a tremendous privilege for me to collaborate with Andre Geim's group and Philip Kim's group. Andre's group discovered graphene; Andre's and Philip's groups discovered most of what we currently know about graphene properties. Andre and Philip gave me an opportunity to learn about experiments which will surely become classic; without them this thesis would be completely different. I am thankful to Andre and Philip, as well as their former postdocs, Kostya Novoselov, Barbaros Ozyilmaz, and especially Pablo Jarillo-Herrero.

I am thankful to the members of MIT Condensed Matter Theory Group for their genuine interest in physics, eagerness to discuss any topic any time, and creating a scientific environment that I consider to be nearly ideal. Conversations with Maxim Vavilov, Markus Kindermann, Saeed Saremi, Michael Slutsky, Nan Gu, Maissam Barkeshi, and Senthil Todadri were motivating and insightful for me.

I am especially grateful to my officemates – Pouyan Ghaemi, Roman Barankov and Mark Rudner – people with whom I spent a large fraction of every day. Pouyan, Roman and Mark are very different from each other, yet all of them are remarkable people and physicists; they are also dear friends to me. Pouyan is a very lighthearted person; talking to him is always easy and enjoyable. Roman's sincere passion for truth continues to inspire me and helps me to be honest with myself. Mark is truly one of the kindest people whom I know; his optimism and positive energy made an atmosphere in our office friendly and productive. Special thanks are due to Mark for helping me to improve my presentation skills, and correcting an endless number of articles in this Thesis.

During past 5 years, in addition to doing physics, I have spent many hours prac-

ticing dancing. Just a hobby at first, dancing gradually became an important part of my life, which taught me most of what I know about human body and emotions. My dance coach, Armin Kappacher, has been very much like a life mentor for me. Armin knows everything there is to know about the mechanics of human movement; he brings with him a tremendous energy, love of life, and utmost common sense. I thank him for sharing all of that; I am glad I could learn so much from him. I am also thankful to my dance friends, Olga Rostapshova, Andriy Didovyk, Esya Volchek, Ran Yi, Henry Newman, Rob Lakow, Jimmy Vanzo, Muyiwa Ogunika, Katya Kukuruza, Sarah Tishler, and many others; being around them was always fun, and helped me stay in a positive mindset.

I thank my closets friends, Vova Manucharyan, Adilet Imambekov and Zhao Chen for always being there for me; they are just like family to me. I know Zhao, Adilet and Vova very well, yet being around them is always exciting. I am grateful to Zhao for her kindness and understanding; thinking of Adilet and his jokes always makes me smile; Vova's encouragement and advice throughout some of the toughest periods of my life have been invaluable. Thank you, for all your support, for making me happy, and just for being the way you are.

I am grateful to my parents for their constant support, teaching me by example, confidence in me, and all their love. I also thank my sister Dasha, as well as the rest of my family. Every moment spent with them is a memorable experience which helps me see things from a broader perspective, teaches me something valuable, and just gives me a chance to feel at home.

Contents

List of Figures

List of Tables

Chapter 1

Introduction

Two-dimensional electronic systems (2DES) have been a major source of remarkable discoveries in quantum physics over the past 30 years [13]. In these systems, by varying the amount of disorder and the strength of electron-electron interactions, a nearly endless variety of new phases and physical effects can be realized [14]. A prominent example of a new quantum phenomenon arising in 2DES is the integer quantum Hall effect (QHE) [2]. The basic observation there is that the Hall conductivity of a 2DES subject to a strong magnetic field is quantized in units of e^2/h, while the longitudinal conductivity vanishes. Furthermore, experiments with 2DES in high magnetic fields revealed a *fractional* quantum Hall effect [15], where quantization of the Hall conductivity occurs at fractional values of e^2/h. Although transport properties in the fractional QHE and integer QHE are quite similar, the underlying physical mechanisms are completely different. While the integer QHE is essentially due to *single-particle* localization, the fractional QHE states are *strongly correlated* electron liquids, with the quantization of the Hall conductivity resulting from localization of collective electronic excitations [16].

In addition, the studies of 2DES in high magnetic fields have led to the discovery of phases with spontaneously broken symmetries [17], exotic excitations (so called anyons, which are neither bosons nor fermions but rather something in between [16, 18]) in correlated electron states, and stripe and bubble phases where an initially uniform electron liquid develops a periodic inhomogeneity [19] due to the spe-

cial form of effective electron-electron interactions [20, 21]. Also, 2DES can exhibit interesting phenomena in the absence of magnetic fields such as the collective behavior of excitons [22], which are bound electron-hole pairs. Reading this list (which is far from complete!), it is hard to believe that such a broad range of phenomena would be found in just one kind of electronic gas restricted to move in two dimensions.

These discoveries of spectacular many-body effects in 2DES are directly related to the progress in the fabrication techniques. Improving fabrication has enabled better control of disorder, producing samples clean enough for observing subtle interaction effects. For instance, the invention in 1960 of (relatively) clean Si-SiO_2 metal-oxide-semiconductor field-effect transistor (MOSFET) with tunable carrier density [23] led to the discovery of the integer QHE in 1980 [2]. In 1978 another breakthrough in semiconductor physics was made when a new crystal growth technique, molecular beam epitaxy (MBE), was used to create a high-mobility 2DES embedded in a three-dimensional GaAs-based structure [24]. Just a few years later, this 2DES, studied in ultrahigh magnetic fields by Tsui, Stormer and Gossard, revealed the fractional QHE [15]. Subsequent improvements of the MBE technique have led to discoveries of new fractional QHE states and other correlated electron phases [14].

In 2004, a fundamentally new type of 2DES was discovered [25] in graphene, a one-atom-thick sheet of carbon. The carrier density in graphene can be tuned over a range of positive and negative values using the field-effect [25]. Because graphene lattice is quite robust and therefore nearly free of structural defects, an advantage similar to that provided by carbon nanotubes, the 2DES in graphene has a high mobility. The mobility of carriers in graphene, although high enough for observation of certain correlated phases [5], is still several orders of magnitude lower than the mobility in the cleanest GaAs-based 2DES, which exhibit the broadest variety of correlated states. It has been conjectured that the mobility of graphene in current experiments is limited by the presence of a three-dimensional substrate which hosts charged impurities acting as scatterers for electrons in graphene [26]. Therefore, one possible route to increasing graphene mobility would be to fabricate suspended graphene samples, free of the three-dimensional substrate. A first step in this direction

has already been made [27], and conductivity measurements in suspended graphene revealed a tenfold mobility increase compared to samples on a substrate. Once the fabrication methods of suspended graphene are further improved to enable better control of intrinsic disorder, the mobility could be increased even further. The high electronic mobility, as well as the tunability of carrier density via the field-effect, make graphene an attractive platform for studying fundamental physics.

In addition to high mobility, the 2DES in graphene exhibits new electronic phenomena because of its unusual band structure, in which the low-energy excitations are described by the massless Dirac Hamiltonian rather than non-relativistic Schroedinger Hamiltonian, as in GaAs- or Si-based structures. There are two types of Dirac excitations in graphene, referred to as two valleys. The Dirac character of excitations modifies, and in some cases completely changes the nature of various physical properties and phenomena, from quantum tunneling [28] to localization by disorder [29]. Perhaps the most dramatic signature of the Dirac spectrum is the anomalous QHE, which is *half-integer* rather than integer [4, 30]. Remarkably, the characteristic energy scales of the electron states in graphene subject to magnetic field are quite large, with Landau level spacings reaching 1500 K at the magnetic field strength of 10 T. Because of that, the half-integer QHE can be observed at room temperatures [31]. Spin and valley-polarized QH states [17] resulting from interaction-induced splitting of otherwise degenerate Landau levels, which in some sense are prerequisite for fractional QH states, have already been observed in graphene [5]. Although the basic mechanism responsible for the formation of the spin- and valley-polarized QHE states in graphene is the same as that in the previously studied 2DES [17], some of those states in graphene exhibit transport properties which are quite different from the conventional QHE states [6]. Four years of studying graphene have already revealed a large number of interesting electronic phenomena [32], some of which are described in this thesis; however, this is surely just the very beginning, and graphene will yield many more interesting findings in the future.

In this thesis we consider several new phenomena which occur in graphene in the QHE regime. We shall develop a microscopic picture of the half-integer QHE in terms

of so-called QHE edge states, which are one-dimensional conducting channels at the boundary of QHE systems responsible for the QHE [33, 34]. While in conventional QHE systems the edge states are always chiral, all propagating in the same direction [33, 34], in graphene the edge states can have chirality of either sign, resulting from the fact that carriers can be electron-like or hole-like. As we shall see below, the counter-circulating character of the edge states gives rise to interesting transport phenomena in locally gated graphene devices, in particular, the fractional and integer two-terminal conductance quantization of these devices. Furthermore, we shall study QH states in graphene which result from interaction-induced lifting of spin and valley degeneracy. The spin-polarized QHE state at the Dirac point features counter-circulating edge states carrying opposite spins, which leads to unique behavior of the charge transport coefficients, as well as interesting spin transport effects, including a quantum spin Hall effect and spin filtering. Finally, we shall consider ordering of the valley graphene QH ferromagnet (QHFM), finding, somewhat surprisingly, that coupling of the order parameter to a peculiar type of disorder present in graphene stabilizes an easy-plane ordered state.

The rest of this introduction is organized as follows. In Section 1.1 we discuss the atomic structure of graphene, its place among other carbon materials, and describe the fabrication of graphene samples. Furthermore, we explain why graphene, being a two-dimensional crystal, is stable with respect to thermal fluctuations. In Section 1.2 we consider the electronic properties of graphene. We derive the Dirac-like low energy spectrum from the nearest-neighbor tight-binding model, and discuss the implications of the Dirac character of excitation for quantum tunneling and localization. We also point out that the truly two-dimensional character of the graphene lattice gives rise to new phenomena and opens up new possibilities to study electronic properties. Section 1.3 in an introduction to the conventional QHE. We discuss the edge states picture of the quantum Hall effect, and the physical mechanism of QH ferromagnetism. Section 1.4 is a review of the QHE in graphene, with an emphasis on differences from the conventional QHE systems. We discuss the half-integer QHE, experimental observations of the QHFM states, and their possible theoretical interpretation. Finally, Section

1.5 is an overview of the main results presented in the thesis.

1.1 Graphene: structural properties

The property of carbon which distinguishes it from all other elements is its unique chemical bonding flexibility. Carbon can bond with oxygen, hydrogen, nitrogen and other chemical elements, forming over ten million so-called organic compounds [35], many of which serve as a basis for all known life forms. There is also a large number of compounds consisting purely of carbon, which exhibit very diverse physical properties. Two well-known examples are three-dimensional carbon materials, diamond and graphite. The different arrangements of carbon atoms in these two materials gives rise to nearly opposite physical properties: diamond is very hard, and graphite is easy to break, diamond is transparent, and graphite is black, diamond is an insulator, while graphite is a conductor.

Carbon can also form low-dimensional compounds, so-called fullerenes, which have interesting physical properties resulting from both band structure and reduced dimensionality. Some common fullerenes are shown in Fig. 1-1. Zero-dimensional fullerenes [36], or buckyballs, have a discrete energy spectrum, very much like atoms or smaller molecules. One-dimensional fullerenes, called carbon nanotubes [37], host [38] a so-called Luttinger electronic liquid [39], which, owing to the enhanced role of electron-electron interactions in 1D exhibits unique transport properties very different from those of electronic liquids in two- and three-dimensional metals. In addition, similarly to the Dirac fermions in graphene, electrons in nanotubes have an internal degree of freedom, pseudospin, in many ways reminiscent of the fundamental electron's spin. This gives rise to interesting phenomena such as the $SU(4)$ symmetric Kondo effect [40]. Both nanotubes and buckyballs exhibit remarkable mechanical and chemical stability, which results from the strength of the carbon's chemical bonds.

The two-dimensional fullerene, called graphene, is a single-atom-thick sheet of carbon with atoms arranged in a honeycomb lattice, and can be viewed as the mother of the carbon materials. As illustrated in Fig. 1-1, graphite consists of weakly coupled

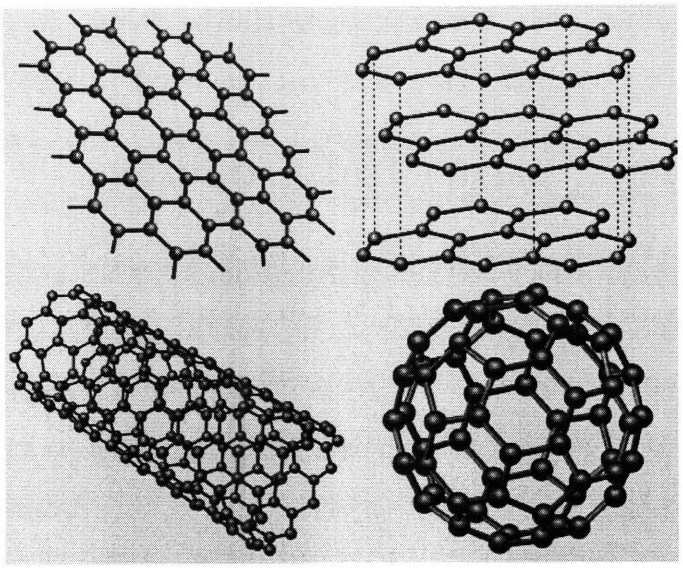

Figure 1-1: Graphene (upper left) as a mother of carbon allotropes. Graphite (upper right) is obtained by stacking graphene planes on top of each other. Carbon nanotubes (lower left) are rolled-up graphene sheets, and buckyballs (lower right) are obtained by substituting some hexagons in graphene lattice by pentagons, which gives rise to a curvature and results in graphene curling into a sphere. From Ref. [1].

layers of graphene, nanotubes are rolled-up sheets of graphene, and buckyballs are obtained by substituting some sixfold rings by fivefold ones, which results in curling the graphene sheet into a sphere or an ellipsoid. While buckyballs were discovered in 1985 [36], and carbon nanotubes in 1991 [37], graphene in a free form was only obtained in 2004 [25] by Andre Geim's group in Manchester. This discovery came as a big surprise, because the classical results of Landau and Peierls state that two-dimensional crystals cannot exist, as they are unstable with respect to thermal phonon fluctuations at arbitrarily low temperatures [41, 42]. Later in this section we shall discuss a physical mechanism of out-of plane fluctuations [43] that stabilizes the graphene sheet and resolves the seeming contradiction with the result of Landau and Peierls.

The fabrication method used to obtain graphene relies on the fact that adjacent atomic layers in graphite are very weakly coupled, and therefore thin stacks of graphene planes can be easily peeled from graphite. Interestingly, it is this property of graphite that allows us to use it as a writing tool. It was known and widely

utilized since 1564, when the graphite pencil was first introduced [44]. The method employed to make graphene essentially involves taking a piece of clean graphite and peeling it with an adhesive tape [25] (remarkably, usual Scotch tape was used in the original experiment) many times until a monolayer sample is obtained. Seemingly very simple, this experiment is in fact quite challenging: along with monolayers many thicker flakes are produced, and it is difficult to find extremely thin monolayers among multi-layers, which are the first ones to be noticed in the microscope. In fact, very special conditions are required to even be able to see monolayers in the microscope. The finding of graphene was made possible by an interference-like effect produced by graphene placed on top of a 300 nm thick SiO_2 substrate. The optical effect disappears, making graphene invisible, if the substrate width is changed by as little as five percent [32]! Therefore, the main challenge of fabrication is not making graphene, but finding it. There have been earlier attempts [45] to make thin stacks of graphene planes, which used techniques similar to the so called micro-mechanical cleavage introduced by the Manchester group. However, the thinnest samples found in those experiments consisted of at least 20 layers.

The optical effect is still used by most experimental groups to identify samples which may be monolayers, however, more reliable methods are needed to prove that a particular sample is indeed a monolayer. At present, there are two such methods: the first one is the Raman spectroscopy [46], and the second one is based on the half-integer quantum Hall effect [4, 30] (see below). The latter method, although not as reliable as the Raman spectroscopy, is widely used in transport experiments. In fact, it was the half-integer QHE that was used in the original works by the groups of Andre Geim [4] and Philip Kim [30] to unambiguously prove that the studied samples were indeed monolayers.

Before we proceed to discussing the electronic properties of graphene, we shall briefly address the stability of graphene membranes with respect to thermal fluctuations [32]. Graphene can crumple in the direction perpendicular to its plane, which, owing to the coupling of the out-of-plane fluctuations to the in-plane phonons, limits its in-plane displacement fluctuations. From the energetic point of view, crumpling

is favorable below a certain temperature, because, although it increases the elastic energy, it restricts the in-plane fluctuations, thus minimizing the free energy. This scenario, considered prior to the discovery of graphene in statistical mechanics of membranes [43], is supported by the direct experimental observation of ripples in graphene membranes [47]. As we shall discuss below, the crumpling generates an unusual type of disorder specific to graphene that leads to interesting phenomena; in particular, this type of disorder causes a suppression of the weak localization correction to conductivity [29], and ordering of the QHFM [48].

1.2 Electronic properties of graphene

Since 2004 graphene has attracted enormous interest, quickly becoming one of the most actively studied materials. The motivation for studying graphene lies in its fascinating physical properties, as well as the great promise it offers to applications: owing to graphene's two-dimensional character, graphene devices potentially can be made much smaller than traditional silicon counterparts. Some prototype devices, such as transistors made of graphene nanoribbons, have already been realized [49]. However, electronics applications require that a reliable growth process, capable of producing large samples of clean graphene, is developed. There have been attempts to grow graphene epitaxially by thermal decomposition of silicon carbide [50]. Samples grown by this method were found to exhibit rather high electron mobilities [50], however, further improvement of this fabrication process is needed.

Another intriguing direction is pointed out by proposals to employ graphene in solid-state-based quantum computing [51]. The main challenge in this field is to find systems where it is possible to realize the basic building blocks of quantum computer, qubits, with long coherence times. Most solid-state qubits considered so far had relatively short coherence times because of coupling to some external degrees of freedom. For example, the spin qubits [52], which can be controlled electrically [53], suffer from coupling to nulcear spins as well as the spin-orbit interaction, both of which cause decoherence [52]. Graphene spin qubits may help to solve this problem:

in principle, they can be made nearly free of decoherence, owing to the very weak spin-orbit coupling and the absence of hyperfine interaction in ^{12}C carbon atoms.

First and foremost, however, studying graphene is of interest from the fundamental physics standpoint, owing to its unique band structure, as well as its truly two-dimensional nature. The band structure of graphene is such that the low-energy excitations are two species of Weyl fermions [54] with opposite chiralities. Combined, the two Weyl spinors form a Dirac spinor, which is why we often refer to graphene excitations as Dirac fermions. As we discuss below, the Dirac-like band structure gives rise to a variety of new phenomena.

The origin of the Dirac spectrum of low-energy excitations can be understood using a nearest-neighbor tight-binding model on a hexagonal lattice, which is known to provide an adequate description of the graphene band structure. The honeycomb graphene lattice, illustrated in Fig.1-2a, has two non-equivalent sublattices, A and B. Fig 1-2a also illustrates the two most common graphene edge types, zigzag and armchair, which will be used in our analysis of quantum Hall edge states in Chapter 4. In the framework of the tight-binding model, which includes only nearest-neighbour hopping, the energy gap vanishes at the two non-equivalent Brillouin zone corners, K and K' (see Fig.1-2b). There are two linearly independent zero-energy Bloch functions for each of the points K, K'. One of these functions resides on sublattice A and vanishes on sublattice B, while the other resides on sublattice B and vanishes on sublattice A. Our choice of these Bloch functions for the K valley is shown in Fig.1-2c, where $\tau = e^{2\pi i/3}$. The Bloch functions for the K' valley can be obtained from those for the K valley by complex conjugation.

To describe low-lying excitations near the K, K' points, we write the wave functions as linear combinations of products of slowly varying enevelope functions $u_K, v_K, -u_{K'}, -v_{K'}$ and the four zero-energy Bloch functions [55], defined as in Fig.1-2c. (Our choice of the envelope function signs is convenient for our analysis of the edge spectrum for an armchair boundary, as we shall see below.) Here the u and v components are wave function amplitudes on A and B lattice sites. The envelope functions u_K, v_K, and $u_{K'}, v_{K'}$ describe excitations near the points K, K', and the effective low-energy

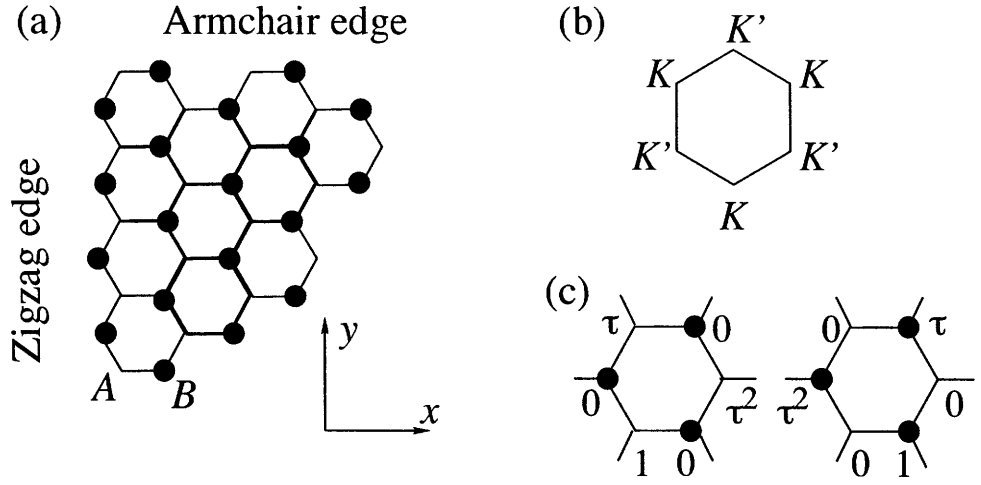

Figure 1-2: (a) Graphene lattice with armchair and zigzag edges. (b) Graphene hexagonal Brillouin zone. K and K' are the two non-equivalent Brillouin zone corners, where energy gap vanishes. (c) Our choice of two linearly independent zero-energy Bloch functions for the K point. Here $\tau = e^{2\pi i/3}$. The zero-energy Bloch functions for the K' point are obtained from those for the K point by complex conjugation.

Hamiltonian, obtained by keeping only lowest-order gradients of u, v, has the following form [55],

$$H_K = iv_0 \begin{bmatrix} 0 & \tilde{p}_+ \\ -\tilde{p}_- & 0 \end{bmatrix}, \quad H_{K'} = iv_0 \begin{bmatrix} 0 & \tilde{p}_- \\ -\tilde{p}_+ & 0 \end{bmatrix}, \tag{1.1}$$

where $v_0 \approx 10^8$ cm/s is the Fermi velocity, $\tilde{p}_\pm = \tilde{p}_x \pm i\tilde{p}_y$, $\tilde{p}_\mu = p_\mu - (e/c)A_\mu$, with A_μ being the vector potential.

Therefore, the effective low-energy excitations in graphene are two species of massless Weyl-like fermions, associated with the points K and K', which are usually referred to as valleys or pseudospins. The psedo-relativistic character of charge excitations in graphene leads to a wealth of new phenomena.

In particular, relativistic Dirac particles are capable of penetrating an arbitrarily high potential barrier at normal incidence [54]. This phenomenon, known as Klein tunneling [54], was theoretically predicted long ago in high energy physics [54]. Klein tunneling has never been observed for the Dirac electrons in vacuum, and remained a purely theoretical concept until about a month ago, when its observation in graphene was reported [56]. A potential step in graphene can be created using a local top gate [57, 9, 10] in addition to the global back gate. When the potential step is

steep enough such that transmission across the step is ballistic, the Klein tunneling manifests itself in the resistance across the barrier [56].

Furthermore, graphene provides an ideal setting to explore the behavior of disordered Dirac fermions, which can be quite different from that of massive electrons [26]. This problem has attracted significant interest previously due to its importance for understanding quantum Hall plateau transitions [58], as well as thermal transport in high-temperature superconductors [59]. By now it is realized, both theoretically [60, 61] and experimentally [29], that transport in graphene is strongly affected by the symmetry of disorder. In particular, disorder with certain symmetries does not localize Dirac electrons and the system remains metallic down to the lowest temperatures [60], in contrast to known systems with massive spectra. However, changing the symmetry of disorder may restore localization [26]. Other disorder types can give rise to anti-localization behavior [60], which, however, have not been observed yet. Despite recent advances [60, 29, 61] in studying disorder effects, the role of various disorder types present in the graphene samples is still a largely unexplored question.

The truly two-dimensional character of the graphene lattice also leads to interesting effects. For instance, recently there have been theoretical studies indicating the importance of electron scattering on flexural phonons [62], which cannot happen in GaAs-based and Si-based 2DES, where the two-dimensional gas is a part of a three-dimensional material. Another new feature is an atomically sharp edge of graphene, with different crystallographic edge orientations corresponding to different boundary conditions for the Dirac equation. Because of that, the electronic properties of graphene nanoribbons are strongly dependent on the sample's edge type [63]. The edge type also manifests itself in the dispersion of quantum Hall edge states [64], as we shall discuss in detail below in Chapter 4. Furthermore, random scattering of Dirac fermions on a disordered edge gives rise to a new symmetry class of a chaotic billiard in graphene quantum dots [65].

Interestingly, one of the common graphene edge types, the zigzag edge, supports a band of surface states [66]. There have been studies indicating that the surface states are rather robust with respect to some degree of edge disorder [67]. Owing to their

large density of states, the surface states may also exhibit a Stoner ferromagnetic instability [68]. Theoretically, the possibility of edge transport due to surface states has also been considered [69]. Experimentally, the relevance of these ideas remains to be explored.

The two-dimensional graphene lattice also supports an unusual disorder type, strain-induced random vector potential [12], which may have important implications for various phenomena including suppression of localization [29] and ordering of graphene quantum Hall ferromagnet [6], which we shall discuss in detail below. Essentially, strain shifts the positions of the Dirac nodes in momentum space due to (i) a purely geometrical effect, corresponding to the Brillouin zone deformation induced by the real space lattice deformation and (ii) a change of the local hopping amplitude due to bond stretching. Shifting the nodal points can be described in terms of an effective vector potential, which explains the origin of this disorder type. The random vector potential will be discussed in greater detail in Chapter 7, where we address the ordering of the QH ferromagnet.

One more interesting characteristic of graphene is that its surface is fully exposed. This opens up new possibilities for probing electronic properties, for example, using scanning tunneling microscope (STM) spectroscopy [70, 71, 72, 73]. In that regard graphene provides a distinct advantage compared to other two-dimensional systems where using the STM technique is made complicated by the fact that electrons are situated under a rather thick layer of dielectric. The STM technique was recently used to study the crumpling of graphene on a SiO_2 substrate [74]. Current STM techniques are capable of resolving individual graphene atoms, and therefore can be applied to image individual localized states in graphene [71], which may help elucidate the nature of impurities. Another interesting direction is using STM to explore the properties of the surface states near zigzag edges [73, 72].

In addition to the phenomena mentioned above, the Dirac spectrum and the two-dimensional graphene lattice have several interesting implications for the QHE in graphene. However, before we start discussing QHE in graphene, in the next section we give a brief introduction to the conventional QHE.

1.3 Introduction to the Quantum Hall Effect

This section is a brief introduction to the quantum Hall effect, providing the necessary background for the subsequent discussion of QHE-related phenomena in graphene. We start with the quantum Hall edge states picture, which helps to understand the quantization of the Hall resistivity. The chirality of the edge states is responsible for the absence of dissipation and the remarkable precision of the Hall conductivity quantization. Then we discuss QH systems where electrons have an intrinsic degree of freedom (spin, pseudospin) and a phenomenon of ferromagnetic ordering of this degree of freedom, which gives rise to new QH states. The discussion in this section applies to two-dimensional systems with a quadratic dispersion relation (Si, GaAs); systems with linear dispersion (graphene) will be the subject of the rest of the dissertation.

1.3.1 Edge states and the QHE.

In 1980 a German physicist Klaus von Klitzing studied [2] the Hall (ρ_{xy}) and longitudinal (ρ_{xx}) resistivity of two-dimensional Si MOSFET samples in strong magnetic fields and at low temperatures. He found that at low densities ρ_{xy} exhibits remarkable deviations from the classical formula $\rho_{xy} = B/en_c$ (n_c is the carrier density), featuring quantized plateaus at values

$$\rho_{xy}^{n} = \frac{h}{ne^2}, \tag{1.2}$$

with n an integer. The quantization (1.2) is commonly referred to as the quantum Hall effect; however, often 'QHE' is used as a general name for the phenomena arising in two-dimensional electronic systems subject to high magnetic fields at low temperatures. The quantization (1.2) is illustrated in Fig. 1-3, showing ρ_{xy} at a fixed magnetic field as a function of gate voltage, which translates into carrier density. The longitudinal resistivity ρ_{xx} vanishes at the plateaus, implying that the transport is

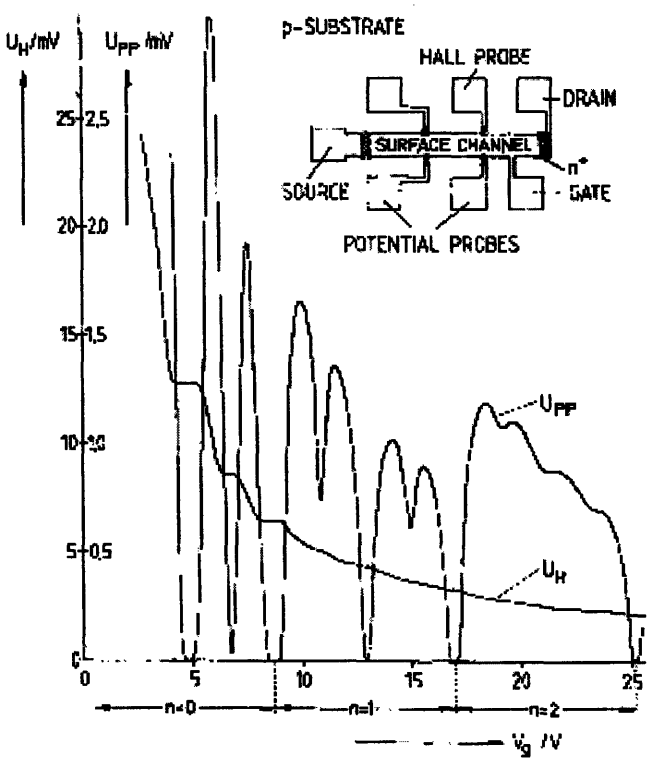

Figure 1-3: The Hall (ρ_{xy}) and longitudinal (ρ_{xx}) resistivity of a two-dimenional electron gas as a function of gate voltage, plotted in units of the voltage on Hall probes (U_H) and potential probes (U_{pp}). Resistivity ρ_{xy} exhibits a series of quantized plateaus with values $\rho_{xy}^n = h/ne^2$ – a remarkable phenomenon known as quantum Hall effect. Inset: schematic of the device. From the paper by von Klitzing [2]

non-dissipative; because ρ_{xx} vanishes, the Hall conductivity is also quantized,

$$\sigma_{xy} = n\frac{e^2}{h}. \tag{1.3}$$

To understand the quantum Hall effect, we examine the electronic spectrum of a sample having the shape of a strip situated in the region $0 < x < W$ in a magnetic

field. The spectrum can be found by solving the Shroedinger equation,

$$\varepsilon\psi = \frac{1}{2m}(\mathbf{p} - e\mathbf{A}/c)^2\psi, \tag{1.4}$$

where $\mathbf{A}$ is the vector potential. Choosing the coordinate system in such a way that the y-axis is parallel to the strip and fixing the gauge, $A_y = -Bx, A_x = 0$, allows us to classify states according to the values of momentum p_y. The motion in the x direction is described by the following equation,

$$\varepsilon\psi(x) = \frac{p_x^2}{2m} + \frac{m\omega_c^2}{2}(x - x_0)^2\psi(x), \quad x_0 = \frac{p_y\ell_B^2}{\hbar}, \quad \omega_c = \frac{eB}{mc}, \tag{1.5}$$

with ℓ_B is the magnetic length defined by Eq. (1.16). Eq. (1.5) describes an oscillator with a spectrum

$$\varepsilon_n = \hbar\omega_c(n + 1/2), \tag{1.6}$$

which corresponds to Landau levels (LLs).

To find how the spectrum is modified near the edge, we assume a hard-wall boundary condition, $\psi(x = 0, W) = 0$; we shall consider the spectrum near the edge $x = 0$, the spectrum near the opposite edge $x = W$ can be found similarly. The problem is to find the oscillator spectrum with a hard wall situated at the distance x_0 away from the parabolic potential minimum. The hard wall pushes the levels (1.6) up when δx becomes comparable to ℓ_B, their energies monotonically increasing as the edge is approached. This is illustrated in Fig. 1-4, depicting the numerically obtained oscillator energy levels depending on the momentum along the edge p_y, which is proportional to x_0 (see Eq. (1.5)). The dispersion of the LLs implies the existence of conducting one-dimensional channels propagating along the edge, with a group velocity of the channel originating from the nth LL being $v = \partial\varepsilon_n/\partial p_y$.

The edge states allow us to understand the quantum Hall effect as follows. When the filling factor ν is an integer, $\nu = n$, there are n conducting edge channels, as illustrated in Fig. 1-4. A current I flows along one of the edges, which corresponds to a Hall voltage $V_H = Ih/ne^2$. Thus the Hall resistivity is quantized, $\rho_{xy} = V_H/I =$

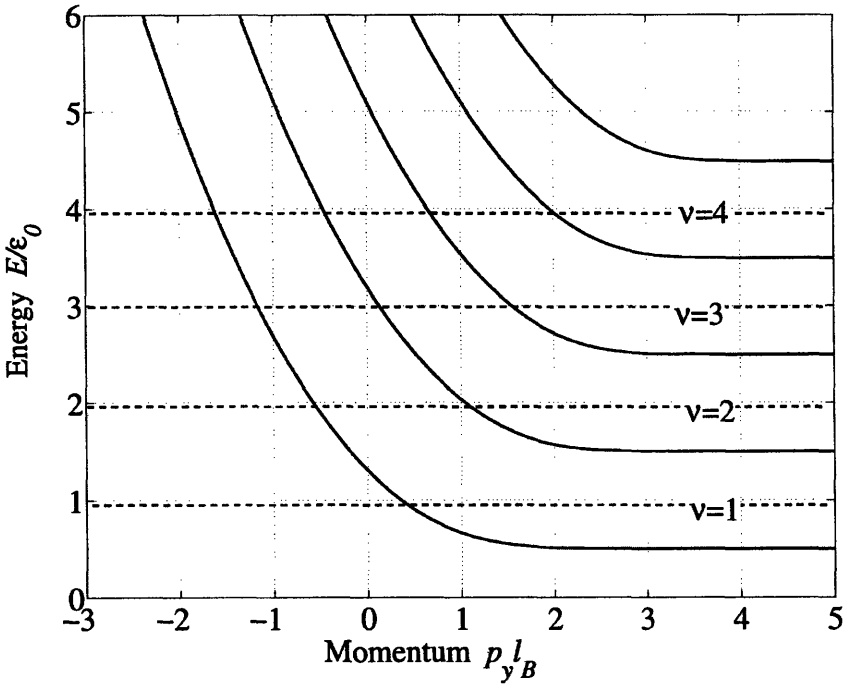

Figure 1-4: Spectrum of the Landau levels in a strip (in units of $\varepsilon_0 = \hbar\omega_c$), obtained by numerically solving the Schroedinger equation with a hard-wall boundary condition. Momentum p_y, equivalent to the magnetic oscillator position, is used to classify the energy levels. Landau levels, which are flat in the bulk, acquire dispersion near the edge. This corresponds to one-dimensional channels (one per LL) localized near the edge and propagating with velocity $v = d\varepsilon_n/dp_y$. At integer fillings, $\nu = n$, there are n conducting edge channels, which give rise to quantized Hall conductivity of ne^2/h.

h/ne^2.

The characteristic feature of these edge states is that they all propagate in the same direction. It is this property that is responsible for the non-dissipative nature of the QHE transport and the remarkable precision of the Hall conductivity quantization. Indeed, backscattering is necessary to generate a voltage drop along an edge and destroy the Hall conductivity quantization. However, because all edge channels at one sample edge propagate in the same direction, an electron has to tunnel to the opposite edge of the sample in order to backscatter. The transitions between opposite edges require passing through a wide classically forbidden region, and their probability is therefore suppressed by a factor of e^{-CW/ℓ_B}, where C is a constant of order one, which is determined by the chemical potential position relative to the LLs. Thus in wide samples, $W \gg \ell_B$, backscattering can be neglected and there is no dissipation on the quantum Hall plateau.

The dissipation on quantum Hall plateaus is absent when the transport is entirely due to the edge channels. However, when temperature is increased, thermally activated carriers in the bulk appear, introducing dissipation, which is described by a non-zero value of the longitudinal resistivity ρ_{xx}. Therefore one could say that the edge transport determines the value of the Hall resistivity, while the bulk transport is responsible for the longitudinal resistivity. As we shall see in the subsequent chapters, near the Dirac point in graphene the situation is exactly the opposite: the edge transport is dissipative and determines the value of ρ_{xx}, while introducing transport through the bulk changes the behavior of ρ_{xy}.

1.3.2 Quantum Hall ferromagnetism

In this subsection we discuss a specific kind of QH system, in which electrons have an internal degree of freedom. The nature of this degree of freedom may vary; in some cases it is the electron spin, in other cases it is valley index [75], and in double-well systems it is the well number [76]. The Coulomb interaction in such systems favors polarization of the intrinsic degree of freedom at certain filling factors, which gives rise to so called ferromagnetic QH states.

To simplify the discussion, we shall restrict our consideration to the lowest LL. For the purposes of this subsection, it is convenient to choose the radial gauge, $\mathbf{A}(\mathbf{r}) = -\frac{1}{2}[\mathbf{r}, \mathbf{B}]$. The wave functions in the lowest LL are given by

$$\varphi_m = \frac{1}{\sqrt{2\pi\ell_B^2 2^m m!}} z^m e^{-\frac{1}{4}|z|^2}, \tag{1.7}$$

where we have introduced a complex dimensionless coordinate $z = (x + iy)/\ell_B$. We shall use $\uparrow, \downarrow$ to denote the two intrinsic electron states, and refer to them as spins, keeping in mind that in fact our discussion is not limited to the case of the fundamental spin.

We will focus on the case when the spin-degenerate lowest LL is half-filled, that is, its filling factor (number of filled LLs) is $\nu = 1$. In general, the Coulomb interaction should favor polarizing all electron spins. This would make the spatial many-body wave function completely anti-symmetric, helping electrons to stay away from each other, and thereby minimizing the Coulomb energy. Motivated by this simple qualitative argument, we consider the following variational wave function, which describes filling all spin-up states,

$$|\psi\rangle = \exp\left(-\frac{1}{4}\sum_i |z_i|^2\right) \prod_{i,j} (z_i - z_j) \times |\uparrow\uparrow \ldots \uparrow\rangle. \tag{1.8}$$

The Coulomb energy of such a state is given by [17]

$$\frac{\langle\psi|V|\psi\rangle}{\langle\psi|\psi\rangle} = \frac{Nn}{2} \int d^2 z \frac{e^2 \ell_B}{\kappa|z|} \left[g(z) - 1\right], \tag{1.9}$$

where κ is the dielectric constant, $n = 1/2\pi\ell_B^2$ is the density of a filled LL, N is the total particle number, and $g(r)$ is the density-density correlation function,

$$g(z) = \frac{N(N-1)}{n^2\langle\psi|\psi\rangle} \int d^2 z_3 \ldots \int d^2 z_N |\psi(0, z, z_3, \ldots, z_N)|^2, \tag{1.10}$$

which can be computed exactly [17] for the wave function (1.8),

$$g(z) = 1 - e^{-\frac{1}{2}|z|^2}. \tag{1.11}$$

This expression has a transparent physical meaning: $g(z)$ vanishes when two particles approach each other, $|z| \to 0$, which corresponds to an exchange hole surrounding each electron. Substituting Eq. (1.11) into Eq. (1.9), we obtain the energy gain (per particle) due to the spin polarization,

$$\Delta = \frac{\langle V \rangle}{N} = -\sqrt{\frac{\pi}{8}} \frac{e^2}{\kappa \ell_B}. \tag{1.12}$$

Adding an electron with spin down requires an energy Δ, and therefore the system is gapped. Because of that, the transport in the bulk is suppressed, and the current is carried by the edge channels, leading to the quantum Hall effect. We emphasize that, although the transport properties of the ferromagnetic and integer QH states are similar, their nature is completely different: ferromagnetic QH states are due to the electron-electron interactions, while integer QH states would occur even in a non-interacting 2DES.

In the majority of studied systems [14] the Coulomb energy (1.12) is much larger that the spin-dependent energies, such as the Zeeman energy or spin-orbit interactions. For example, in GaAs the exchange energy (1.12) is two orders of magnitude larger than the Zeeman energy, which is especially small in GaAs due to the reduced value of the g-factor, $|g| \approx 0.4$. Thus to leading order the QH ferromagnet Hamiltonian is rotationally symmetric in the spin space.

What determines the orientation of the QH ferromagnetic order parameter? For any system, inevitably there are terms in the Hamiltonian (possibly small) that break the rotational symmetry in spin space, and thus fix the direction of the order parameter. Certain spin-dependent terms in the Hamiltonian act as symmetry-breaking fields, while the others induce an anisotropy, which can be of an easy-plane or an easy-axis type. For example, in the case of fundamental electron spin, the symmetry breaking field is provided by the Zeeman interaction. In the case of quantum Hall

bilayers [77, 14] the z component of pseudospin describes density imbalance between the two layers. The Coulomb energy is minimized when the two layers are equally charged, thus favoring the easy-plane-type state, corresponding to the $U(1)$ symmetric order parameter situated in the xy plane. The $U(1)$ symmetry of the order parameter gives rise to interesting phenomena, such as Berezinskii-Kosterlitz-Thouless transition and fractionally charged vortices [77, 76].

1.4 QHE in graphene

Owing to the unusual nature of the underlying material, the 2DES in graphene exhibits interesting phenomena in the QHE regime [4, 30, 5, 78], which are not encountered in the conventional QHE systems discussed above. The goal of this section is to review experimental and theoretical advances in understanding QHE properties arising due to the Dirac spectrum of excitations. We begin by discussing the half-integer QHE [4, 30], and provide a simple theoretical argument for the half-integer quantization based on the LL spectrum of Dirac fermions. Furthermore, we discuss experiments [5, 6, 79, 80] which observe interaction induced LL splitting in high magnetic fields, and theories [11, 81, 82, 83, 84, 48, 6] suggested to explain this splitting. Finally, we briefly address other reseach directions, such as experiments on transport in locally gated graphene devices [9, 10] and (theoretical) studies of correlated electron phases [85, 86, 87].

1.4.1 Half-integer QHE

In this Section we discuss the anomalous QHE in graphene. Figure 1-5 illustrates experimentally measured [4] transport coefficients, Hall conductivity σ_{xy} and longitudinal resistivity ρ_{xx} of graphene subject to a magnetic field of 14 T. The transport coefficients are shown as a function of the carrier density. The Hall conductivity exhibits a set of quantized plateaus situated symmetrically with respect to the Dirac

point, $\nu = 0$, with quantized values

$$\sigma_{xy}^{n} = 4 \times \left(n + \frac{1}{2}\right) \frac{e^2}{h}. \tag{1.13}$$

The factor of 4 in this expression is due to the twofold spin and valley degeneracies. Remarkably, the quantized values (1.13) are half-integer (up to the fourfold degeneracy) rather than integer (1.3), as in systems with Schroedinger spectrum of low energy excitations. The behavior of the longitudinal resistivity in graphene is quite similar to that observed in GaAs- and Si-based systems [88]: resistivity vanishes at the quantized plateaus of σ_{xy} and exhibits broadened peaks between the plateaus.

The half-integer QHE is a hallmark of the Dirac-like spectrum. For instance, bilayer of graphene [78], which has a band structure different from that of monolayer (electron-like and hole-like parabolic bands touching at zero energy), exhibits an integer QHE, as illustrated by the inset in Fig. 1-5. Thus the QHE signature provides a tool to distinguish QHE bilayers from monolayers [4, 78].

In experiments it is often more convenient to use two-terminal conductance measurements for sample characterization [89, 9], than to use the six-terminal measurements that allow one to find the full conductivity tensor [90]. Although the two-terminal conductance is quantized at the same values as σ_{xy}, in general it depends on both σ_{xx} and σ_{xy}, as well as on sample geometry; this often masks the quantization. In Chapter 2 we shall study the shape dependence of the conductance in the QHE regime, demonstrating that even when the quantization is completely washed out, local extrema of conductance still provide a way to distinguish monolayers from bilayers [7].

To understand the origin of the half-integer QHE, we study the LL spectrum in graphene. LLs in an external magnetic field B can be analyzed using the following gauge,

$$A_x = -By, \; A_y = 0. \tag{1.14}$$

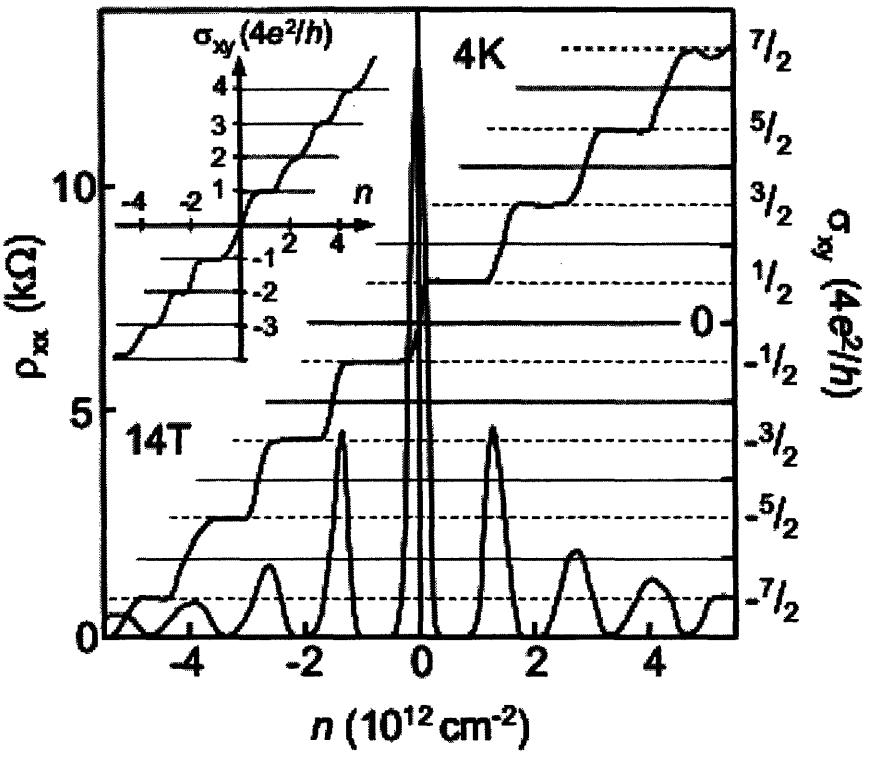

Figure 1-5: Quantum Hall effect in graphene at $B = 14\,\mathrm{T}$. Transport coefficients, Hall conductivity σ_{xy} (red) and longitudinal resistivity ρ_{xx} (green), are shown as a function of the carrier density. The Hall conductivity exhibits half-integer quantization in units of $4e^2/h$, resulting from the Dirac spectrum of excitations in graphene. Inset: σ_{xy} as a function of carrier density in bilayer graphene. The massive electron-hole symmetric band structure of bilayer graphene gives rise to the quantization of the Hall conductivity at integer values [3]. From Ref. [4]

Then the low-energy Hamiltonians (1.1) take the following form,

$$H_{K,K'} = i\frac{\varepsilon_0}{\sqrt{2}} \begin{bmatrix} 0 & \pm\partial_y + (y - y_0) \\ \pm\partial_y - (y - y_0) & 0 \end{bmatrix}, \quad \varepsilon_0 = \hbar v_0 \sqrt{2eB/\hbar c}, \tag{1.15}$$

where $y_0 = -p_x$. Here y is measured in the units of the magnetic length

$$\ell_B = (\hbar c/eB)^{1/2}, \tag{1.16}$$

and p_x is measured in the units of $\hbar/\ell_B$. The spectrum of the Hamiltonian (1.15) is given by the following equation [91],

$$E_n = \pm\varepsilon_0\sqrt{n}, \quad \varepsilon_0 = \hbar v_0 \sqrt{2eB/\hbar c} \tag{1.17}$$

with the sign plus (minus) for positive (negative) n, respectively. The structure of the LLs (1.17) allows one to understand the anomalous QHE. Since the levels (1.17) are spin- and valley-degenerate (we shall discuss the role of Zeeman splitting below), each of them gives rise to a step of $4e^2/h$ in the quantized Hall conductivity. The particle-hole symmetry $\varepsilon \to -\varepsilon$ of the spectrum (1.17), with the $n = 0$ level positioned exactly at the neutrality point, suggests that the QHE plateaus must occur at filling factors $\nu = \pm 2(2n + 1) = \pm 2, \pm 6, \pm 10, ...$, with conductivity given by Eq. (1.13), in agreement with the experiment [4, 30].

There are two other ways to understand the half-integer QHE in graphene. The most intuitive explanation is provided by the edge states picture [8, 11], which will be the subject of Chapter 4. The half-integer QHE can also be understood in a more fundamental way in terms of a quantum anomaly of the Dirac fermions [92, 91].

1.4.2 Spin- and valley-split QHE states

In this subsection we review experiments [5, 6] studying the splitting of LLs in graphene in high magnetic fields, as well as theories [11, 81, 82, 83, 84, 93, 48, 6] of the splitting mechanism.

Experimentally, it was found [5] that in magnetic fields above 15 T new quantized plateaus appear. This is illustrated in Fig. 1-6 which shows evolution of the Hall conductivity as the magnetic field is being increased from 9 T to 45 T. While at fields $B < 15\,\mathrm{T}$ the quantized values are given by the half-integer sequence, Eq. (1.13), at higher fields new quantized plateaus at $\sigma_{xy} = 0, \pm 1, \pm 4\, e^2/h$ develop. This signals lifting of the valley and spin degeneracy of the $n = 0$ LL, and the lifting of valley or spin degeneracy of $n = \pm 1$ LLs, schematically illustrated in the lower left inset in Fig. 1-6.

The behaviors of the longitudinal and Hall resistivities are displayed in the upper left inset of Fig. 1-6. The $\nu = 0$ state, despite exhibiting a clear plateau in σ_{xy}, has a non-vanishing longitudinal resistivity ρ_{xx}, while ρ_{xy} smoothly changes sign at the Dirac point, showing a fluctuating feature, but no distinct plateau. This is to be contrasted with the conventional QHE systems, where a plateau in the Hall conductivity is accompanied by vanishing of the longitudinal resistivity and a plateau in the Hall resistivity.

A more detailed study of transport coefficients near $\nu = 0$ was performed in Ref. [6]. The authors of Ref. [6] found, in particular, a metallic temperature dependence of ρ_{xx} at the Dirac point $\nu = 0$ (illustrated in the lower left inset of Fig. 1-7), and showed that $\rho_{xx}(0)$ was a monotonically increasing function of the magnetic field at $B > 10\,\mathrm{T}$. The behavior of the transport coefficients at low temperatures ($T = 4\,\mathrm{K}$) and high fields ($B = 30\,\mathrm{T}$) presented in Ref. [6], is shown in Fig. 1-7. Near $\nu = 0$ it qualitatively agrees with that found in Ref. [5], however, the plateaus at $\nu = \pm 1, \pm 4$, observed in [5], were absent in the experiment [6].

More recently, the longitudinal resistivity of the $\nu = 0$ state was investigated at even lower temperatures, $T \approx 0.3\,\mathrm{K}$ [80]. Interestingly, in this experiment it was found that above some critical magnetic field $B_* \approx 10\,\mathrm{T}$ the behavior of $\rho_{xx}(T)$ at the Dirac point changes from metallic to insulating.

The longitudinal resistivity at the $\nu = \pm 1, \pm 4$ plateaus vanishes, similarly to the conventional QHE states. It exhibits activated temperature dependence [79], from which gaps between split LLs can be extracted. The gaps at $\nu = \pm 1$ have a square

root magnetic field dependence [79], and by far exceed the bare Zeeman splitting, thus indicating the interacting nature of the split QH states. Furthermore, sensitivity of the gaps at $\nu = \pm 4$ to the in-plane magnetic field suggests that they are spin split rather than valley split.

Several scenarios which may be responsible for the observed LL splitting have been proposed [11, 81, 82, 83, 84, 93, 48]. Authors of Refs. [11, 81, 83, 84] considered ferromagnetic LL splitting, similar to that discussed in Section 1.4 above. An alternative mechanism of dynamically generated exciton-like gap was proposed in Refs. [93, 94, 95, 96]. Finally, a possibility of the Peierls-like spontaneous sublattice-symmetry breaking leading to LL splitting was considered in Ref. [82].

An important difference between the QHFM theories and dynamic mass generation as well as spontaneous Peierls-like sublattice instability is that QHFM predicts lifting of both valley and spin degeneracy for all LLs, while the two other theories predict that the valley degeneracy is only lifted for the $n = 0$ LL. So far only plateaus corresponding to valley degeneracy lifting of the $n = 0$ LL have been observed, which does not contradict any of the three theories. In QHFM theories the lifting of the valley degeneracy is suppressed by disorder [81], with higher LLs being more sensitive to the disorder amount [81]. Therefore it is highly desirable to explore whether samples with increased mobility (for example, suspended graphene samples [27]) would exhibit valley splitting of higher LLs. If found, such splitting would lend strong support to the QHFM scenario.

The theories of the interaction-induced LL splitting can be classified into two groups: those which predict a valley-polarized and spin-unpolarized $\nu = 0$ state [93, 82] and those where the $\nu = 0$ state is spin-polarized [11, 81, 83, 97]. The two states are predicted to exhibit very different transport properties: while the valley-polarized state is insulating, the spin-polarized state features counter-propagating edge states [11, 98], which give rise to a conducting behavior. The properties of the spin-polarized state will be considered in detail in Chapter 6 below. Experimental observations [5, 6], indicating the metallic character of the $\nu = 0$ state, favor the spin-polarized $\nu = 0$ state scenario.

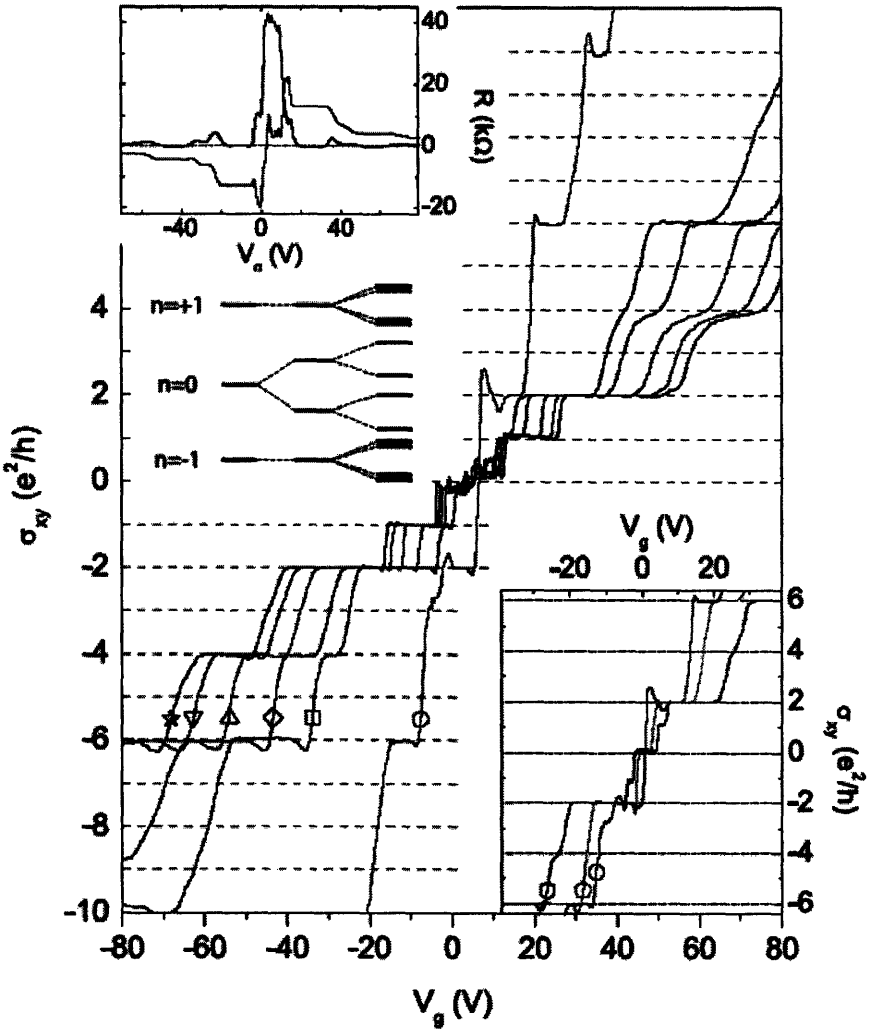

Figure 1-6: Evolution of the Hall conductivity σ_{xy} as a function of gate voltage V_g with increasing magnetic field: 9 T (circle), 25 T (square), 30 T (diamond), 37 T (up triangle), 42 T (down triangle), and 45 T (star). Right inset: detailed behavior of σ_{xy} near the Dirac point for $B = 9\,\mathrm{T}$ (circle), 11.5 T (pentagon) and 17.5 T(hexagon). Left upper inset: longitudinal and Hall resistivity measured at $B = 25\,\mathrm{T}$. Left lower inset: a schematic drawing of the LL splitting in high magnetic fields. From Ref. [5].

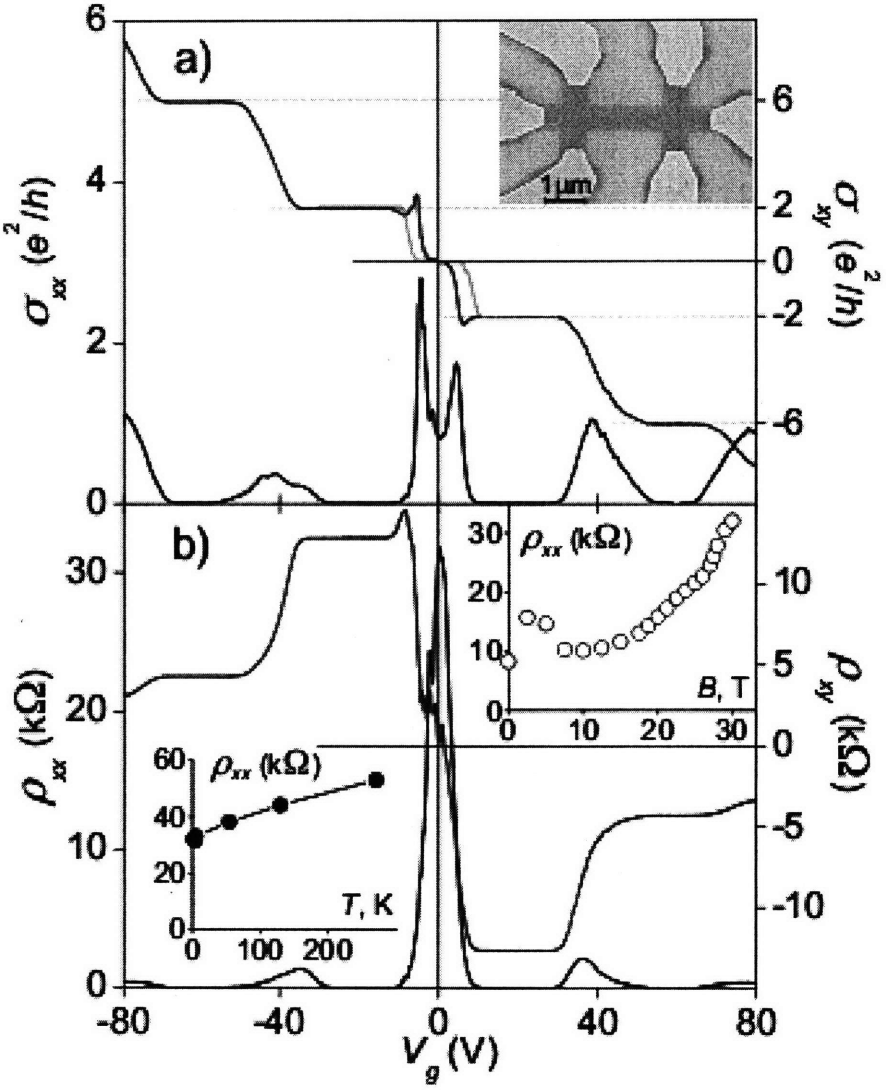

Figure 1-7: Longitudinal and Hall conductivities σ_{xx} and σ_{xy} (a) calculated from ρ_{xx} and ρ_{xy} measured at 4 K and $B = 30\,\mathrm{T}$ (b). The upper inset shows one of the measured devices. Temperature and magnetic field dependence of ρ_{xx} at $\nu = 0$ are shown in the insets below. Note the metallic temperature dependence of ρ_{xx}. From Ref. [6].

The authors of Ref. [80], on the other hand, claimed that the insulating temperature dependence of ρ_{xx} at the Dirac point observed in their experiment implies that the $\nu = 0$ is valley-, rather than spin-polarized. However, very recently it was argued [99] that such behavior could also result from the localization of the edge states in the spin-polarized $\nu = 0$ state. Thus at this point the character of the $\nu = 0$ state remains a subject of debate, and further studies are needed to elucidate its nature.

1.4.3 Other directions

In this subsection we briefly discuss two other directions in graphene QHE research, experiments on QHE in locally gated graphene devices [9, 10, 100], and theoretical studies of correlated electron phases in the QHE regime [85, 87, 86].

Interesting phenomena in the QHE regime occur in locally gated graphene devices, p-n and p-n-p junctions, where the carrier densities in the p and n parts of the device can be varied independently. In particular, owing to the electron-hole symmetry of the Dirac Hamiltonian, bipolar QH transport can be studied in these junctions. Experimentally, it was found [9, 10] that two-terminal conductance of p-n and p-n-p junctions in the bipolar regime exhibits a series of quantized plateaus, where, in addition to the half-integer quantized values (1.13), new fractional and integer quantized values appear. This quantization was explained [101, 10] in terms of the QH edge states mixing at the p-n interfaces. The detailed theoretical study of the QHE in the locally gated devices is presented below in Chapter 5.

Another interesting direction is the studies of the correlated electron phases in graphene. Owing to graphene's peculiar LL wave functions, the effective form of the electron-electron interaction in a LL is different [81, 84] from that in systems with quadratic dispersion relation. This leads to a new behavior of fractional QH states energies and gaps [87]. Furthermore, the approximate spin and valley symmetry of the Coulomb interaction in graphene may result in new $SU(4)$-symmetric fractional QH states [102, 86], not encountered in GaAs-based structures. Finally, a possibility of bubble and stripe phases [20] in higher LLs in graphene has also been considered in Ref. [85]. The fractional QHE, bubble and stripe phases in graphene have not been

observed experimentally yet, most likely due to disorder effects. However, there is a chance that correlated electron states will be found in recently demonstrated [27] suspended graphene samples, which have a much higher mobility than samples with substrate studied previously.

1.5 Main results of this thesis

This section is an overview of main results presented in the thesis, along with a discussion of their relation to the experimental and theoretical work described in the previous section.

1.5.1 Conformal invariance, shape-dependent conductance and graphene sample characterization

In Chapter 2, motivated by applications of two-terminal conductance measurements for sample characterization [89], we study general properties of two-terminal conductance depending on the sample's shape. We employ conformal invariance to show that the conduction problem in a sample of arbitrary shape can be reduced to that in an equivalent rectangle. Thus, the effect of sample geometry on the conductance is described by a single parameter, which is the aspect ratio of the equivalent rectangle.

We solve the conduction problem in a rectangular sample by a conformal mapping method [103]. This approach, supplemented by the semicircle law describing the behavior of the QHE conductivity tensor [104], allows us to analyze the conductance properties in the quantum Hall regime as a function of carrier density and LL broadening. We compare the conductance for monolayer and bilayer of graphene, identifying features which help to distinguish monolayers from bilayers. Interestingly, even for very asymmetric sample shapes with broadened LLs, where conductance quantization is completely washed out, the position and size of the conductance local extrema still allow us to determine the number of layers.

In Chapter 3, we apply our results for the conductance to graphene sample diag-

nostics. We first present experimentally measured conductance curves for samples of various shapes, including rectangular samples of various aspect ratios and a strongly asymmetric non-rectangular sample. The conductance maxima and minima positions and their sizes allow us to identify bilayer and monolayer samples, even in the cases where conductance quantization is poor or absent.

We fit the data for all studied samples, including the non-rectangular sample, with the help of our model for rectangular samples with a suitably chosen aspect ratio, finding a good qualitative agreement. For the non-rectangular sample, we explicitly construct a conformal mapping transforming the sample into a rectangle. The equivalent rectangle's aspect ratio agrees with that found phenomenologically from the fit to the conductance curve. This confirms that all shapes are classified by just one parameter. Interestingly, for several rectangular samples the aspect ratio found from the conductance differs from the actual sample's geometrical aspect ratio. We attribute this to the fact that only parts of the contacts may be active; another possible explanation is sample inhomogeneity.

1.5.2 Edge states and the half-integer QHE

In Chapter 4, we develop the microscopic edge states picture of the half-integer QHE in graphene. For that, we study the edge states spectrum for armchair and zigzag edge orientations, solving the Dirac equation with proper boundary conditions for each. For the zigzag edge, we analyze an interesting interplay between the zeroth LL and the band of zero-energy surface states [66]. We find that, although the edge orientation affects the details of the spectrum, the number of conducting edge channels is odd independent of the edge type, which implies the universality of the half-integer QHE.

Furthermore, we propose that the properties of the edge states can be probed by STM spectroscopy. In particular, owing to the momentum-space duality, the real space map of the local density of states near the edge can be used to analyze the dispersion of the edge states.

1.5.3 QHE in locally gated graphene devices

In Chapter 5, we explore transport in locally gated graphene devices, p-n and p-n-p junctions in the QHE regime. The edge states in graphene at positive and negative energies are of electron and hole types and because of that they propagate in opposite directions. We argue that this enables the realization of interesting edge states transport regimes in bipolar p-n and p-n-p junctions, where both electrons and holes are present in different parts of the device. When QHE states are formed in the p and n parts, the edge states in p and n regions propagate in the opposite directions, bringing electrons from both regions to the p-n interface, where they can scatter and interact, as in chaotic quantum dots [105]. We show that full electron mixing at the p-n interfaces gives rise to the experimentally observed quantization of the two-terminal conducatnce at fractional and integer values [9, 10] mentioned in Section 1.4. We point out that mixing can be due to several mechanisms, including coupling of the edge states to the bulk localized states, self-averaging, and electron thermalization. All three mechanisms give rise to quantized shot noise Fano factors. However, the quantized Fano factor values are different in the three cases, and therefore shot noise can be used as a tool to study transport mechanisms at the p-n interfaces.

The agreement between our theory and experiment [10] is not complete: while most quantized conductance plateaus predicted by our model for p-n-p junctions are indeed observed experimentally [10], others are either absent or their values deviate significantly from the theoretical ones. In an attempt to explain this observation, we study the sensitivity of the conductance quantization to the edge states backscattering in the locally gated n region. In the experiment, the backscattering could result from the density inhomogeneities induced by the local gate. We employ a bulk conductivity approach, modeling the p-n-p junction by a conductor with a spatially non-uniform conductivity tensor, where the edge state backscattering is taken into account by introducing a non-zero longitudinal conductivity component. Solving this model exactly by a conformal mapping method [103], we find that the sensitivity of quantization to backscattering strongly depends on the central region's geometry. We

determine which plateaus are most stable depending on the central region's aspect ratio. Our findings allow us to understand the discrepancy between the experiment [10] and the simple edge states theory without backscattering.

1.5.4 Spin and charge transport at the graphene edge

In Chapter 6 we analyze spin and charge transport phenomena which occur in the spin-polarized ferromagnetic QHE state at the Dirac point. Based on the results obtained in Chapter 4, we argue that the spin-polarized QH state at the Dirac point exhibits unusual counter-propagating edge states, which carry opposite spins. We show that these spin-filtered edge states give rise to a quantized spin Hall effect [11], and propose that they can be used to explore interesting spin transport phenomena, including spin filtering and the detection of spin polarized currents.

Despite the counter-circulating character of the edge states at the Dirac point, their backscattering is strongly suppressed, because in order to backscatter electrons at the edge have to flip their spin. We estimate the mean free path at the edge, considering scattering due to spin-orbit and potential disorder, and find the mean free path to be comparable to the typical samples size. Based on this result, we argue that the spin-filtered edge states dominate the charge transport properties of the spin-polarized $\nu = 0$ state, in particular, giving rise to the metallic behavior of conductivity.

We formulate and solve a model [6, 64], where edge state transport near $\nu = 0$ is accompanied by shunting of the opposite edges by a weakly conducting bulk. This allows us to obtain density dependence of transport coefficients, which is strikingly similar to that observed experimentally (a plateau in σ_{xy}, a broadened peak in ρ_{xx} and ρ_{xy} smoothly changing sign; see discussion in Section 1.4). Agreement of our model with the experiment lends strong support to the theory of a spin-polarized ferromagnetic state at the Dirac point.

1.5.5 Disorder-induced anisotropy in valley QH ferromagnet

Finally, in Chapter 7 we study ordering of the valley degree of freedom in the graphene QH ferromagnet. In the leading order the Coulomb energy is isotropic with respect to rotations in the valley space, which gives rise to rotationally symmetric QHE ferromagnetic states. To understand the ordering of the valley QHFM, we first study anisotropic terms in the Hamiltonian resulting from the lattice effects. They, however, turn out to be negligible [48]. Thus we look for other possible sources of anisotropy in the valley space, finding that coupling to random strain-induced vector potential (see Section 1.2 above) may introduce a rather large easy-plane anisotropy [48]. The XY-ordered valley ferromagnetic state features a Berezinskii-Kosterlitz-Thouless (BKT) phase tranistion at low, but experimentally accessible temperatures, as well as fractionally charged quantum vortices [76] (merons) below the BKT transition temperature.

Chapter 2

Conformal Invariance and Shape-Dependent Conductance of Graphene Samples

2.1 Abstract

For a sample of an arbitrary shape, the dependence of its conductance on the longitudinal and Hall conductivity is identical to that of a rectangle. We use analytic results for a conducting rectangle, combined with the semicircle model for transport coefficients, to study properties of the monolayer and bilayer graphene. A conductance plateau centered at the neutrality point, predicted for square geometry, is in agreement with recent experiments. For rectangular geometry, the conductance exhibits maxima at the densities of compressible quantum Hall states for wide samples, and minima for narrow samples. The positions and relative sizes of these features are different in the monolayer and bilayer cases, indicating that the conductance can be used as a tool for sample diagnostic. The results presented in this Chapter are published in Ref. [7].

2.2 Introduction

One of the challenges in graphene experiments is finding reliable methods for sample characterization, allowing to distinguish graphene monolayer from graphene bilayer or multilayer systems. Quite often, the means for that are provided by Raman spectroscopy [46]. However, in a number of experiments it is more convenient to perform sample characterization using transport measurements [90].

The simplest transport characteristic of a graphene device is its two-terminal conductance. This quantity exhibits plateau-like structure in the QHE regime, occurring at different electron densities in the monolayer and bilayer systems, which in principle makes it suitable for sample diagnostic. However, the observed conductance plateaus are often distorted, which is not surprising, because the two-terminal conductance, unlike the resistivity obtained from a four-probe measurement, in general depends on the sample aspect ratio and other geometric characteristics. This dependence must be taken into account, in as much as possible, in interpreting the measurement results.

The effect of sample shape on the conductance can be illustrated by the well known formula for a conducting square with the longitudinal and Hall conductivities σ_{xx} and σ_{xy} and ideal contacts on opposite sides [106, 107]:

$$G_{L=W} = \sqrt{\sigma_{xx}^2 + \sigma_{xy}^2}, \tag{2.1}$$

which follows from a duality relation for 2d transport (see [107, 108] and discussion below). The result (2.1) gives the macroscopic conductance in terms of microscopic transport coefficients. As we shall see, the dependence on σ_{xx} and σ_{xy} in Eq.(2.1) is such that it can make the conductance $G_{L=W}$ density-independent in the QHE regime near the graphene charge neutrality point (CNP), where both σ_{xx} and σ_{xy} have strong density dependence. Thus the effect of sample geometry on conductance may be nonintuitive and should be accounted for carefully.

Is it possible to extend the result (2.1), valid for a perfect square, to other sample geometries? The next simplest shape to a square is a rectangle, for which the two-terminal conductance was found in Ref.[106] using conformal mappings of the

Schwartz-Christoffel form. For all other shapes, luckily, the conduction problem can be reduced, via a conformal mapping, to that of a rectangle (see below). The aspect ratio of such an equivalent rectangle, which depends on the size of the contacts and on their separation, can serve as a parameter that classifies all conduction problems.

In Ref.[106] a closed-form expression for the conductance of a rectangle was obtained via an integral representation. However, as discussed below, the integrals of Ref.[106] are convergent very slowly, especially in the interesting limit of large Hall angles. Because of that, for our purpose it will be more convenient to employ the approach of Rendell and Girvin [103], which describes spatial distribution of the electric field and current in terms of a suitably chosen analytic function, allowing for direct numerical evaluation of the conductance.

Below we use the method of Ref. [103] combined with the effective medium approach of Dykhne and Ruzin [104] that yields a semicircle relation between σ_{xx} and σ_{xy}. We analyze conductance as a function of carrier density, focusing on the features that distinguish between transport in the monolayer and bilayer graphene. We conclude that the dependence of conductance on the sample shape, which may be quite strong, does not mask the difference between the monolayer and bilayer systems even in the absence of clear conductance plateaus.

For the effective medium approach [104] to be applicable, the sample size must be large compared to the typical charge inhomogeneity length scale ξ, otherwise strong mesoscopic sample-to-sample fluctuations are to be expected. In most of the paper we focus on the case of large samples, which can be described by a spatially uniform conductivity tensor obeying the semicircle relation. We shall briefly discuss the situation in mesoscopic samples of size comparable to ξ at the end of the paper.

2.3 Duality relation for conductance

Here we shall focus on the rectangular geometry illustrated in Fig.2-1 inset (later, in Section , it will be shown that for any conductor shape the problem can be mapped on that of an equivalent rectangle). To describe electric transport, we employ the bulk

conduction approach, in which the sample bulk is characterized by the longitudinal and Hall conductivities σ_{xx}, σ_{xy}. The transport equation is $\mathbf{j} = \hat{\sigma}\mathbf{E}$ where $\hat{\sigma}$ is a 2×2 conductivity tensor, with the current and electric field obeying

$$\nabla \cdot \mathbf{j} = 0, \quad \nabla \times \mathbf{E} = 0 \tag{2.2}$$

These equations must be solved with the boundary conditions $\mathbf{j}_\perp = 0$ at $x = 0, W$ (current continuity) and $\mathbf{E}_\parallel = 0$ at $y = \pm L/2$ (ideal ohmic contacts).

It is instructive to apply duality transformation [108, 107] to this problem, rotating current $\mathbf{j}$ and electric field $\mathbf{E}$ by 90^o and interchanging them: $\mathbf{j}' = R_{\pi/2}\mathbf{E}$, $\mathbf{E}' = R_{\pi/2}\mathbf{j}$. Upon such a transformation the transport equations (2.2), as well as the boundary conditions, preserve their form, whereby the conductivity tensor is replaced by $\hat{\sigma}' = \hat{\sigma}^{-1}$ and the dimensions of the rotated rectangle interchange: $L' = W$, $W' = L$. Since resistance for the transformed problem $R = V'/I' = 1/G'$ is identical to the conductance of the initial problem $G = I/V$, where V is source/drain voltage and I is net current, we obtain a duality relation

$$G(L, W, \hat{\sigma}) = G^{-1}(L', W', \hat{\sigma}') \tag{2.3}$$

We note that, since $\hat{\sigma}' = \hat{\sigma}^{-1}$ is the resistivity tensor, the quantity $G(L', W', \hat{\sigma}')$ has dimension of resistivity, and so the right hand side of (2.3) has dimension of conductance. To simplify the relation (2.3), we take into account that G scales with $\hat{\sigma}$, i.e. that $G(L, W, \eta\hat{\sigma}) = \eta G(L, W, \hat{\sigma})$, and that it is invariant upon sign reversal of σ_{xy}. Writing $\sigma'_{xx} = \sigma_{xx}/(\sigma_{xx}^2 + \sigma_{xy}^2)$, $\sigma'_{xy} = \sigma_{xy}/(\sigma_{xx}^2 + \sigma_{xy}^2)$, and using the scaling property of G, we obtain a relation

$$G(L, W, \hat{\sigma}) = (\sigma_{xx}^2 + \sigma_{xy}^2)/G(W, L, \hat{\sigma}), \tag{2.4}$$

which connects the rectangles $L \times W$ and $W \times L$ having *the same* bulk transport coefficients. Setting $L = W$, we obtain the conductance of a square, Eq.(2.1).

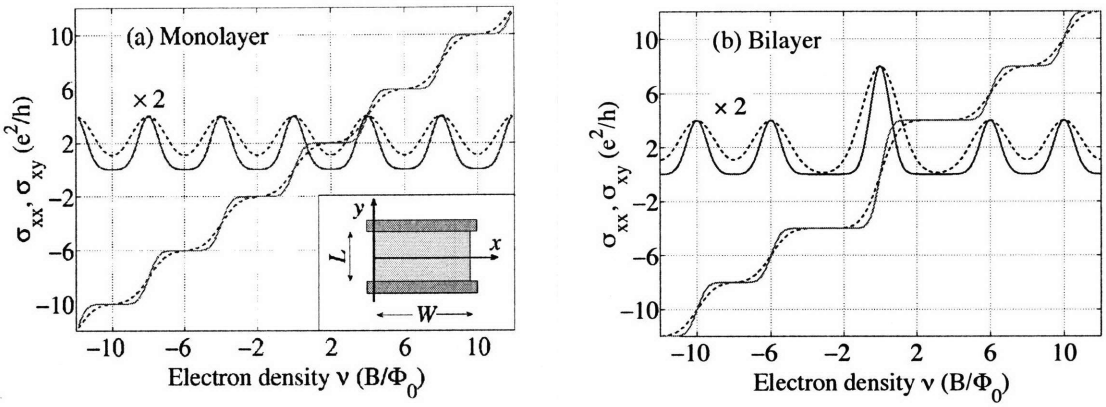

Figure 2-1: Longitudinal and Hall conductivity for (a) graphene monolayer and (b) graphene bilayer, obtained from the semicircle model, Eqs.(2.9),(2.7),(2.8), for two values of the Landau level width parameter $\lambda = 1.7$ (solid lines), $\lambda = 0.5$ (dashed lines). *Inset:* Schematic of a conducting sample of dimensions L and W, of a rectangular shape, with source and drain at opposite sides.

2.4 The semicircle model

The effective medium approach [104] provides a convenient framework for understanding the density dependence of σ_{xx} and σ_{xy} in QHE systems. It predicts a semicircle relation between σ_{xx} and σ_{xy}, derived from a two-phase model, in which the system at the QHE transition is treated as a mixture of incompressible puddles with local Hall conductivities σ'_{xy}, σ''_{xy}, given by the quantized values at the neighboring QHE plateaus.

The semicircle relation is a statement about properties of the macroscopic conductivity tensor on the length scales much greater than the size of individual puddles. Although the validity of this relation, strictly speaking, is limited to the regime dominated by large-scale fluctuations of electron density, it is empirically known to provide a good description of the integer QHE plateau transitions observed in various semiconducting systems [109]. Recently, the semicircle relation was employed to describe transport coefficients in graphene [6, 64, 110].

We stress that, while the semicircle model is realistic, and also quite convenient to use, its specifics are almost certainly not essential for our conclusions. We believe that slight departure in behavior of transport coefficients from the semicircle model

will have little effect on the properties of conductance.

Prior to turning to the semicircle model, we recall that the conductivity σ_{xy} in graphene monolayer exhibits steps of size $4e^2/h$ between adjacent integer quantum Hall plateaus, where the factor of four describes combined spin and valley degeneracy of Landau levels. The incompressible densities corresponding to the QHE plateaus in graphene monolayer are [4, 30]

$$\nu_n = 4(n+1/2)|B|/\Phi_0, \quad n = 0, \pm 1, \pm 2..., \tag{2.5}$$

where $|B|/\Phi_0$ is electron density for a single Landau level. In graphene bilayer QHE, due to accidental degeneracy of the Landau level positioned at the neutrality point $\nu = 0$, there is an $8e^2/h$ Hall conductance step between the plateaus with $\sigma_{xy} = \pm 4e^2/h$, whereas other conductance steps are of normal $4e^2/h$ size. Accordingly, in the bilayer the incompressible QHE densities are [78]

$$\nu_n = 4n|B|/\Phi_0, \quad n = \pm 1, \pm 2... \tag{2.6}$$

In both cases (2.5) and (2.6) the density values ν_n are arranged symmetrically around the neutrality point. Hall conductivity on the plateaus takes the values $\sigma^{(0)}_{xy,n} = \nu_n e^2/h$, where ν_n are densities (2.5) and (2.6).

In the semicircle model [104], the contributions of each Landau level to the longitudinal and Hall conductivities $\delta_n\sigma_{xx}(\nu)$, $\delta_n\sigma_{xy}(\nu)$ are related by the semicircle law:

$$\delta_n\sigma_{xx}^2 + (\delta_n\sigma_{xy} - \sigma^{(0)}_{xy,n})(\delta_n\sigma_{xy} - \sigma^{(0)}_{xy,n'}) = 0, \tag{2.7}$$

where $\sigma^{(0)}_{xy,n}$ and $\sigma^{(0)}_{xy,n'}$ are the quantized Hall conductivities on adjacent plateaus. Here n and n' are neighboring integers in the sequence $...-2,-1,0,1,2...$ for the monolayer, and $...-2,-1,1,2...$ for the bilayer: $n' = n+1$ except the double-degenerate $\nu = 0$ Landau level for the bilayer, in which case $n = -1$, $n' = 1$.

The longitudinal conductivity $\delta_n\sigma_{xx}(\nu)$ exhibits a peak centered at the Landau

level. We model it by a gaussian

$$\delta_n\sigma_{xx}(\nu) = \frac{1}{2}C_n e^{-\lambda\left(\nu-\frac{1}{2}(\nu_n+\nu_{n'})\right)^2} \tag{2.8}$$

where the parameter λ describes broadening of the Landau level (large values of λ correspond to a narrow Landau level).

In the semicircular model, the peak value of $\delta_n\sigma_{xx}$ must equal to $\frac{1}{2}(\sigma^{(0)}_{xy,n'} - \sigma^{(0)}_{xy,n})$. This is ensured by the prefactor C_n value in Eq.(2.8) chosen to coincide with the nth Landau level degeneracy. For graphene monolayer we set $C_n = 4$ (spin and valley degeneracy) for all n, while for the bilayer $C_n = 8$ for $n = -1$ (spin, valley and accidental degeneracy) and $C_n = 4$ for all other n's.

The total conductivity tensor is given by the sum of the contributions of all Landau levels,

$$\sigma_{xx}(\nu) = \sum_n \delta_n\sigma_{xx}(\nu), \quad \sigma_{xy}(\nu) = \sum_n \delta_n\sigma_{xy}(\nu). \tag{2.9}$$

For simplicity, here we choose the same value of the parameter λ for all Landau levels. The resulting conductivity density dependence is illustrated in Fig.2-1a,b.

We point out that an interesting prediction can be drawn, specific to the graphene zeroth Landau level ($\nu = 0$), by combining the semicircle model (2.7) with Eq.(2.1). In a square sample with a negligible overlap between Landau levels, the two-terminal conductance (2.1) would be completely density-independent across the zeroth Landau level, because in this case $\sqrt{\sigma_{xx}^2 + \sigma_{xy}^2}$ would equal $2\frac{e^2}{h}$ for the monolayer and $4\frac{e^2}{h}$ for the bilayer. This happens because the density dependence of transport coefficients, the peak in σ_{xx} and the step in σ_{xy}, centered at $\nu = 0$, cancel each other in the expression (2.1). For weakly overlapping Landau levels, the contributions of the levels adjacent to $\nu = 0$ would lead to slight deviations from a flat plateau.

The conductance measured in graphene indeed often exhibits a plateau across the entire $\nu = 0$ region. Two examples of such behavior in recent literature are Ref.[89], Fig. 1d, and Ref.[9], Fig. 3B. In both cases, the measured conductance is nearly flat in a wide density interval centered at $\nu = 0$, with a small peak in the middle. Interestingly, the sample geometry in both cases was quite different from a square. In Ref.[89] the

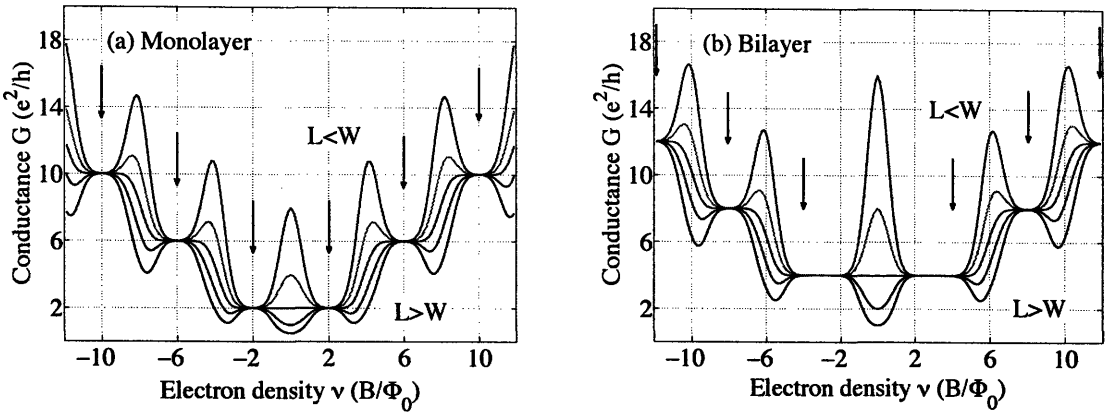

Figure 2-2: Two-terminal conductance (2.15) of a rectangular graphene sample: (a) monolayer, (b) bilayer, for aspect ratios $L/W = 0.25, 0.5, 1, 2, 4$ (top to bottom) with the Landau level width parameter $\lambda = 1.7$ (corresponding to solid lines in Fig.2-1). Arrows mark the incompressible densities (2.5), (2.6). Note the plateau at $\nu = 0$ for the square case, $L = W$ (red curve), which is in agreement with the behavior predicted by Eq.(2.1).

AFM image indicated that the sample was approximately rectangular with contacts at opposite sides, similar to the schematic in Fig.2-1 inset. However, its width was quite large, $W \approx 5L$, in which case a fairly large peak at $\nu = 0$ is to be expected (see below). To understand the discrepancy, it would be useful to known how spatially uniform the conduction was, in particular near contacts (poor contact along part of the sample edge could reduce the effective sample width, bringing W closer to L). As for the device in Ref.[9], its contact geometry was quite far from rectangular, yet giving rise to a fairly good plateau around $\nu = 0$.

Such a behavior can be understood in the context of universality of the conductance problem that results from its conformal invariance. As we discuss in Appendix, for an arbitrary geometry of a conductor with two contacts of arbitrary sizes the conductance is identical to that of an equivalent rectangle. In other words, all possible conduction problems are classified by the values of a single parameter, the aspect ratio L/W of an equivalent rectangle. Then, as long as $L/W \approx 1$, the conductance would behave in the same way as for a square shape, even if the actual geometry is very different from a square.

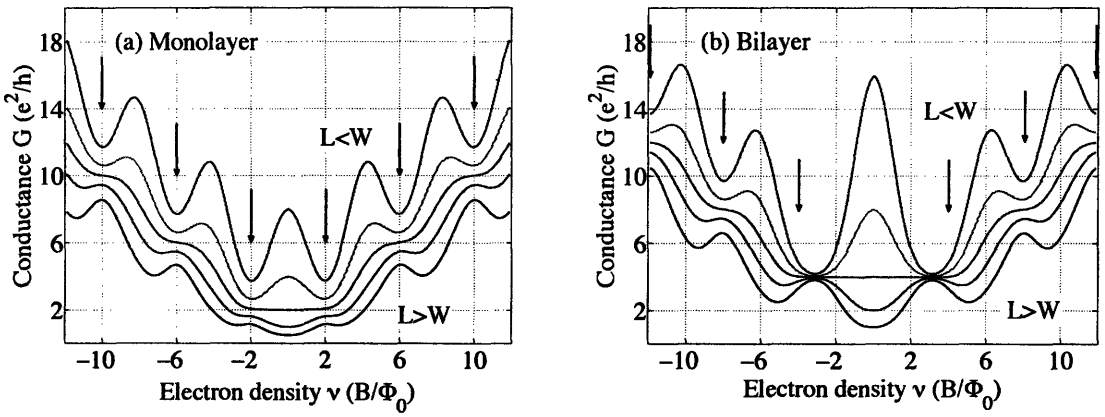

Figure 2-3: Same as in Fig.2-2 for broader Landau levels, described by (2.8) with $\lambda = 0.5$ (dashed lines in Fig.2-1); the sample aspect ratios are $L/W = 0.25, 0.5, 1, 2, 4$ (top to bottom). Note that the qualitative features, such as the positions of the conductance minima at the QHE plateau centers for $L < W$ (maxima for $L > W$), as well as the conductance values at these densities, are similar to those seen in Fig.2-2 despite increased Landau level broadening. Note also the relative size of the $\nu = 0$ peak in the monolayer and bilayer cases, compared to the size of neighboring peaks at other compressible densities, which is also insensitive to the Landau level broadening.

2.5 Conformal mapping approach

Now we proceed to describe the distribution of current and electric field in a rectangular sample with an arbitrary aspect ratio L/W and spatially uniform conductivities σ_{xx}, σ_{xy} (see Fig.2-1 inset). This problem, with zero boundary condition for normal current component at the sample boundary and for tangential field component at the sample/contact interface, has been treated in Refs. [106, 103] using conformal mapping technique.

In Ref. [106] the Schwartz-Christoffel mapping was employed, leading to the following integral representation for the conductance:

$$G = \sqrt{\sigma_{xx}^2 + \sigma_{xy}^2}\, \frac{I(1,-1)}{I(1/k,1)}, \tag{2.10}$$

where

$$I(u,v) = \int_v^u \frac{d\xi}{|(\xi-1)(1/k+\xi)|^{\delta_+}|(\xi+1)(1/k-\xi)|^{\delta_-}}. \tag{2.11}$$

Here $\delta_\pm = 1/2 \pm \theta/\pi$, and $\theta = \tan^{-1}(\sigma_{yx}/\sigma_{xx})$ is the Hall angle. The parameter k

above is the elliptic modulus, $0 < k < 1$, related to the sample aspect ratio via

$$\frac{L}{W} = \frac{K(k)}{2K(k')}, \quad k' = \sqrt{1-k^2}, \tag{2.12}$$

where $K(k)$ is the complete elliptic integral of the first kind.

In principle, Eqs.(2.10),(2.11),(2.12) give a complete solution of our problem. However, the integrals in Eq.(2.10) contain power-law singularities with the exponents $\delta_\pm = 1/2 \pm \theta/\pi$ that can approach unity for $\theta \approx \pm\pi/2$. This makes the integrals in Eq.(2.11) difficult to evaluate numerically, especially for large Hall angles, when the singularities are the strongest and the integrals are converging fairly slowly.

Instead, we use a different approach, developed in Ref. [103], which provides an expression of the electric field and current in the sample in terms of the exponentials of infinite but rapidly convergent sums. This method is more convenient for our purposes, because it allows to choose the integration contour for numerical evaluation of the conductance so that it bypasses the singularities.

In Ref. [103], the electric field components E_x and E_y at a point $z = x + iy$ are obtained as the real and imaginary parts of a suitable analytic function. The latter function is found to be of the form

$$E_y + iE_x = -e^{f(z)}, \tag{2.13}$$

where

$$f(z) = i\theta - \sum_{n>0\,(\text{odd})} \frac{4\theta}{n\pi} \frac{\sinh(n\pi iz/W)}{\cosh(n\pi L/2W)}. \tag{2.14}$$

Current distribution can be obtained by combining (2.13) with the relation $j_x + ij_y = (\sigma_{xx} + i\sigma_{yx})(E_x + iE_y)$.

Once the current distribution is found, it can be used to obtain the two-terminal conductance

$$G = I/V, \tag{2.15}$$

where I is the total current and V is the source-drain bias voltage. To evaluate

the net current I by integrating current density, one has to choose a cross-section through the sample that does not pass through its corners, where the function $f(z)$ has singularities. It is particularly convenient to perform this integration along a straight line that cuts through the middle of the rectangle at $y = 0$ (along the x-axis in Fig.2-1 inset):

$$I = \int_0^W j_y(x, 0)dx. \tag{2.16}$$

Since $j_y = \sigma_{xx}E_y + \sigma_{yx}E_x$, the current is given by

$$I = \int_0^W \sigma_{xx}(E_y(x, 0) + \tan\theta E_x(x, 0))dx. \tag{2.17}$$

For similar reasons, we calculate the voltage drop between the upper and lower contacts ($y = \pm L/2$) as an integral of the electric field along a straight line connecting the points $(W/2, -L/2)$ and $(W/2, L/2)$ of the contacts:

$$V = -\int_{-L/2}^{L/2} E_y(W/2, y)dy. \tag{2.18}$$

Evaluating the integrals (2.17) and (2.18) numerically, we obtain the conductance (2.15) as a function of transport coefficients, which defines its dependence on electron density. The results for different aspect ratios L/W for the monolayer and the bilayer case are displayed in Fig.2-2 and Fig.2-3 for two different values of the Landau level width parameters in (2.8), $\lambda = 1.7$, 0.5.

As evident from Fig.2-2, the conductance behavior depends strongly on the sample aspect ratio L/W. For a square sample, $L = W$, the conductance is a monotonic function of density at positive and negative ν, rising in steps associated with QHE plateaus. In this case, the behavior of G is found to be completely flat near $\nu = 0$ in agreement with the above discussion based on Eq.(2.1).

For $L \neq W$, the conductance turns into a nonmonotonic function of density, with the QHE plateaus being less pronounced than for $L = W$. For $L < W$ the conductance has minima near QHE plateau centers, Eq.(2.5) for the monolayer, and Eq.(2.6) for the bilayer case (marked by arrows in Figs.2-2,2-3), while for $L > W$

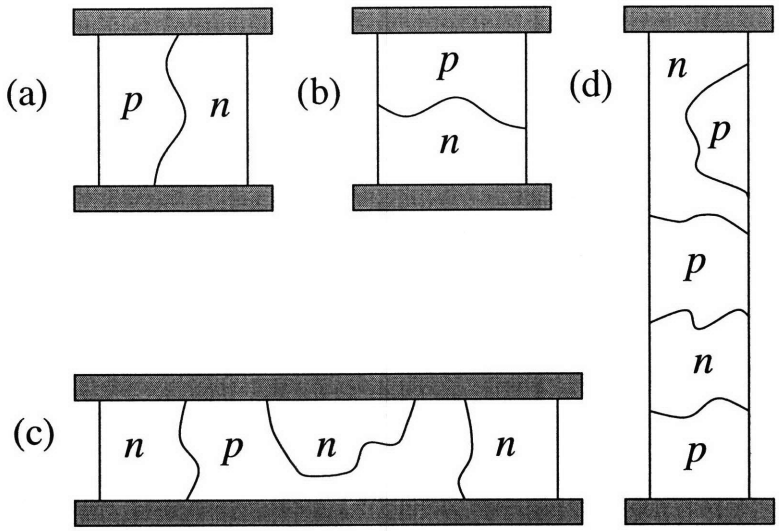

Figure 2-4: Examples of possible p-type and n-type puddle configurations near graphene charge neutrality point for mesoscopic samples with at least one of the dimensions comparable to the typical puddle size ξ. In (a) and (b) two possible configurations are shown for a square sample with $L, W \approx \xi$. The corresponding conductance values, $G = 4e^2/h$ for (a) and $G = e^2/h$ for (b), are different from the value $G^* = 2e^2/h$ predicted by the effective medium (semicircle) model. Puddle arrangement in a short and wide sample ($L \lesssim \xi \ll W$) and in a narrow and long sample ($W \lesssim \xi \ll L$) is illustrated in (c) and (d).

the conductance has maxima at these densities. Overall, the conductance behavior for $L < W$ is "inverted" compared to that for $L > W$, as expected from the duality relation (2.4) which implies

$$G_{L<W} > G_{L=W} > G_{L>W}$$

for all ν. Recently, the conductance as a function of carrier density was studied for samples of several aspect ratios [111], with the results being in qualitative agreement with ours. We shall discuss the data and compare it to out theory in the next Chapter.

With these results at hand we are now in position to ask which differences between the monolayer and bilayer systems are robust with respect to Landau levels' broadening and variation in sample geometry. First, we note that the centers of the QHE plateaus (arrows in Figs.2-2,2-3) remain close to the positions of the minima in G for $L < W$, and its maxima for $L > W$. The corresponding incompressible values of the density, Eqs.(2.5),(2.6), which are marked by arrows in Figs.2-2, 2-3, are

equally spaced in the monolayer case, but are *not equally spaced* in the bilayer case due to the eight-fold Landau level degeneracy at $\nu = 0$. It can be seen by comparing Fig.2-2 and Fig.2-3 that this difference between the monolayer and bilayer systems is not masked by Landau levels' broadening or by the aspect ratio variation.

Next, the conductance values at the minima for $L < W$ and at the maxima for $L > W$ remain close to the associated QHE values $G \approx \nu_n e^2/h$, which are different in the monolayer and bilayer cases. This difference is clear in Figs.2-2,2-3 even for large aspect ratios and broadened Landau levels. In practice, however, these values may change as a result of added contact resistance. If this is the case, the relative positions of the plateaus in density, inferred from the arrangement of maxima and minima of G, are more robust than the conductance values at these densities.

Finally, we note the difference in the size of the peak at $\nu = 0$ as compared to the sizes of neighboring peaks at other compressible densities, found for the monolayer and bilayer at $L < W$. (The same is true for the dip at $\nu = 0$ for $L > W$.) In the monolayer case, the size of the $\nu = 0$ peak/dip is comparable to the sizes of neighboring peaks/dips, whereas in the bilayer case the $\nu = 0$ peak/dip is almost two times larger than its neighbors. This difference reflects the higher density of states in the $\nu = 0$ Landau level of a bilayer.

It is also interesting to note that the heights of all peaks and dips in G are completely independent of the Landau level broadening, as can be seen by comparing the curves in Fig.2-2 and Fig.2-3. This behavior is specific to the semicircle model, in which the peak values of σ_{xx} and corresponding values of σ_{xy} are universal. Indeed, as evident from Fig.2-1, peaks of σ_{xx} line up with steps in σ_{xy}, and the values of σ_{xy} in the middle of each step are independent of the Landau level broadening. As a result, although broadened Landau levels change the overall behavior of the conductance G, the peak values remain intact.

2.6 Conductance fluctuations in small samples

So far we have described the system by a spatially uniform conductivity, assuming this effective medium model to be valid at all filling factors. This assumption, adequate for large samples, breaks down for smaller samples when the sample dimensions L or W become comparable to the typical charge inhomogeneity length scale ξ. Conductance of such small samples at QHE transitions can exhibit strong sample-to-sample fluctuations and significant deviations from the prediction of the semicircle model.

The effect of charge inhomogeneity is expected to be especially strong near the charge-neutrality point (CNP), where the density of free carriers is low and screening of the disorder potential is poor, for both the monolayer and bilayer graphene. For simplicity, below we shall focus on the monolayer graphene in the vicinity of the CNP, $\nu \approx 0$. To qualitatively understand the effect of charge inhomogeneities, we employ the two-phase model [104] treating the sample as a mixture of incompressible puddles of types n and p of typical size ξ. The filling factors in the puddles are $\nu = \pm 2$, corresponding to the QHE plateaus adjacent to CNP.

To illustrate the effect of strong fluctuations near the CNP, we first inspect the case of a small square sample, with both dimensions L and W comparable to ξ. Suppose that the carriers in such a sample form just two puddles, of type p and n ($\nu = \pm 2$). There are two topologically distinct puddle configurations giving the net conductance different from the value $G^* = 2e^2/h$ expected from the semicircle relation: (i) the p-n boundary connecting the source and the drain (see Fig.2-4a) (ii) the p-n boundary connecting the opposite free edges of the sample (see Fig.2-4b).

In the case (i) the p and n regions are connected in parallel, and thus the net conductance is the sum of the conductances $G_0 = 2e^2/h$, giving $G = 2G^* = 4e^2/h$. In the case (ii) the p and n regions are connected in series, with the net conductance equal $G = 1/2G^* = e^2/h$ (see Ref. [101]). Thus for mesoscopic square samples with $L, W \sim \xi$ the conductance strongly depends on the puddle configuration and can exhibit either a peak or a dip at $\nu = 0$, whereas the semicircle model predicts a plateau.

Now let us consider a sample which is short but wide: $L \lesssim \xi \ll W$ (see Fig.2-4c). Such a sample consists of about $N \sim W/\xi$ alternating p and n regions of width $\sim \xi$. The total conductance is given by the sum of the conductances of the individual regions, the conductance of each region being $G_0 = 2e^2/h$. This yields the net conductance of $G \sim NG_0 = (2W/\xi)\frac{e^2}{h}$. This is about L/ξ smaller than the value $G^* = (2W/L)\frac{e^2}{h}$ predicted by the semicircle relation for the effective medium model.

Similarly, for the case of a narrow but long sample, $W \lesssim \xi \ll L$ (see Fig.2-4d) the conductance is given by the series conductance of $N \sim W/\xi$ puddles: $G \sim (2\xi/L)\frac{e^2}{h}$. This is ξ/W times larger than than the prediction of the effective medium model. These estimates show that near CNP the semicircle model overestimates the conductance of very short samples, and underestimates the conductance of very narrow samples, when at least one of the sample dimensions is comparable to the puddle size.

2.7 Rectangle as the mother of all shapes; conformal invariance and universality

There is a profound relation between the two-terminal conductance and conformal invariance of the 2d transport problem. It arises because for 2d conductors of arbitrary shapes with spatially uniform σ_{xx} and σ_{xy} the conductance is invariant under conformal transformations, and because all single-connected domains in the plane can be conformally mapped to one another. As a result, a conducting domain of any shape has the same conductance as a particular domain of some simple shape with an appropriate arrangement of contacts. The simple shape can be chosen in a number of ways, in particular it can be chosen to be a rectangle. We show in this section that for a conductor of any shape with any configuration of two contacts *the conductance is equal to that of a rectangle* with some aspect ratio L/W.

Because the correspondence between conductors of arbitrary shapes and equivalent rectangles is purely geometric (it is defined by a conformal mapping), the aspect ratio

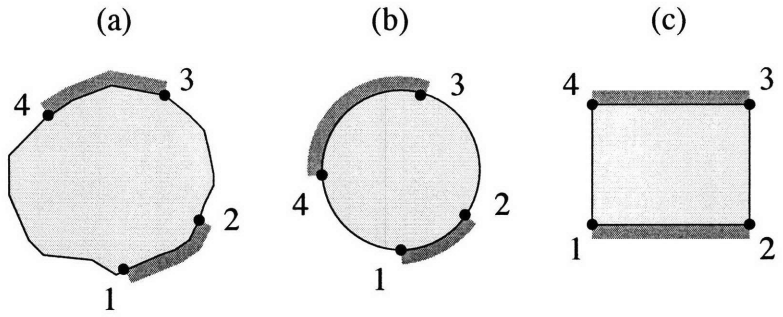

Figure 2-5: Conformal invariance illustrated by several conducting domains with contacts. If two domains can be conformally mapped on each other so that the contact regions are mapped on the corresponding contact regions, their conductances are the same. The Riemann mapping theorem guarantees existence of a mapping between an arbitrary domain (a) and a unit disk (b) such that three points on the boundary of (a), marked 1, 2 and 3, are mapped on any three points (1, 2 and 3) on the circle (b). The position of the fourth point, which is not specified, defines a one-parameter family of possible conduction problems. All such problems can be parameterized by rectangles (c) with different aspect ratios.

L/W of an equivalent rectangle depends on the sample shape but does not depend on the values of transport coefficients σ_{xx} and σ_{xy}. As a result, one can use the rectangle problem with a fixed aspect ratio to describe conductance as a function of the carrier density, via the σ_{xx} and σ_{xy} density dependence.

To formulate the constraints due to conformal invariance, we recall that conformal mappings in 2d are realized as analytic functions of the complex variable $z = x + iy$. Thus we consider mappings between two complex planes z and w defined by analytic functions $w = f(z)$, which map the sample domain (hereafter denoted $\mathcal{D}$) in the plane z onto a domain $\mathcal{D}'$ in the plane w.

The relations (2.2) as well as the boundary conditions $E_{\|} = 0$ on the contacts and $j_{\perp} = 0$ on the open boundary are invariant under such conformal mappings. The easiest way to verify this is to note that the current continuity condition $\nabla \cdot \mathbf{j} = 0$ can be solved by $\mathbf{j} = \nabla \times (\mathbf{z}\varphi(x, y))$, where $\mathbf{z}$ is the unit vector normal to the plane. Then the relation $\nabla \times \mathbf{E} = 0$ combined with $j_x + ij_y = (\sigma_{xx} + i\sigma_{yx})(E_x + iE_y)$ means that the function φ is harmonic, i.e. it satisfies the Laplace's equation

$$\left(\partial_x^2 + \partial_y^2\right) \varphi(x, y) = 0. \tag{2.19}$$

Because a harmonic function remains harmonic under a conformal mapping, and because the angles between the gradient $\nabla\varphi(z)$ and the boundary of $\mathcal{D}$ are the same as the angles between $\nabla\varphi(w)$ and the boundary of $\mathcal{D}'$ at corresponding points, Eqs.(2.2) as well the relations $E_{\|} = 0$ and $j_{\perp} = 0$ are indeed conformally invariant.

This simple mathematical fact can serve as a platform for the following interesting observation. Suppose an analytic function $w = f(z)$ maps the conducting domain $\mathcal{D}$ in the plane z to a domain $\mathcal{D}'$ in the plane w so that a pair of contacts to $\mathcal{D}$ is mapped on a pair of contacts to $\mathcal{D}'$. More precisely, let four points $1, 2, 3, 4$ on the boundary of $\mathcal{D}$ be mapped onto four points $1', 2', 3', 4'$ on the boundary of $\mathcal{D}'$. Let the arcs $1-2$, $3-4$ and $1'-2'$, $3'-4'$ be ohmic contacts for the problems in the z and w planes, respectively (see Fig.2-5). Then the two-terminal conductance of $\mathcal{D}$ is exactly the same as that of $\mathcal{D}'$, i.e the conductance is invariant under all conformal mappings that map to one another the corresponding conducting domains and contacts.

On the other hand, as is well known from the theory of complex variables (the Riemann mapping theorem), any two single-connected domains $\mathcal{D}$ and $\mathcal{D}'$ can be mapped onto each other. This mapping can be fixed so that any three points on the boundary of $\mathcal{D}$ are mapped to any three points on the boundary of $\mathcal{D}'$ (under these conditions the mapping is unique). This allows to reduce the conductance problem of an arbitrary domain $\mathcal{D}$ to that of some simple domain, e.g. a circular disk $|w| \leq 1$.

Thus the only reason the conductors of different shapes do not all have the same conductance is the additional freedom in choosing the contacts, defined by the points $1, 2, 3, 4$. Furthermore, because any conduction problem is equivalent, via a conformal mapping, to a disk with contacts defined by four points on the boundary $z_1, ..., z_4 = e^{i\theta_1}, ..., e^{i\theta_4}$, and because three of those points can be fixed by the Riemann mapping theorem, the only freedom left is in the position of the fourth point. Therefore, all conductance problems form *a one-parameter family.* For the points $z_1, ..., z_4$ this parameter can be expressed, e.g., as the so-called cross ratio

$$\Delta_{1234} = \frac{(z_1 - z_4)(z_3 - z_2)}{(z_1 - z_2)(z_3 - z_4)} \tag{2.20}$$

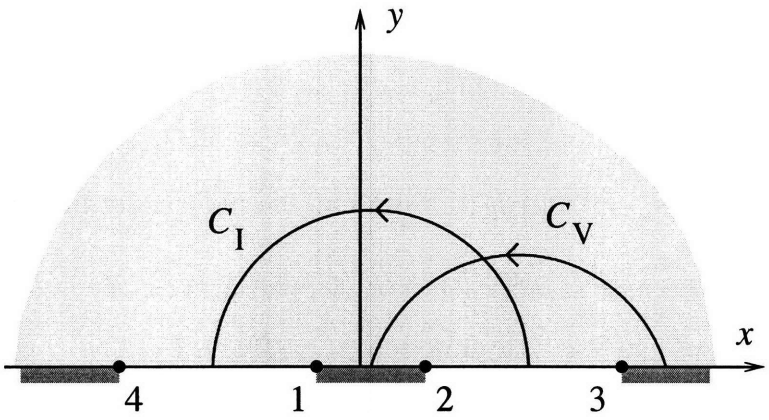

Figure 2-6: Complex halfplane and conduction problem in it, which can be mapped on that in a rectangle using the Schwartz-Christoffel mapping, Eq.(2.23). The aspect ratio L/W of the equivalent rectangle depends on the relative size of the contacts, shown in blue, and the distance between them. The end points of the contacts are $\xi_{1,2} = \mp 1$, $\xi_{3,4} = \pm 1/k$.

which takes real values for any four points that lie on a circle. Applied to the problem of a rectangle, this procedure would give a one-to-one relation between the parameters L/W and Δ_{1234}, proving that indeed any conductance problem is isomorphic to that of a rectangle.

To obtain such a relation between L/W and Δ_{1234}, let us consider a complex halfplane $\mathrm{Im}\,\xi > 0$ with four points on the real axis

$$\xi_{1,2} = \mp 1, \quad \xi_{3,4} = \pm 1/k, \tag{2.21}$$

with the parameter $0 < k < 1$ (see Fig.2-6). Under a fractional-linear mapping that maps the unit disk to the halfplane, the points $z_1, ..., z_4$ can be mapped onto corresponding points (2.21) if and only if the cross ratios are the same:

$$\Delta_{1234} = (1 - k^2)/4k \tag{2.22}$$

(the cross ratio is an invariant of fractional linear mappings). On the other hand, using the Schwartz-Christoffel formula, the halfplane $\mathrm{Im}\,\xi > 0$ can be mapped on a

rectangular domain by the function

$$z = F(\xi, k) \equiv \int_0^{\xi} \frac{d\xi'}{\sqrt{(1-\xi'^2)(1-k^2\xi'^2)}}, \tag{2.23}$$

where $F(\xi, k)$ is the elliptic integral of the first kind. This function maps $\xi_{1,2} = \mp 1$ to $z_{1,2} = \mp K(k)$, where

$$K(k) = \int_0^1 \frac{d\xi}{\sqrt{(1-\xi^2)(1-k^2\xi^2)}} \tag{2.24}$$

is the complete elliptic integral of the first kind. The points $\xi_{3,4} = \pm 1/k$ are mapped to $z_{3,4} = \pm K(k) + iK(k')$, where $k' = \sqrt{1-k^2}$. Thus the sides of the rectangle have lengths $W = 2K(k)$ and $L = K(k')$, which gives the relation between L/W and k of the form (2.12). Combining this with (2.22), we can relate L/W to the cross ratio Δ_{1234}.

In the halfplane of Fig.2-6 the distribution of the electric field and current can be found by noting that the function $E(\xi) = E_y + iE_x$ is analytic at $\mathrm{Im}\,\xi > 0$ and at the boundary its argument takes fixed values between the points $\xi_1, ..., \xi_4$: $\arg E_{-1<\xi<1} = 0$, $\arg E_{1<\xi<1/k} = \frac{\pi}{2} + \theta$, $\arg E_{-1/k<\xi<-1} = -\frac{\pi}{2} + \theta$, $\arg E_{|\xi|>1/k} = -\pi$. These requirements are sufficient to reconstruct the function:

$$E(\xi) = \frac{A}{(1-\xi)^{\delta_+}(1+\xi)^{\delta_-}(1-k\xi)^{\delta_-}(1+k\xi)^{\delta_+}}, \tag{2.25}$$

where $\delta_{\pm} = \frac{1}{2} \pm \frac{\theta}{\pi}$ with $\theta = \tan^{-1}\sigma_{yx}/\sigma_{xx}$ the Hall angle, as in (2.11), and the unknown prefactor A depends on the source-drain voltage. Current distribution is then found as $J(\xi) = j_y + ij_x = (\sigma_{xx} + i\sigma_{xy})E(\xi)$. The total current and voltage can be expressed by integrating $J(\xi)$ over the contour C_I, and $E(\xi)$ over the contour C_V (see Fig.2-6). The ratio of these integrals gives the result (2.10).

To summarize our discussion, because the conductor of an arbitrary shape can be conformally mapped on a rectangle which has the same conductance, the rectangle problem is "universal." For a sample of any shape with a pair of contacts of arbitrary size and form, an equivalent rectangle can be found such that it has the same

conductance. Crucially, the aspect ratio L/W of this rectangle is independent of the values of transport coefficients, which means that its conductance will have the same density dependence as that of the physical sample.

We note that, although the results of this section apply to conductors of completely arbitrary shapes, and in that sense they are far reaching, there are several limitations. First, we have assumed that the electron system is spatially uniform and homogeneous, i.e. the transport coefficients σ_{xx} and σ_{xy} are position-independent. Our second assumption was that transport is fully described by the 2d current-field relation $\mathbf{j} = \hat{\sigma}\mathbf{E}$, where $\hat{\sigma}$ is the conductivity tensor. In particular, the above model does not allow for the edge current states, which could, in principle, alter the shape dependence of the conductance. Still, since the bulk transport model agrees with the edge transport model in the limit of a large Hall angle, it can probably provide a good guidance even when the quantum Hall effect is fully developed.

2.8 Conclusions

The above results for the two-terminal conductance of rectangular samples, and in particular, the conductance dependence on the sample aspect ratio, can serve as a benchmark for understanding properties of graphene samples. We found that G exhibits peaks (dips) at the compressible densities for $L < W$ ($L > W$), which completely disappear at $L = W$. We could identify several specific features that may help to distinguish between transport in graphene monolayer and bilayer. Those include positions of the incompressible densities, inferred from minima (maxima) in G at $L < W$ ($L > W$), the values of G at these densities, and the relative size of the central peak (dip) in G as compared to the neighboring peaks. These features, which are shown to be insensitive to the sample aspect ratio and to Landau levels' broadening within our model, can be used for sample diagnostic in transport measurements.

Chapter 3

Two-Terminal Conductance of Graphene Devices in the Quantum Hall Regime

3.1 Abstract

We report measurements of the two-terminal conductance of single-layer and bilayer graphene in the quantum Hall regime. Conductance values at the Hall plateaus and at charge neutrality, as well as the positions of the local conductance extrema, are found to be layer-number and device-geometry dependent. Qualitative agreement is found with the theory of two-terminal graphene conductance presented in the previous Chapter, and it is found experimentally that the geometric dependence of conductance can be described by a single parameter ξ_e. Possible origins for discrepancies found between ξ_e and the actual device aspect ratio are discussed.

3.2 Introduction

In contrast to graphene monolayer, graphene bilayer has a quadratic elecron-hole symmetric excitation spectrum, leading to QH conductance values $g_{xy} = 4n\,e^2/h$, $n = \pm 1, \pm 2, ...$ that are distinct from the half-integer QH values 1.13 of the single-layer

graphene [78, 32]. These QH signatures have served to elucidate the band structure of these carbon materials, and as an experimental tool for identifying number of layers and for characterizing sample quality [32].

Experimentally, two-terminal conductance measurements in the QHE regime are often used for sample diagnostic [89, 9]. Interpretation of the two-terminal conductance data, however, is typically not as straightforward as the conductance measured by the multi-terminal methods [112]. The two-terminal conductance is of interest because the conventional resistance measurement schemes, while having a number of advantages over the two-probe method, can be difficult to implemented in a nanoscale conductor. The two-terminal quantized conductance plateaus in single-layer graphene have been previously reported [9, 10, 89] mainly to identify the device as a single layer. However, often the conductance quantization is poor and/or the values of conductance on the Hall plateaus can differ greatly from the quantized values for both the single- and bilayer graphene. This is especially common for the samples with a two-terminal device geometry other than a square, suggesting that the geometric dependence must be taken into account when interpreting two-terminal conductance measurements.

We investigate the QH conductance of two-terminal graphene devices, focusing on the dependence on layer number and device geometry. We demonstrate experimentally how two-terminal conductance features can be used to discern monolayers and bilayers even when conductance quantization is poor, in agreement with theory [7] presented in the previous Chapter. Specifically, we use the positions of the conductance minima and maxima as well as conductance behavior near the charge-neutrality point (CNP). Below we study five two-terminal samples of different geometry, four rectangular devices with aspect ratio $\xi_s = L/W$ ranging from 0.15 to 2.5, and one with asymmetric contacts (see Table 1).

In our discussion of the geometric dependence of two-terminal conductance of QH graphene samples in the previous Chapter we have shown that the conduction problem for a sample of an arbitrary geometry can be reduced to that for an equivalent rectangular sample. Here we test that prediction experimentally and find that the geometric dependence can be reasonably described by a single parameter, the equivalent

Table 3.1: Measured two-terminal graphene devices

Sample	Number of Layers	(L, W) (μm)	ξ_s	ξ_e
A1	Monolayer	(1.3, 1.8)	0.72	1.67
A2	Monolayer	(0.35, 2)	0.18	0.2
B1	Bilayer	(2.5, 1)	2.5	0.8
B2	Bilayer	(0.3, 2)	0.15	0.29
C	Monolayer	Asym. contacts	0.9[1]	0.83

rectangle's aspect ratio ξ_e, even when the device geometry is not rectangular.

Transport in the QH regime is sensitive to the band structure of the material. For both single-layer and bilayer graphene, the unique gapless energy dispersion results in the existence of a fully formed Landau level (LL) at zero energy [91, 60], which is absent in the gapped bilayer system [113, 114]. The behavior of the two-terminal conductance for three cases [Fig. 3-1a - gapless Dirac fermions, Fig. 3-1b - gapless bilayer graphene, and Fig. 3-1c - gapped bilayer graphene] is shown schematically in Fig. 3-1. The eight-fold degeneracy of the zero-energy Landau level in bilayer graphene [60] leads to conductance value near the CNP that is larger than for a monolayer. A non-zero value of conductance at zero density for single and bilayer graphene is in contrast to what is expected for a gapped graphene bilayer, where the LL at zero energy splits up, producing a vanishing conductance at $\nu = 0$.

Device geometry can also alter the behavior of the two-terminal conductance in the QH regime, giving rise to additional conductance maxima or minima that replace the QH plateaus. Traces, shown in Fig. 3-1, illustrate phenomenologically the possible conductance behavior for two different device aspect ratios ($\xi_e = 2$ and 0.5) for all three band structures. Conductance features observed in our samples are qualitatively similar to those in Fig. 3-1a and 3-1b, indicating that the studied samples are of monolayer and gapless bilayer type.

3.3 Conductance of single-layer graphene samples

Graphene devices were fabricated by mechanically exfoliating highly oriented pyrolytic graphite [25] onto a n^{++} Si wafer capped with $\sim 300\,\mathrm{nm}$ of SiO_2. Potential

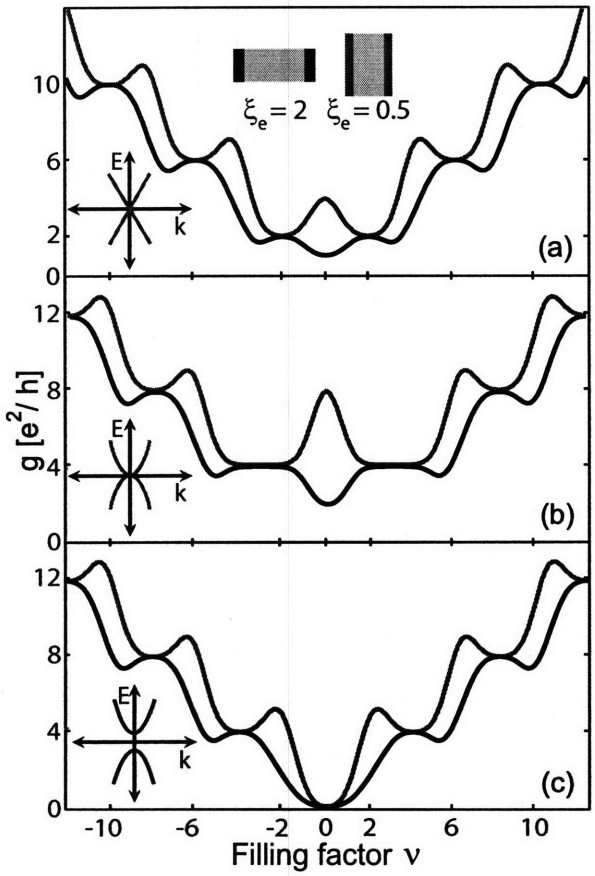

Figure 3-1: Theoretical density-dependent two-terminal QH conductance g as a function of carrier density obtained using Ref. [7] (see text for details) shown for (a) single-layer graphene; (b) gapless bilayer graphene, and (c) gapped bilayer graphene. Black and red curves correspond to aspect ratios $\xi_e = L/W = 2$ and 0.5. Local extrema of g at filling factors $\nu = \pm 2, \pm 6, \pm 10..$ for single layers and at $\nu = \pm 4, \pm 8, \pm 12..$ for bilayers are either all maxima ($\xi_e < 1$) or all minima ($\xi_e > 1$). In (a) and (b), the local extremum at $\nu = 0$ is of opposite character (i.e., mimimum for $\xi_e < 1$ and maximum for $\xi_e > 1$). In (c), due to the gap, g vanishes at $\nu = 0$ regardless of geometry.

single and bilayer graphene flakes were identified by optical microscopy. Source and drain contacts, defined by electron beam lithography, were deposited by thermally evaporating 5/40 nm of Ti/Au. Two-terminal conductance measurements were performed on five samples. The ξ_s for each sample was determined by either optical or scanning electron microscopy.

Devices were measured in a ^{3}He refrigerator allowing dc transport measurements in a magnetic field $|B| < 8\,\mathrm{T}$ perpendicular to the graphene plane. Unless otherwise noted, all measurements were taken at base temperature, $T \sim 250\mathrm{mK}$. Differential

conductance $g = dI/dV$, where I is the current and V the source-drain voltage, measure using a current-bias configuration (I chosen to keep $eV < k_BT$) was obtained using a standard lock-in technique at a frequency of 93Hz. All samples show $B = 0$ characteristics of high-quality single-layer and bilayer graphene [4, 30]: a CNP positioned at back-gate voltage $V_{\rm bg} \sim 0$ and a large change in g (in excess of $20\,e^2/h$) over the $V_{\rm bg}$ range of $\pm 40\,$V.

Figure 3-2a (black trace) shows measured $g(V_{\rm bg})$ for sample A1 (ξ_s=0.72) at B= 8 T. Plateaus in conductance are observed at filling factors $\nu = \pm 2$ near, but not equal to $2\,e^2/h$, with values of $\sim 2.7\,e^2/h$ and $\sim 2.3\,e^2/h$ on the hole and electron side of the CNP, respectively. At $\nu = 0$ ($V_{\rm bg} \sim 2.3$V), g departs from the quantized values, dropping to a minimum of $\sim 1.4e^2/h$. At higher densities, the conductance exhibits a series of maxima with values slightly above 6, 10, $14\,e^2/h$. Maxima on the hole side consistantly have slightly higher values, a feature observed in all the samples measured. The inset of Fig. 3-2a shows g in the QH regime as a function of $V_{\rm bg}$ and B. Dashed black lines indicate the filling factors $\nu = n_s h/eB$ (where n_s is the carrier density) of -6, -10, and -14 and lines align with the local *maxima* of $g(V_{\rm bg})$. $V_{\rm bg}$ was converted to n_s using a parallel plate capacitance model[25], giving $n_s = \alpha(V_{\rm bg} + V_{\rm offset})$ with $\alpha = 6.7 \times 10^{10}{\rm cm}^{-2}{\rm V}^{-1}$ and $V_{\rm offset} = 2$V.

Measured $g(V_{\rm bg})$ [black curve in Fig. 3-2b] for sample A2 ($\xi_s = 0.18$) shows distinctive differences from the measured $g(V_{\rm bg})$ in sample A1. In particular, at the CNP ($V_{\rm bg} = -1.5$V), g exhibits a sharp peak with a maximal value of $\sim 8.8\,e^2/h$. Away from the CNP, the conductance has maxima which are much stronger than those in sample A1. The inset of Fig. 2(b) shows $g(V_{\rm bg}, B)$. For this sample, the dashed lines representing the incompressible filling factors $\pm 6, \pm 10, \pm 14$ now align with the *minima* in g. Here we used the $V_{\rm bg}$ to n_s conversion factors of $\alpha = 6.7 \times 10^{10}{\rm cm}^{-2}{\rm V}^{-1}$ (the same as for sample A1) and $V_{\rm offset} = -1.1$V.

The observed features in g for samples A1 and A2 can be compared to theory for two-terminal quantum Hall conductance developed in the previous Chapter. The filling factor dependence of the conductivity tensor is obtained using the semicircle relation [104] and the current density distribution for a rectangular sample with an

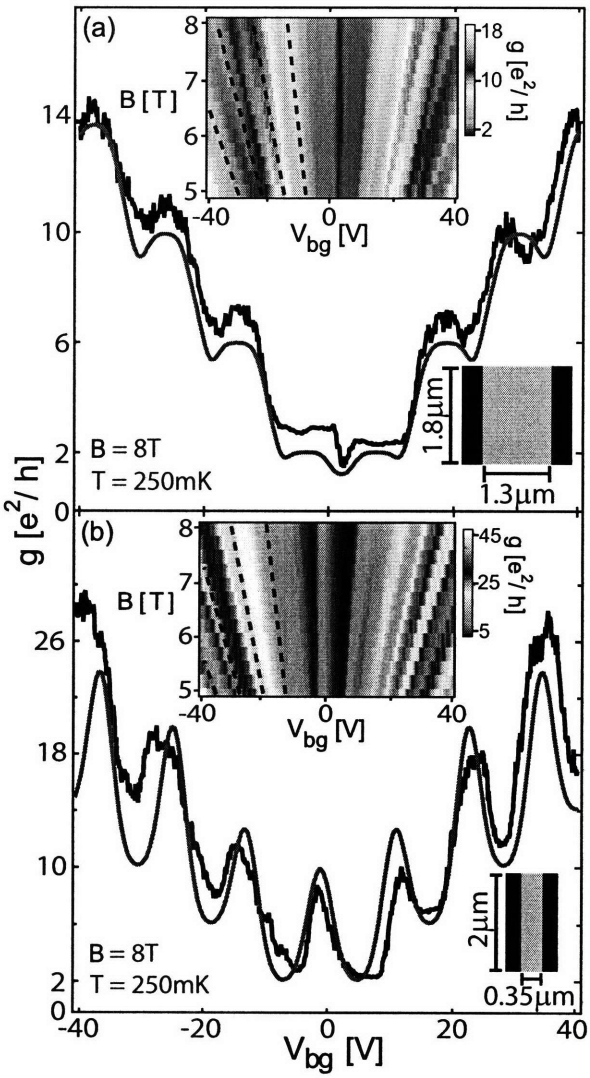

Figure 3-2: (a) Inset: Conductance g in the quantum Hall regime as a function of B and V_{bg} at T=250mK for sample A1. Black dashed lines correspond to filling factors of -6, -10, -14, -18 and align with the local *maxima* of conductance. Main: (black) Horizontal cut of inset giving $g(V_{\mathrm{bg}})$ at B=8T and (red) calculated g ($\xi_e = 1.67$ and $\lambda = 1.2$). (b) Inset: Conductance g in the quantum Hall regime as a function of B and V_{bg} at T=250mK for sample A2. Black dashed lines correspond to filling factors of -6, -10, -14, -18 and align with the local *minima* of conductance. Main: (black) Horizontal cut of inset giving $g(V_{\mathrm{bg}})$ at B=8T and (red) calculated g ($\xi_e = 0.2$ and $\lambda = 1.2$).

arbitrary aspect ratio is found analytically by conformal mapping [103]. The current density is then integrated numerically along suitably chosen contours to evaluate total current and voltage drop, from which g is obtained by $g = I/V$. The rectangular geometry was found to be universal in the sense that the conductance of an arbitrary

non-rectangular sample is equal to that of a rectangle with a effective aspect ratio ξ_e, which depends only on the sample geometry and not on the conductivity tensor.

The red curves in Figs. 3-2a and 3-2b show the best-fit calculated conductance obtained following Ref. [7]. The aspect ratio parameter value, found from best fit, is $\xi_e = 1.67$ for sample A1. The Landau level broadening is described by a gaussian $e^{-\lambda(\nu-\nu_n)^2}$ and is quatified through the parameter λ, with λ=1.2 for sample A1. This theoretical curve reproduces the essential features of the data: local maxima align with the filling factors $\pm 2, \pm 6, \pm 10$, ..., and g exhibits a dip at the CNP.

The alignment of conductance minima with the incompressible densities, as well as a peak at the CNP, observed for sample A2, are also in agreement with theoretical predictions for wide samples. As illustrated in Fig. 3-2b (red curve), the data is well described by the effective aspect ratio $\xi_e = 0.2$ and is close to the actual value $\xi_s = 0.18$.

The size of peaks and dips in Fig. 3-2a and Fig. 3-2b grows for higher LL. This is a general trend, which is observed in all our monolayer samples except for sample C. The model, on the contrary, predicts that peaks and dips at $|\nu| > 0$ LLs have similar size. This discrepancy may be attributed to inapplicability of the two-phase picture of Ref. [104], from which the semicircle law is derived, in higher LLs. Indeed, because for Dirac particles the spacing between LLs decreases at higher energies as an inverse square root of the level number, one may expect mixing between non-nearest LLs to increase at high energies. Such mixing can lead to the longitudinal conductivity values in excess of those obtained in Ref. [104] by accounting only for mixing between nearest levels (see also discussion in Ref. [110]).

To take these effects into account, we have extended the model of of the previous Chapter phenomenologically, assuming that the contribution of the n^{th} LL $(\delta_n\sigma_{xx}, \delta_n\sigma_{xy})$ to the conductivity tensor in monolayer graphene is described by a modified semicircle, or an elliptic law,

$$\delta_n\sigma_{xx}^2 + A_n^2(\delta_n\sigma_{xy} - \sigma_{xy,n}^0)(\delta_n\sigma_{xy} - \sigma_{xy,n'}^0) = 0, \tag{3.1}$$

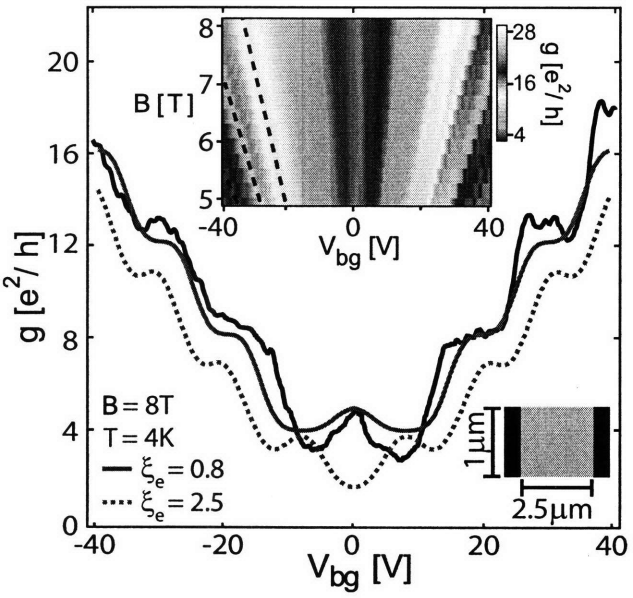

Figure 3-3: Inset: Measured g of sample B1 as a function of B and $V_{\rm bg}$ at $T = 4K$. Black dashed lines, corresponding to ν= -12, -16, -20, align with local *minima* of g. No minima are observed at $\nu = 8$ for $5T < B < 8T$. Main: Horizontal cut of inset at $B = 8T$ (black), and calculated g (red) using $\lambda = 0.7$ and effective aspect ratio $\xi_e = 0.8$ (solid) and $\xi_e = 2.5$ (dashed).

where $\sigma^0_{xy,n}, \sigma^0_{xy,n'}$ are the quantized Hall conductivities at the neighboring plateaus, and A_n is a factor which equals unity for 'usual' semicircle law. To explain the data for samples A1 and A2, we take values $A_n \approx 1$ for $n = 0, \pm 1$, and $A_n \approx 2$ for other LLs, consistent with the previous experiment[4] (see Ref. [110]).

3.4 Conductance of bilayer graphene samples

The black curve in Fig. 3-3 shows measured $g(V_{\rm bg})$ for sample B1 ($\xi_s = 2.5$) at B= 8 T and T=4K. This sample has two features which indicates that it is bilayer graphene: plateaus in conductance appearing near 4, 8, 12 and 16 e^2/h and a conductance maxima at the CNP that is much larger that then extrema at higher density. The conductance values at the plateaus $\nu = \pm 4$ here are lower than the expected $4\,e^2/h$ for a bilayer sample, falling to $3.1(2.7)\,e^2/h$ on the hole(electron) side of the CNP. The peak value in conductance at $\nu = 0$ is at $5\,e^2/h$ at a $V_{\rm bg} = 0.5\,$V. At higher filling factors, the plateaus exhibit two different behaviors, showing a very flat

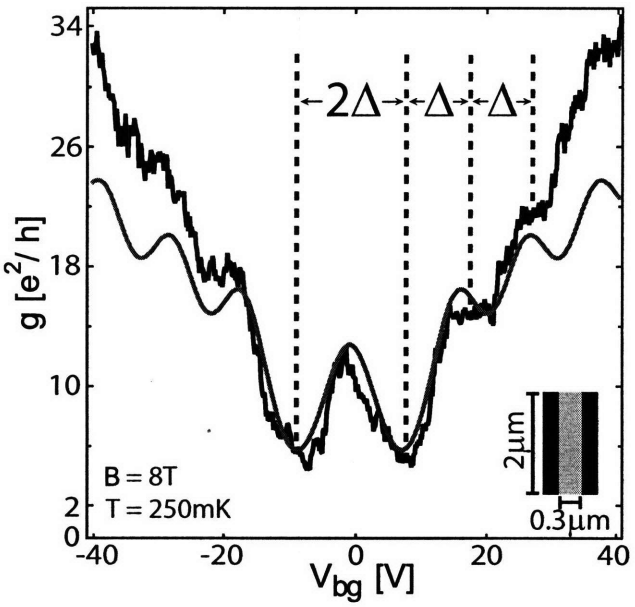

Figure 3-4: Measured $g(V_{\rm bg})$ for sample B2 (black) and the calculated conductance for $\xi_e = 0.29$ and $\lambda = 0.25$ (red). Two key features in the curve suggest this sample is a gapless bilayer, namely, a pronounced peak in g near the CNP, and the larger spacing between the two minima straddling the CNP compared to the spacing $\Delta \sim 9.5$ between other consecutive minima.

plateau at $\nu = 8$ and a flat plateau followed by a dip at $\nu = 12$. The small dips align with the filling factors $\nu = 12, 16$ for $5\,\mathrm{T} < B < 8\,\mathrm{T}$ (see inset of Fig. 3), using $\alpha = 7.2 \times 10^{10}\mathrm{cm}^{-2}\mathrm{V}^{-1}$ and $V_{\rm offset} = 0.5\mathrm{V}$.

Theoretical g curves for aspect ratios $\xi_e = 2.5$ (actual geometry - dashed line) and $\xi_e = 0.8$ (best fit - solid line) are shown in red in Fig. 3-3. The predicted dependence g as a function of $V_{\rm bg}$ for the two aspect ratios are similar in structure at high density, but differ dramatically at $\nu = 0$, exhibiting a dip in conductance for $\xi_e = 2.5$ and a peak near the experimental value for $\xi_e = 0.8$. The curve for $\xi_e = 0.8$ is also in a better agreement with the data at higher densities: it reproduces the observed values of the conductance at the incompressible densities, while the curve for $\xi_e = 2.5$ underestimates the conductance.

In some other cases the quantized conductance values are found to be much further from the expected values than what is observed in samples A1, A2 and B1. Sample B2 (($\xi_s = 0.15$) demonstrates this behavior. At the CNP, g reaches a maximum value of $13.5\,e^2/h$, followed by a minimum to the left and right of the CNP of $5\,e^2/h$ (see

black trace in Fig. 3-4). Away from the CNP, two conductance plateaus appear at values of $\sim 16\,e^2/h$ and $23\,e^2/h$, neither of which are near the known values for single nor bilayer graphene. Since there are no strong peaks or dips in g away from charge neutrality, as is expected for a device with a ξ_s of 0.15, it is difficult to determine the number of layers from the location of the conductance extrema. There are two features, however, which allow for the identification of the underlying band structure of the device. First, the peak at $\nu = 0$ is much more pronounced than any other peak in the conductance. Second, the spacing in $V_{\rm bg}$ between the two lowest LL is twice as large as the spacing between any other two LL (in Fig. 4, $\Delta \sim 9.5\,\mathrm{V}$). Both of these features arise in bilayer graphene as a result of the zero-energy LL being eight-fold degenerate, twice as much as all other bilayer LLs and the zero-energy LL in single layer graphene[60]. The theoretical prediction, using a ξ_e of 0.29, for the bilayer sample B2 is shown in red in Fig. 3-4.

3.5 Non-rectangular samples

So far we have considered rectangular samples. What happens if the sample is non-rectangular, or the contacts are positioned asymmetrically? Sample C, shown schematically in the inset of Fig. 3-5, has these features. Surprisingly, the measured conductance of sample C (black curve in Fig. 3-5) has properties very similar to those expected for a square monolayer sample: around the CNP the conductance is nearly flat with value close to $2\,e^2/h$, monotonically increasing on the electron and hole sides at filling factors $|\nu| > 2$.

The data in Fig. 3-5 are reasonably accurately modeled by the red theoretical curve, obtained for the best-fit effective aspect ratio $\xi_e = 0.83$. Here we assume the LLs to be relatively broad ($\lambda = 0.7$), which somewhat masks the maxima at the LLs with $|n| \geq 1$. This choice of parameters yields a good agreement with the data for the range of filling factors $|\nu| \leq 6$. At higher fillings, the plateaus are washed out, suggesting that the LL broadening is stronger for LLs $|n| \geq 2$.

Due to sample C's relatively simple polygonal geometry, its effective aspect ratio

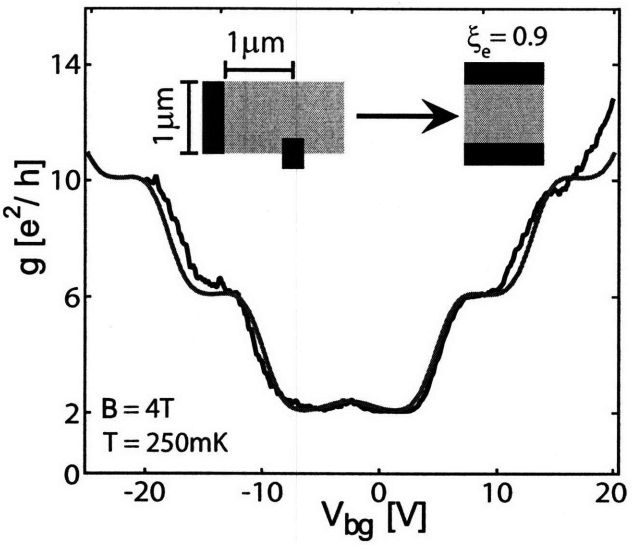

Figure 3-5: $g(V_{\rm bg})$ for sample C (black) and the calculated conductance (red) for the best-fit value of $\xi_e = 0.83$ ($\lambda = 0.7$). The observed conductance (black) can be reproduced by conformally mapping the asymmetric contact configuration into a rectangular shape (see inset), which for this device results in an equivalent rectangle of $\xi_e = 0.9$.

can be estimated analytically. For that, we construct a conformal mapping transforming sample C into the upper half-plane, which, in turn, can be mapped onto a rectangle. This yields the effective aspect ratio of $\xi_s \approx 0.9$, which is in a good agrement with the best-fit value $\xi_e = 0.83$ found above. In principle, the polygon pictured in Fig. 3-6 could be mapped onto the upper half-plane by inverting a Schwarz-Christoffel mapping. However, since this mapping is defined by a contour integral, the difficult inversion can only be done numerically. In order to circumvent this difficulty, we replace the rectangle by a semi-infinite strip [Fig. 3-7a)]. This approximation should not significantly affect the conductance, as the current flows mostly in the region between contacts 1-2 and 3-4.

The desired mapping can be constructed from two simple mappings, as illustrated in Fig. 3-7. Without loss of generality we set the length scale $a = 1$. Our first step is to straighten out the contact 3-5-6-4. We notice that the following mapping,

$$\tilde{z} - iA = \int_0^{\tilde{w}} \left(\frac{\xi^2 - 1}{\xi^2 - 2} \right)^{1/2} d\xi, \tag{3.2}$$

$$A = \int_0^1 \left(\frac{\xi^2 - 1}{\xi^2 - 2}\right)^{1/2} d\xi \approx 0.60, \tag{3.3}$$

maps the upper $\tilde{w}$ plane onto the upper $\tilde{z}$ plane with a removed rectangle having vortices

$$\tilde{z}_{3,4} = \pm A, \ \tilde{z}_{5,6} = \pm A + iA. \tag{3.4}$$

These points correspond to the points $\tilde{w}_{3,4} = \pm\sqrt{2}$, $\tilde{w}_{5,6} = \pm 1$ in the $\tilde{w}$ plane. The value of A ensures that the edge of the sample situated on x axis remains on the axis under the mapping (3.2). The distance between points $\tilde{z}_3$ and $\tilde{z}_5$ plane equals A, as follows from Eq. (3.2) and equality [115]

$$\int_1^{\sqrt{2}} \left|\frac{\xi^2 - 1}{\xi^2 - 2}\right|^{1/2} d\xi = A. \tag{3.5}$$

The removed recangle's aspect ratio is 2, the same as that for the contact 3-5-6-4, however, the two rectangle's dimensions differ by a factor of A. Scaling and shifting both $\tilde{z}$ in $\tilde{w}$,

$$\tilde{z} = A(z - 5), \ \tilde{w} = A(w - 5), \tag{3.6}$$

we obtain the required mapping which straightens out the contact 3-5-6-4.

The mapping (3.2), (3.6), while straightening the segments 3-5-6-4, distorts the rest of the boundary. However, we notice that far from the contact 3-5-6-4, $|z-5| \gg 1$, the mapping (3.2), (3.6) is an identity,

$$z(w \gg 1) = w + O(1/w). \tag{3.7}$$

Owing to this property and the relatively small size of the segments 3-5-6-4 compared to the strip width, the distortion is small. This is shown schematically in Fig. 3-7), where the yellow polygon portrays the image of the sample, with the deviation of its boundary from the original one (shown in red) exaggerated for clarity. The deviation is indeed small: by investigating the mapping (3.2), (3.6) numerically we found that the boundary is displaced the most at the point 2 which is shifted by approximately 0.3 away from its original position $2'$ along the real axis. This is small compared

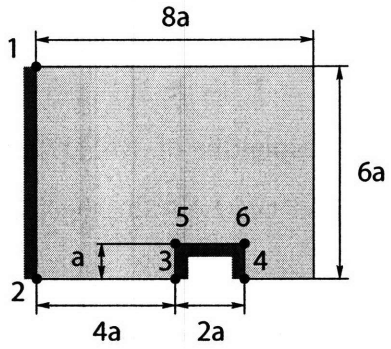

Figure 3-6: A polygon representing sample C (see Fig. 3-5). Blue regions correspond to contacts, length scale $a = 200\,\text{nm}$.

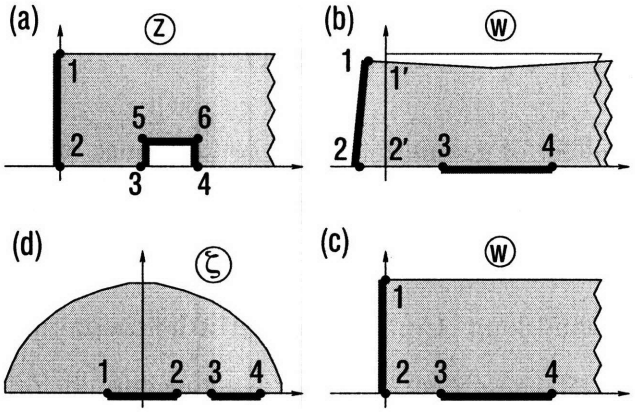

Figure 3-7: Mapping of the polygon in Fig. 3-6 (sample C) onto the upper half-plane (shown not to scale). Blue lines correspond to contacts. First, we replace the rectangle in Fig. 3-6 by a half-infinite strip, extending indefinitely to the right. Next, we map the domain shown in (a) onto a rectangle with contact 3-5-6-4 straightened out (b). Under this mapping, the sample is slightly distorted, as indicated by the yellow polygon in (b). Because the deviation of the yellow polygon's boundary from the original sample's boundary (red line in (b)) is fairly small, it can be neglected, giving a half-infinite strip (c). Finally, the domain (c) is mapped onto the upper half-plane (d), which allows to find the cross ratio Δ_{1234} and evaluate the effective aspect ratio (see text).

to the sample's width, which allows us to neglect the displacement of the boundary and assume that the mapping (3.2), (3.6) transforms the original geometry into the semi-infinite strip shown in Fig. 3-7b in red color.

After making this approximation, we transform the semi-infinite strip in Fig. 3-7c into the upper half-plane by the following mapping,

$$\zeta = \cosh\frac{\pi w}{6}. \tag{3.8}$$

In the ζ plane, the contacts are mapped on the real axis, with the end points 1, 2, 3 and 4 mapped to $\zeta_1 = -1$, $\zeta_2 = 1$, $\zeta_3 \approx 2.11$, $\zeta_4 \approx 23.57$. From these values, following the procedure in the Appendix of Ref. [7], we compute the cross ratio $\Delta_{1234} = \frac{(\zeta_1-\zeta_4)(\zeta_3-\zeta_2)}{(\zeta_1-\zeta_2)(\zeta_3-\zeta_4)} \approx -0.64$, and then obtain the aspect ratio $\xi_e = 0.9$ from the relations

$$\xi_s = \frac{L}{W} = \frac{K(k')}{2K(k)}; \quad \Delta_{1234} = (1-k^2)/2k, \tag{3.9}$$

where $K(k)$ is the complete elliptic integral of the first kind, and $k' = (1-k^2)^{1/2}$.

3.6 Summary and discussion

We have studied the effect of geometry on the conductance of two-terminal graphene devices in the QH regime. The quantized QH plateaus typically exhibit conductance extrema, with the observed extrema being stronger for the samples which are wide-and-short and narrow-and-long. Comparison with the theoretical model[7] discussed in Chapter 2 shows that these distortions can be accounted for by the effect of geometry. We find that the equivalent-rectangle model works reasonably well even for non-rectangular samples.

Furthermore, we find that for the short-and-wide samples ($\xi_e < 1$, samples A2, B1, B2) the local conductance minima occur at the incompressible filling factors, while for the effectively long-and-narrow samples ($\xi_e > 1$, sample A1) it is the conductance maxima. This, along with the behavior at the CNP, provides a clear way to identify the sample's number of layers even when the quantization is weak or absent (sample B2). These observations are all in qualitative agreement with theory.

We find that in all five samples the geometric dependence of the conductance is approximately described by a single parameter, the effective aspect ratio ξ_e of an equivalent rectangle. Surprisingly, the effective ratio ξ_e of several rectangular samples obtained from the conductance measurements differs significantly from their actual aspect ratio ξ_s: $\xi_e > \xi_s$ for A1 and B2, while $\xi_e < \xi_s$ for B1, whereas $\xi_e \sim \xi_s$ for A2 and C.

What can possibly change the effective aspect ratio of rectangular samples? The

increase of the effective aspect ratio ξ_e of samples A1 and B2 may be due to the fact that only parts of the contacts are injecting current. The more surprising decrease of ξ_e for B1 could arise from doping from the contacts. This scenario would require the doping to penetrate some $\sim$ 500 nm per contact, 1-2 orders of magnitude larger than expected [116]. Another, more interesting possibility could be that the picture of an effective medium characterized by local conduction, on which the argument leading up to the semi-circle model [104] is based may not hold. Microscopically, this arise from large-scale density fluctuations, creating a mesh of intertwined electron and hole puddles with conducting states propagating along the interfaces [117]. The nonlocal transport mediated by such states may, under certain conditions, completely alter the conventional picture of local conduction. For this to happen, however, the typical spatial length scale of density fluctuations must be comparable to the sample size. However, because this scale was found to be just a few hundred nanometers in the scanning probe experiments [118], it seems rather unlikely that such a situation occurs in sample B1. Further studies are required to clarify the physical mechanism responsible for the observed behavior.

Leaving this puzzle aside, we note that the comparison of the data with the theoretical picture. [7] discussed in the previous Chapter shows overall qualitative agreement. This is remarkable, as the theoretical curves, describing the conductance dependence on density across several Landau levels are controlled solely by the effective aspect ratio ξ_e. This parameter depends on the sample geometry, but may take the same values for very different geometries. Most importantly, however, geometry-dependent variations in the two-terminal conductance of graphene samples do not mask the key differences in $g(V_{\mathrm{bg}})$ that allow single-layer and bilayer samples to be distinguished, as demonstrated experimentally in this work.

Chapter 4

Edge States and the Half-Integer Quantum Hall Effect

4.1 Abstract

We employ the framework of massless Dirac model [55] to analyze Landau level energy spectrum near zigzag and armchair edges, the two most common graphene edge types. We formulate the boundary conditions for the Dirac spinor and solve resulting 1d eigenvalue equations, finding that the number of conducting edge modes is odd for both zigzag and armchair edge types, which explains the half-integer QHE and its universality. We study the local density of states near the boundary, and suggest that the properties of the edge states, e.g. their dispersion, which is different for the two edge types, can be studied with the help of STM. Results presented in this Chapter are published in Refs. [11, 64].

4.2 Introduction and Outline

In this Chapter we analyze the edge states spectrum of a graphene sample in a magnetic field. We consider two common edge types, armchair and zigzag, illustrated in Fig. 1-2a, and solve the Dirac equation with boundary conditions appropriate for these two edge types. As we shall see below, the zigzag edge is peculiar: it supports

a band of states near zero energy which are very tightly localized at the boundary (in fact, these so called surface states occur even when the magnetic field is absent). The quantum Hall edge states near the Dirac point result from the mixing of the zeroth LL and the surface mode (this was first demonstrated numerically, see Ref. [8]). In the framework of the Dirac model, the surface mode is dispersionless and does not contribute to the transport. Thus the total number of conducting channels does not depend on the edge type, which explains the universality of the anomalous quantum Hall quantization.

The predictions of the Dirac model for the zigzag edge case are in agreement with the numerical studies [8], based on the tight-binding model. Interestingly, including next-nearest neighbor hopping into the model [8] gives rise to a dispersing surface mode. However, the surface states are counter-propagating, and, therefore, they inevitably localize due to the edge imperfections. QH edge states, on the contrary, are chiral, and therefore cannot localize. The surface mode localization restores the universal anomalous QHE.

The details of the edge states spectrum, such as their dispersion and the corresponding local densities of states are different for the armchair and zigzag boundaries. As we argue below, these differences can be investigated using STM spectroscopy.

We start with analyzing the edge states spectrum in Section 4.3; in Section 4.4 we consider the local density of states and demonstrate that the edge states properties, including their dispersion, can be studied using STM.

4.3 Edge states spectrum.

4.3.1 Armchair edge.

We start with considering the edge states near an armchair boundary. For our analysis below, it is convenient to choose the Landau gauge,

$$A_x = -By,\ A_y = 0. \tag{4.1}$$

Then the low-energy Hamiltonians (1.1) take the following form,

$$H_{K,K'} = i\frac{\varepsilon_0}{\sqrt{2}} \begin{bmatrix} 0 & \pm\partial_y + (y - y_0) \\ \pm\partial_y - (y - y_0) & 0 \end{bmatrix}, \tag{4.2}$$

where $\varepsilon_0 = \hbar v_0 (2eB/\hbar c)^{1/2}$ and $y_0 = -p_x$. Here y and p_x are measured in the units of the magnetic length $\ell_B = (\hbar c/eB)^{1/2}$ and $\hbar/\ell_B$. The spectrum of the Hamiltonian (4.2) is given by Eq.(1.17).

Eigenfunctions of the Hamiltonian (4.2) for the two valleys $K(K')$ are given by

$$u_{K,n} = A(1 - \delta_{n,0})\varphi_{n-1}(y - y_0),\ v_{K,n} = A\varphi_n(y - y_0), \tag{4.3}$$

$$u_{K',n} = A\varphi_n(y - y_0),\ v_{K',0} = A(1 - \delta_{n,0})\varphi_{n-1}(y - y_0), \tag{4.4}$$

where $\varphi_n(z)$ is the n-th eigenfunction of the magnetic oscillator, and A is normalization factor, which equals 1 for $n = 0$ and $\sqrt{2}$ for $n \neq 0$. Note that zeroth LL states in the valley $K(K')$ reside solely on $B(A)$ sublattices [1].

We now analyze how LL spectrum (1.17) is modified near the *armchair* edge. Let us start by considering graphene situated at $y < 0$ with an armchair edge parallel to the x axis (see Fig.1-2a).

Energy levels of the Dirac fermions near the edge are determined from the eigenvalue equation $E\psi = H\psi$, where $\psi = (u, v)$, H is given by Eq.(4.2), and we omitted K, K' indices for simplicity. To analyze this eigenvalue problem, it is convenient to exclude v components of the wave function, and to consider eigenvalue equations for u components:

$$\frac{1}{2}\left(-\partial_y^2 + (y - y_0)^2 + 1\right) u_K = \lambda u_K, \tag{4.5}$$

$$\frac{1}{2}\left(-\partial_y^2 + (y - y_0)^2 - 1\right) u_{K'} = \lambda u_{K'}, \tag{4.6}$$

$$\lambda = (E/\varepsilon_0)^2. \tag{4.7}$$

[1] This property is specific for the $n = 0$ LL, and it makes the splitting of the zeroth LL due to Coulomb interaction distinctly different from that of other LLs (see [48, 84]).

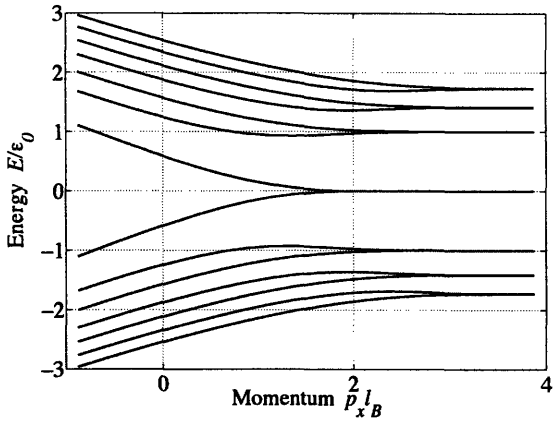

Figure 4-1: Graphene energy spectrum near the armchair boundary obtained from Dirac model, Eq.(1.1). The boundary condition, Eq.(4.8), lifts the K, K' degeneracy. The odd integer numbers of edge modes lead to the half-integer QHE.

The boundary conditions for Eqs.(4.5,4.6) can be obtained by assuming that the tight-binding model is valid up to the very last row near the boundary, and by setting the wave function amplitude to be zero at the boundary. Since the armchair edge has lattice sites of both A and B type (see Fig.1-2a), the wave function amplitude on both sublattices should vanish at the edge. In terms of the envelope functions $u_{K,K'}$, $v_{K,K'}$, taken at $y = 0$, this condition translates into

$$u_K = u_{K'}, \quad v_K = v_{K'}. \tag{4.8}$$

Thus we obtain a pair of differential equations (4.5),(4.6) on the half-axis $y < 0$, coupled at the boundary via Eq.(4.8). To analyze this problem, let us consider Eq.(4.5) for u_K on the negative half-axis $y < 0$, and Eq.(4.6) on the positive half-axis $y > 0$, and reformulate the boundary conditions accordingly. The first boundary condition in Eq.(4.8) then means that the wave function at $y = 0$ is continuous, and the second condition implies continuity of the derivative $\partial u/\partial y$ (this can be seen by expressing v components in terms of u components using Eqs.(4.2)). Thus we obtain a 1D Schrœdinger problem in the potential

$$V(y) = \frac{1}{2}(|y| + y_0)^2 - \frac{1}{2}\mathrm{sgn}(y), \tag{4.9}$$

defined on the entire y axis. We find the energy levels in the potential (4.9) numerically. Then, the energy levels of the Dirac fermions are related to the eigenenergies in the potential (4.9) via Eq.(4.7),

$$E(p_x) = \pm\varepsilon_0\sqrt{\lambda(y_0)}, \tag{4.10}$$

whereby the particle-hole symmetry is restored due to the two possible signs of $E(p_x)$. The energy spectrum (4.10) is illustrated in Fig.4-1. Notice that the double valley degeneracy of the Landau levels in the bulk is lifted at the boundary.

The particle-hole symmetric edge states spectrum in Fig. 4-1 instantly explains the half-integer Hall quantization in graphene. Indeed, for any electron density with integer filling factor ν in the bulk there is an odd number of the edge modes crossing the Fermi level, which means that the Hall conductivity is quantized at $\sigma_{xy} = 2(2n+1)e^2/h$, with the factor two introduced to account for the spin degeneracy.

Interestingly, for positive (negative) LLs one edge state first bends down (up), and then goes up (down), see Fig. 4-1. This can lead to a pair of counter-propagating edge states when the Fermi level is just below (above) a positive (negative) LL. Due to the fact that these counter-propagating states are spatially separated, scattering between them may be suppressed, and, in principle, they could contribute to the transport. This however have not been observed in the experiment, possibly because such counter-propagating states are supported only by the armchair edges, and in the experiment graphene boundaries have both zigzag and armchair parts.

4.3.2 Zigzag edge.

We now analyze the *zigzag* edge, which even at $B = 0$ hosts a a band of dispersionless zero-energy states bound to the edge [66]. We shall refer to these states as surface states, to distinguish them from the dispersing QH edge states. As we shall see below, surface states contribute to the splitting of $n = 0$ LL near the zigzag edge.

We consider graphene sheet in the half-plane $x > 0$, with its first row consisting

of B sublattice atoms (see Fig.1-2(a)). We choose a gauge

$$A_x = 0, \; A_y = Bx. \tag{4.11}$$

Then the Hamiltonian (1.1) transforms into

$$H_{K,K'} = \frac{\varepsilon_0}{\sqrt{2}} \begin{bmatrix} 0 & \partial_x \pm (x - x_0) \\ -\partial_x \pm (x - x_0) & 0 \end{bmatrix}, \tag{4.12}$$

where $x_0 = p_y$. Similarly to the armchair case, the spectrum can be found from the eigenvalue equation, $E\psi = H_{K,K'}\psi$, where $\psi = (u, v)$, and $H_{K,K'}$ is given by (4.12). This should be supplemented by the boundary condition, which for our zigzag edge is that the wave function vanishes at all A sites at $x = 0$. For that both envelope functions $u_K, u_{K'}$ have to vanish at the boundary,

$$u_K = 0, \quad u_{K'} = 0. \tag{4.13}$$

Excluding v components of the wave functions, we obtain two separate eigenvalue problems for the spectral parameter $\lambda = (E/\varepsilon_0)^2$,

$$\frac{1}{2}\left(-\partial_x^2 + (x - x_0)^2 + 1\right) u_K = \lambda u_K, \tag{4.14}$$

$$\frac{1}{2}\left(-\partial_x^2 + (x - x_0)^2 - 1\right) u_{K'} = \lambda u_{K'}, \tag{4.15}$$

where both u_K and $u_{K'}$ satisfy the hard wall boundary conditions (4.13). The amplitudes $v_{K,K'}$ on the B sublattice can be expressed via ampliudes $u_{K,K'}$ on the A sublattice and eigenenergy E,

$$v_K = (\varepsilon_0/\sqrt{2}E)\left(-\partial_x + (x - x_0)\right) u_K, \tag{4.16}$$

$$v_{K'} = (\varepsilon_0/\sqrt{2}E)\left(-\partial_x - (x - x_0)\right) u_{K'}. \tag{4.17}$$

The eigenvalue problems (4.14,4.15) with the hard-wall boundary conditions (4.13) are familiar from the study of the edge states in the conventional QHE (see Ref.[34]),

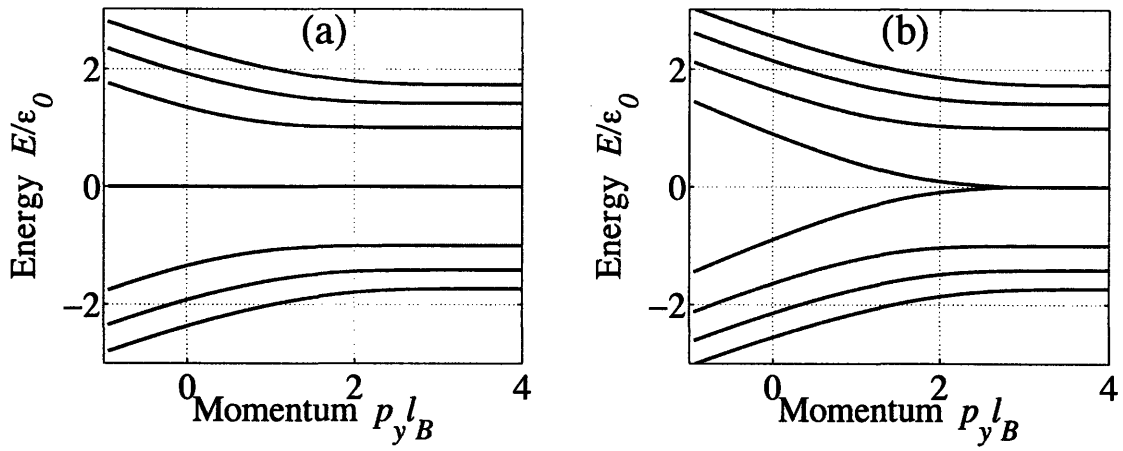

Figure 4-2: Graphene energy spectrum near the zigzag boundary obtained from Dirac model, Eq.(4.12), with boundary condition (4.13). (a) Spectrum for the K valley. The zeroth LL transforms into dispersionless surface mode near the edge. (b) Spectrum for the K' valley. The zeroth LL mixes with the surface mode at the edge, giving rise to two branches of dispersing QH edge states.

and their spectrum $\lambda(x_0)$ can be found numerically. The Dirac fermions energy levels, given by $E(p_y) = \pm\varepsilon_0\sqrt{\lambda(x_0)}$, are illustrated in Fig.4-2.

The behavior of $n \neq 0$ LLs is similar to the armchair case: there are two branches of the edge states, one for each valley, degenerate in the bulk, $x_0 \gg 1$, which split near the edge. The zeroth LL, however, coexists with the surface state, which makes its behavior rather peculiar and different for the two valleys.

In the K valley, which we discuss first, the zeroth LL states reside solely on the B sublattice, see Eq.(4.3), and therefore automatically satisfy the boundary condition $u_K = 0$. Thus there are K-valley zero-energy states for arbitrary values of x_0, of the form $\varphi_0(x - x_0) \propto e^{-(x-x_0)^2/2}$. Let us consider the states with x_0 far outside the graphene half-plane, $x_0 \ll -1$. Not too far from the boundary, such states can be approximated by an exponential

$$v_K(0 < x \lesssim |x_0|) \propto e^{-|x_0|x}, \quad u_K(x) = 0, \tag{4.18}$$

which is identical to the surface state wave function [66]. Thus the K-valley zeroth LL state in the bulk transforms into the surface mode at the edge. Since the surface mode

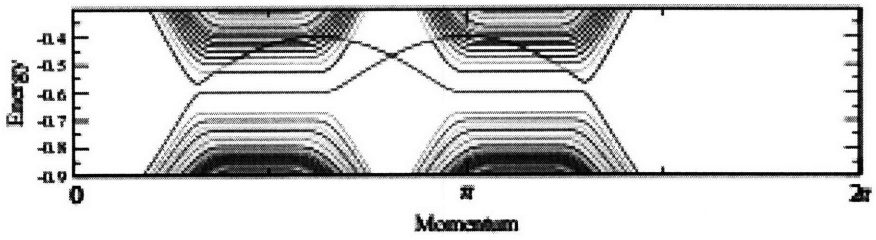

Figure 4-3: Landau levels spectrum of a graphene strip with zigzag edges, obtained numerically in the framework of the tight-binding model [8]. The interplay between the zeroth LL and surface state near the edges is illustrated. The zeroth LL in the K valley (left) transforms into a surface state near the right strip edge; the surface state traverses through the whole Brillouin zone, and mixes with the K' zeroth LL, generating a pair of quantum Hall edge states. The surface states, despite being dispersive owing to the next-nearest neighbor hopping introduced in the model, localize due to the coupling to strong edge disorder and do not contribute to the transport properties. Thus the half-integer quantization is preserved for the zigzag case. Adopted from Ref. [8]

is dispersionless, it does not contribute to the edge transport. The edge spectrum for the K valley is displayed in Fig.4-2a.

Now let us consider the splitting of the zeroth LL for the K' valley. For $x_0 \gg 1$, we approximate the ground state of the oscillator (4.15) with the hard-wall boundary condition as,

$$u_{K'}(x) = \psi_{x_0}(x) \approx \varphi_0(x - x_0) - \varphi_0(x + x_0). \tag{4.19}$$

The ground state energy $\lambda_0(x_0)$ is then approximated by,

$$\lambda_0(x_0) \approx \langle h \rangle, \tag{4.20}$$

where $h = \frac{1}{2}(-\partial_x^2 + (x - x_0)^2 - 1)$ is the effective Hamiltonian for $u_{K'}$ component, Eq.(4.15), and $\langle ... \rangle$ denotes averaging over the normalized wave function (4.19).

Evaluating $\langle h \rangle$ analytically for $x_0 \gg 1$ (in this limit the wave function (4.19) is normalized to unity with exponential accuracy), we obtain

$$\lambda_0(x_0) \approx x_0 \pi^{1/2} e^{-x_0^2}. \tag{4.21}$$

From the relation $E = \pm\varepsilon\sqrt{\lambda}$, we find the energies for the two branches of dispersing edge states,

$$E(x_0) \approx \pm(2x_0)^{1/2}\pi^{-1/4}e^{-x_0^2/2}\varepsilon_0. \tag{4.22}$$

Plugging this expression in Eq.(4.17), we obtain the wave function on B sublattice for these two branches,

$$v_{K'} = \pm x_0^{1/2}e^{-x_0 x}, \tag{4.23}$$

which is again the surface state wave function (compare to Eq.(4.18)). We therefore conclude that for the K' valley the zeroth Landau level and the surface state mix at the edge, giving rise to two dispersing edge modes. This is illustrated in Fig.4-2(b).

Interestingly, the A and B sites contribute equally to the splitting of the zeroth LL,

$$\int_{x>0} |u_{K'}|^2 \, dx = \int_{x>0} |v_{K'}|^2 \, dx. \tag{4.24}$$

This is somewhat counterintuitive, since this LL resides solely on the sublattice A in the bulk, while the surface mode resides solely on the sublattice B. This equal participation property can be understood as follows. The spinor states $(u_{K'}, \pm v_{K'})$ with $u_{K'}, v_{K'}$ given by Eqs. (4.19),(4.23) are eigenstates of the Dirac Hamiltonian with the boundary condition (4.13), with the energies $\pm E$. Thus these states are orthogonal, which implies that the integrals of $|u_{K'}|^2$ and $|v_{K'}|^2$ are equal. We further note that the integral of the square of the B component of our edge state wave function (4.23) over $x > 0$ indeed equals one, in agreement with our choice of the A component normalization (4.19).

To summarize, for the zigzag case the zeroth LL edge states are due to the mixing of the zeroth LL in one of the valleys and the surface state. The zeroth LL in the other valley transforms into the surface mode, which, being dispersionless, does not contribute to the transport. The bending of the non-zero LLs is similar to the armchair case. When an integer number of LLs is filled, there is a half-integer number of dispersing edge states at the Fermi level (see Fig. 4-2), leading to the anomalous QHE.

One may ask whether the surface mode remains non-dispersing and therefore non-

conducting when one goes beyond the Dirac model. This was explored in Ref. [8], where the numerical tight-binding model approach was used; the tight-binding model provides a more complete picture compared to the Dirac model which is applicable near K, K' points. The authors of Ref. [8] found that in the presence of the next-nearest neighbor hopping the surface mode becomes dispersing, as illustrated in Fig. 4-3, which shows the spectrum of a graphene strip in the whole Brillouin zone. However, at each strip edge the surface states are counter-propagating, and therefore would quickly localize due to the backscattering induced by the edge imperfections. That such imperfections are present is known from the STM studies of the graphite surface [73, 72]. In contrast, the QH edge states cannot localize due to their chirality. Thus we conclude that even when the surface mode acquires dispersion, the anomalous Hall quantization is not changed.

4.4 STM spectroscopy of edge states.

In this Section we briefly discuss how the edge states in graphene can be investigated using the STM technique [73, 72]. Due to the Landau level momentum-position duality relation, $p_y = (\hbar/\ell_B^2)x_0$, the edge state momentum dispersion shown in Figs. 4-1, 4-2 translates into the excitation energy dependence on the distance from the edge. The characteristic scale for the latter is set by the magnetic length ℓ_B, which for typical fields is about 50-80 times greater than the spatial resolution of STM instruments on graphite surface. This makes the STM technique particularly convenient for the edge states studies.

A link between the edge states dispersion and the position-dependent tunneling spectroscopy can be established as follows. We shall use the solutions for the edge state wave function given above to calculate the local density of state (LDOS) near the zigzag edge (other edge types can be dealt with similarly). For each of the graphene sublattices LDOS is given by

$$\rho_A(E, x) = \sum_\alpha |u_\alpha(x)|^2 \delta(E - E_\alpha), \tag{4.25}$$

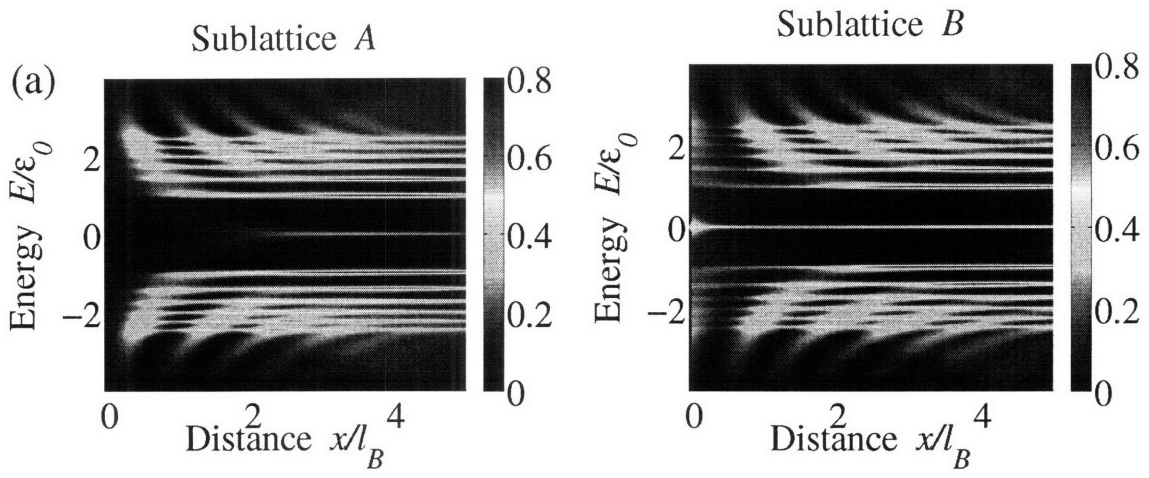

Figure 4-4: STM spectrum of graphene near the zigzag edge for sublattice A (a) and B (b). x is the distance to the edge. Due to the momentum-position duality, analysis of the STM spectrum allows extraction of the edge states dispersion.

$$\rho_B(E,x) = \sum_\alpha |v_\alpha(x)|^2 \delta(E - E_\alpha), \tag{4.26}$$

where x is the distance from the edge, and α denotes the set of eigenstates of the K and K' Hamiltonians (4.12) with the hard-wall boundary condition (4.13).

Using the eigenfunctions $u_\alpha(x), v_\alpha(x)$ and the energies E_α found from Eqs. (4.14),(4.16) as discussed above, we obtain LDOS for the A and B sublattices which is displayed in Fig. 4-4. We see that the position-independent Landau level bands, dominating LDOS far from the edge, bend away from $\varepsilon = 0$ near the edge. This bending mimics the edge states momentum dispersion shown in Fig. 4-2. Note, however, that LDOS is nonzero only for $x > 0$, whereas the edge states momentum p_y can be both positive and negative. The spatial width of the bending bands is determined by the width of the eigenfunctions $u_\alpha(x), v_\alpha(x)$, which is of the magnetic length scale.

The behavior of the LDOS at $x \to 0$ is very different for the two sublattices: it remains finite for the sublattice B, and vanishes for the sublattice A. This agrees with the boundary condition (4.13), which requires A amplitudes to vanish at the boundary.

The peculiar nature of the zeroth LL splitting, discussed in the previous section, also manifests itself in the STM spectrum. While the position of A-sublattice LDOS

maximum closest to the edge (see Fig. 4-4(a)) mimics the dispersion of the zeroth LL edge states, the B-sublattice LDOS (Fig. 4-4(b)) has a local maximum right at the edge, $x = 0$. This behavior can be understood in the limit of low energies as follows. Limit of the low energies corresponds to the large distance from the edge, $x \gg 1$, which allows to make us of the approximate expressions (4.19),(4.23) obtained in the previous section. The edge state amplitude on the sublattice A (4.19) has a maximum at $x \approx x_0 = p_y \ell_B^2/\hbar$, while the amplitude on the sublattice B (4.23), which explains the LDOS behavior. The difference of the A and B spectra suggests that in the experiment the zeroth edge states dispersion should be extracted from the A-sublattice spectrum. The edge states dispersion for the non-zero LLs can be extracted using either A or B spectra, as each of them mimic the momentum dependence of the edge state energies, see Figs. 4-2,4-4.

For the armchair case, the LDOS is equal for the two sublattices, as follows from the symmetry of the armchair boundary condition (4.8) with respect to the two sublattices. The spectrum of either sublattice mimics the dispersion of the armchair edge states, Fig. 4-1.

Chapter 5

Quantum Hall Effect in Locally Gated Graphene Devices

5.1 Abstract

We study two-terminal conductance of locally gated graphene devices, p-n and p-n-p junctions. In p-n junctions, the edge states mixing at the p-n interface and propagation across the interface give rise to conductance quantization, which is integer in the unipolar regime, and fractional and integer in the bipolar regime. Our results explain the recently observed conductance quantization [9] discussed in Section 1.4. We propose several possible mechanisms leading to mixing at the p-n interface, including dephasing by localized states, electron thermalization and self-averaging. We suggest that shot noise measurements can be used to distinguish between different transport regimes.

In p-n-p junctions, in addition to the analogues of the bipolar and unipolar regimes, a new intermediate partial equilibration regime is realized, where modes circulating in the n region can transfer electrons between opposite edges of the sample. We find quantized conductance values in all three regimes, which are in agreement with the experiment [10]. Finally, we explore robustness of the QHE in p-n-p junctions with respect to disorder, finding that the sensitivity of various plateaus strongly depends on the filling factors as well as sample geometry. Some of the results presented

in this Section are published in Refs. [101, 10].

5.2 Introduction

So far we have discussed quantum Hall transport in graphene samples with uniform density of carriers controlled by a global back gate. In this Chapter we consider transport properties of locally gated quantum Hall graphene devices, *p-n* and *p-n-p* junctions, where the density is spatially non-uniform. Experimentally, the problem of fabricating graphene *p-n* and *p-n-p* junctions attracted large interest since the very discovery of graphene for two reasons. First, junctions provide the basis for possible device applications; second, graphene junctions were predicted to exhibit interesting transport effects reflecting the Dirac character of excitations, such as Klein tunneling through *p-n* interfaces and Veselago lensing in *p-n-p* junctions [119] (both effects occur in the absence of the magnetic field). However, due to high sensitivity to disorder, neither effect was observed in the experiments with the first graphene junctions [57, 9, 10]. Somewhat surprisingly, the most interesting transport effect in the first graphene junctions was observed in a magnetic field, when Williams et al. [9] and Ozyilmaz et al. [10] found that two-terminal conductance of junctions is quantized at fractional and integer values.

The experimental results of Williams et al. [9] are illustrated in Fig. 5-1. Fig. 5-1b shows two-terminal conductance g of a *p-n* junction (Fig. 5-1a) as a function of top (V_t) and back gate voltages (V_b), which are used to independently control filling factors ν_1 and ν_2 in the p and n regions. To understand the rhombi pattern of the conductance in Fig. 5-1b we consider g as a function of the top gate voltage fixing the filling factor in the non-gated region. Fig. 5-1c shows $g(V_t)$ at $\nu_1 = 6$, and (d) corresponds to $\nu_2 = 2$. Interestingly, g exhibits quantized plateaus with values $1, 3/2, 2, 6 \ldots e^2/h$.

In this Chapter, we explain the observed conductance quantization. We employ the edge states framework to study the two-terminal transport,finding that the conductance is quantized when incompressible QHE states are formed in the p and n

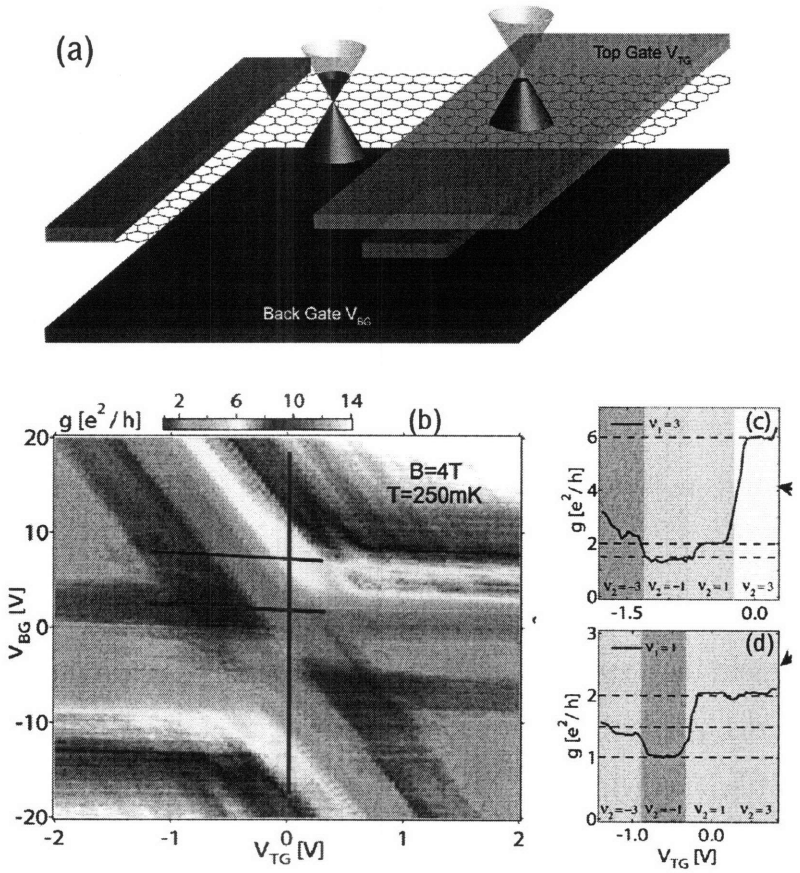

Figure 5-1: Conductance of a graphene p-n junction in the QHE regime, from Ref. [9]. (a) schematic of the device, with a local top gate used to create a p-n junction. (b) Conductance map as a function of top and bottom gate voltages. (c), (d) conductance as a function of top gate voltage at fixed filling factors (6 and 2, respectively) in the non-gated region. Conductance exhibits a series of quantized plateaus with fractional and integer values.

parts of the device. The edge states transport in p-n junctions is quite different in the unipolar and bipolar cases, which leads to different quantized conductance values : in the unipolar regime, the edge states cannot backscatter, and therefore the quantized sequence of uniform graphene, $\pm 2, \pm 6 \ldots e^2/h$, is reproduced. In the bipolar regime, the edge states can mix at the p-n interface, which effectively leads to edge states scattering between the opposite sample edges. Such scattering is usually non-universal and should lead, by analogy with quantum dots, to mesoscopic conductance fluctuations. However, as will be explained below, there are several effects which wash out the mesoscopic fluctuations, leading to the fractional and integer conductance quantization in the bipolar regime.

In p-n-p junctions, the situation is slightly more complicated [10]: there are three possible edge states structures depending on the densities in the p and n parts of the device. These three cases give rise to a sequence of quantized conductance values which is different from that in p-n junctions. The quantized values that we find using the edge states picture mostly agree with the experimental observations [9, 10].

It turns out that the agreement between the simple edge states theory [101, 10] and the experiment in the p-n-p junctions [10] is not perfect. While most conductance plateaus predicted by the theory are observed experimentally, others are either absent or their values deviate significantly from the theoretical ones [10]. We attribute this behavior to backscattering of the edge states in the locally gated n region. Such backscattering can result from the density inhomogeneities induced by the local gate, which is only several tens of nanometers away from the sample, or from the coupling of the edge states to localized states in the gated region. To analyze the backscattering effects, it is convenient to switch to the bulk conductivity framework. Solving the conduction problem in an inhomogeneous conductor which models the p-n-p junction, we find that the robustness of the quantization strongly depends on the filling factors in the p and n regions, and on the geometry of the central n region.

Our work complements previous studies of gated quantum Hall devices with backscattering [120]. Theory developed there employed Landauer transport approach and considered backscattering due to the coupling of the edge states to the localized

states. Our phenomenological approach treats unipolar regime, considered previously [120] and bipolar regime, which is specific to graphene [101, 9, 10], on equal footing. For the unipolar regime our conclusions are similar to those of Ref.[120].

The rest of this Chapter is organized as follows. In Section 5.3 we discuss the edge states structure in p-n junctions and show that, when mesoscopic conductance fluctuations are suppressed, the conductance is quantized. In Section 5.4 we demonstrate that there are several different mechanisms suppressing the mesoscopic fluctuations; we suggest that shot noise measurements can be used to distinguish between those mechanisms. In Section 5.5 we consider the edge states in p-n-p junctions and the corresponding quantized values of conductance. Finally, in Section 5.6 we employ bulk conductivity approach to describe the sensitivity of the quantization to the edge states backscattering in the central region.

5.3 Conductance quantization in p-n junctions

We start with analyzing the edge states structure in p-n junctions; there are two regimes, bipolar, when densities in the two part of the device are of the opposite signs, and unipolar, when the densities are of the same sign. As we saw in the previous Chapter, an incompressible quantum Hall state with a filling factor ν has $|\nu|$ edge channels, propagating in the opposite direction for $\nu > 0$ and $\nu < 0$ [8, 11]. For the bipolar case, assuming QHE at densities $\nu_1 > 0$ and $\nu_2 < 0$ on either side of the boundary, this gives $|\nu_1|$ and $|\nu_2|$ edge modes circulating in opposite directions that merge to form a multi-mode edge states at the p-n interface, see Fig. 5-2a. These modes supply particles from both p and n reservoirs to the p-n interface. After propagating together along the interface these particles arrive at the sample boundary where they are ejected into the edge modes which split up and return to the reservoirs.

In the unipolar case, edge modes in both regions circulate in the same direction. As a result, some modes are coupled to both reservoirs, while the others are connected to only one of the reservoirs. This is illustrated in Fig. 5-2b.

The observed conductance quantization in the bipolar case can be readily ex-

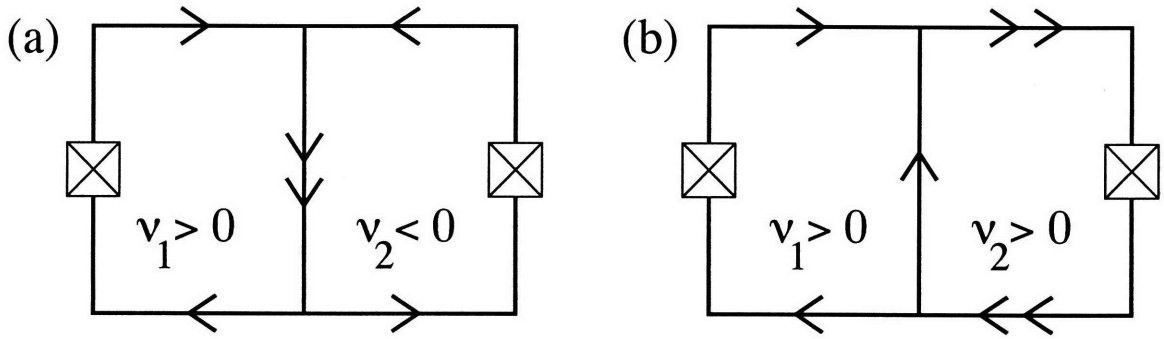

Figure 5-2: Schematic of QHE edge states for (a) bipolar regime of pn junction, and (b) unipolar regime of nn and pp junctions. In case (a) the edge states counter-circulate in the n and p regions, bringing to the pn interface electrons and holes from different reservoirs. Mode mixing at the interface leads to the two-terminal conductance (5.1). In case (b), since the edge states circulate in the same direction without mixing at the interface, conductance is determined by the modes permeating the whole system, $g = \min(|\nu_1|, |\nu_2|)$.

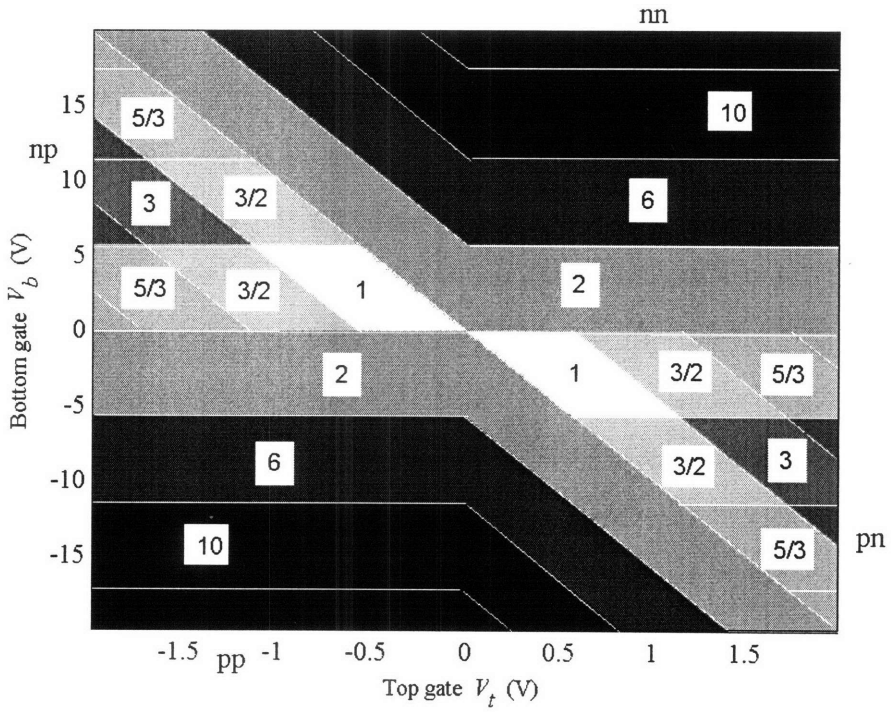

Figure 5-3: Two-terminal conductance vs. gate voltage, given by Eq. 5.2 in the unipolar case ($\nu_{1,2}$ of equal sign), and by Eq. 5.1 in the bipolar case $\nu_1 > 0$, $\nu_2 < 0$. The boundaries of QHE regions are specified by $\nu_{1,2} = 0, \pm 4, \pm 8...$, with the gate voltage dependence of $\nu_{1,2}$ given by Eq. 5.3. Parameters used: distances to the top and back gates $h = 30\,\text{nm}$, $d = 300\,\text{nm}$, magnetic length $\ell_B = 10\,\text{nm}$, dielectric constant $\kappa = 3$.

plained by assuming full mixing of the modes propagating along the p-n interface, such that for each particle the probability to be ejected into any of the $N = |\nu_1| + |\nu_2|$ modes equals $p_N = 1/N$ irrespective of its origin. The two-terminal conductance is then obtained by multiplying p_N by the numbers of the modes connected to the reservoirs, giving

$$g_{\rm pn} = \frac{|\nu_1||\nu_2|}{|\nu_1| + |\nu_2|} = 1, \frac{3}{2}, 3, \frac{5}{3}..., \tag{5.1}$$

$\nu_{1,2} = \pm 2, \pm 6, \pm 10....$ This agrees with the observed quantized values [9].

The transport in the unipolar regime is very different. With backscattering suppressed by the QHE, the conductance across the boundary is solely due to those edge modes that permeate the entire system, making contact with both reservoirs. This gives the observed nonclassical conductance values

$$g_{\rm nn} = g_{\rm pp} = \min(|\nu_1|, |\nu_2|) = 2, 6, 10..., \tag{5.2}$$

where $\nu_{1,2} = \pm 2, \pm 6, \pm 10...$, in agreement with the known results for quantized conductance of constrictions between different QHE states [121, 122, 123].

The conductance values given by Eqns. 5.2 and 5.1 occur in a particular pattern [9] that can be described as follows (see Fig.5-3). Electron density in graphene induced by the back gate is $n_1 = (\kappa/4\pi e)V_{\rm b}/d$, where d is the distance to the gate, $V_{\rm b}$ is voltage on it, and κ is dielectric constant. Similarly, in the region gated from both the top and the bottom, we have $n_2 = (\kappa/4\pi e)(V_{\rm b}/d + V_{\rm t}/h)$, where h and $V_{\rm t}$ are the distance to the top gate and voltage on it. For the Landau level filling factors $\nu_{1,2} = (hc/eB)n_{1,2}$ we find

$$\nu_1 = (\ell_B^2\kappa/2e)V_{\rm b}/d, \quad \nu_2 = (\ell_B^2\kappa/2e)(V_{\rm b}/d + V_{\rm t}/h), \tag{5.3}$$

with $\ell_B = \sqrt{\hbar c/eB}$ the magnetic length. The values $V_{\rm b}$, $V_{\rm t}$ corresponding to integer QHE states are inside parallelograms with the boundaries approximately given by $\nu_{1,2} = 0, \pm 4, \pm 8...$, as appropriate for the four-fold degenerate graphene Landau levels [4, 30]. The resulting conductance pattern, shown in Fig.5-3 for realistic parameter

values, strikingly resembles the experimental results illustrated in Fig. 5-1b.

5.4 Mixing mechanisms and shot noise.

In this section we address the nature of the edge states mixing at the p-n interface in the bipolar regime, which we have assumed in the previous Section to explain the observed conductance quantization. For that, an analogy of the edge states system to a chaotic quantum dot proves very helpful. In this analogy the QHE states at the sample boundary play the role of perfect lead channels of chaotic quantum dots [105, 124], bringing charge to the p-n interface and carrying it away into the reservoirs. The p-n interface plays the role of the quantum dot itself, with the intermode scattering corresponding to the scattering inside the dot. An important difference is that several physical mechanisms causing conductance fluctuations in chaotic dots are absent in our case, leading to quantization of two-terminal conductance not known for the dots. In particular, the effective lead channels are quantized much more perfectly than in the dots, owing to the backscattering suppression in the QHE transport. In addition, the quantum-mechanical interference effects which lead to sample-specific conductance fluctuations, can be suppressed in our case due to self-averaging, as well as dephasing and electron-electron scattering. Other effects that can affect the edge state transport at the p-n interface are intermode relaxation and coupling to electronic localized states in the QHE bulk, causing dephasing in a manner similar to the voltage probe model [125]. While these regimes yields equivalent results for the conductance, they will manifest themselves differently in other transport characteristics, in particular, in electron shot noise [126], which can be used for detailed characterization of transport mechanisms.

How is conductance in Eq. 5.1 affected by interference effects? Random matrix theory (RMT) predicts [105, 124] ensemble-averaged conductance $\bar{g} = n_1 n_2/(n_1+n_2+1-2/\beta)$, where $n_{1,2}$ is the open channel number, and $\beta = 1, 2, 4$ for the three random matrix universality classes. In our QHE case, with the channel numbers $n_{1,2} = |\nu_{1,2}|$ and $\beta = 2$, RMT predicts $\bar{g}$ identical to Eq. 5.1. Similarly, semiclassical description

of transport chaotic cavities [126], where mixing is due to the dynamics in the cavity, yields conductance values close to the classical result for two conductors connected in series.

To understand the origin of chiral QHE mode mixing at the pn interface we studied electron density distribution for the gate geometry used in Ref. [9]. Numerical solution of Laplace problem for the electrostatic potential in between the gates revealed that the pn density step is about 40 nm wide, a few times larger than the magnetic length at $B = 10\,\mathrm{T}$. Comparison to the known results [127] for intertwining compressible and incompressible QHE regions then suggests the presence at the pn interface of QHE modes having opposite chiralities, $N + m$ propagating in one direction and m in the other direction, $m > 0$. In that, $N = |\nu_1| + |\nu_2|$ modes are coupled to reservoirs, while $2m$ counter-propagating modes are confined to the interface region. Such counter-propagating modes, if present, will facilitate inter-channel scattering leading to dynamical mixing.

In the fully coherent regime conductance would exhibit sample-specific fluctuations, UCF. The magnitude of UCF predicted for chaotic transport (see Ref.[128]) in our case depends on the channel numbers as follows:

$$\mathrm{var}(g) = \frac{\nu_1^2\nu_2^2}{(|\nu_1| + |\nu_2|)^2((|\nu_1| + |\nu_2|)^2 - 1)}. \tag{5.4}$$

Applied to the observed plateaus with $(\nu_1, \nu_2) = (2, -2), (2, -6), (6, -2)$, Eq. (5.4) indicates that these plateaus would not have been discernible in a system with fully developed UCF. We therefore conclude that the observed quantization of g depends on some mechanism that suppresses UCF. For example, the suppression could easily be understood if Thouless energy for the states at the pn interface was small compared to $k_\mathrm{B}T$. The reduced UCF would then result from averaging over the $k_\mathrm{B}T$ energy interval. However, the plateaus in [9] remain unchanged when temperature is reduced from 4K to 250 mK, making such a scenario unlikely.

The UCF suppression may signal a fundamental departure of chiral QHE dynamics from that of the earlier studied systems. However, at this point we cannot exclude

other, more mundane explanations. In particular, time-dependent fluctuations of system parameters can supercede mesoscopic fluctuations, turning the observed time-averaged quantities into ensemble-averaged quantities. This could arise naturally due to fluctuating electric field at the pn interface induced by voltage noise on the gates. Another, more interesting explanation could be that UCF suppression indicates presence of dephasing due to the coupling of the chiral modes to the localized states in the bulk.

Current partition due to mode mixing at the *pn* interface will manifest itself in the finite shot noise intensity. To evaluate noise, we note that mixing of the reservoir distributions, no matter of what origin, results in particle energy distribution of the form

$$n(\varepsilon) = \frac{|\nu_1|}{N} n_1(\varepsilon) + \frac{|\nu_2|}{N} n_2(\varepsilon) \tag{5.5}$$

which at small $k_B T$ is a double step. In analogy with diffusive systems [129], and chaotic cavities [126, 130], this distribution serves as a Kogan-Shulman-like extraneous source of current fluctuations,

$$J = \int n(\varepsilon)(1 - n(\varepsilon)) d\varepsilon = \frac{|\nu_1||\nu_2|}{N^2} |V_{sd}|. \tag{5.6}$$

We relate the noise source J to the fluctuations of the two-terminal current by noting that, since fluctuating current of intensity J is injected into each open channel, the current fluctuations flowing into the n and p regions will be $J_1 = |\nu_1| J$ and $J_2 = |\nu_2| J$. Converting these fluctuations into voltage fluctuations and adding the contributions of the n and p regions, we find the voltage fluctuations induced between the reservoirs:

$$\delta V^2 = \frac{J_1}{|\nu_1|^2} + \frac{J_2}{|\nu_2|^2} = \left(\frac{1}{|\nu_1|} + \frac{1}{|\nu_2|} \right) J = \frac{|V_{sd}|}{N}. \tag{5.7}$$

Current noise can now be obtained as $S = g^2 \delta V^2$, where g is the conductance (5.1). It is convenient to characterize noise by the Fano factor $F = S/I$, describing noise

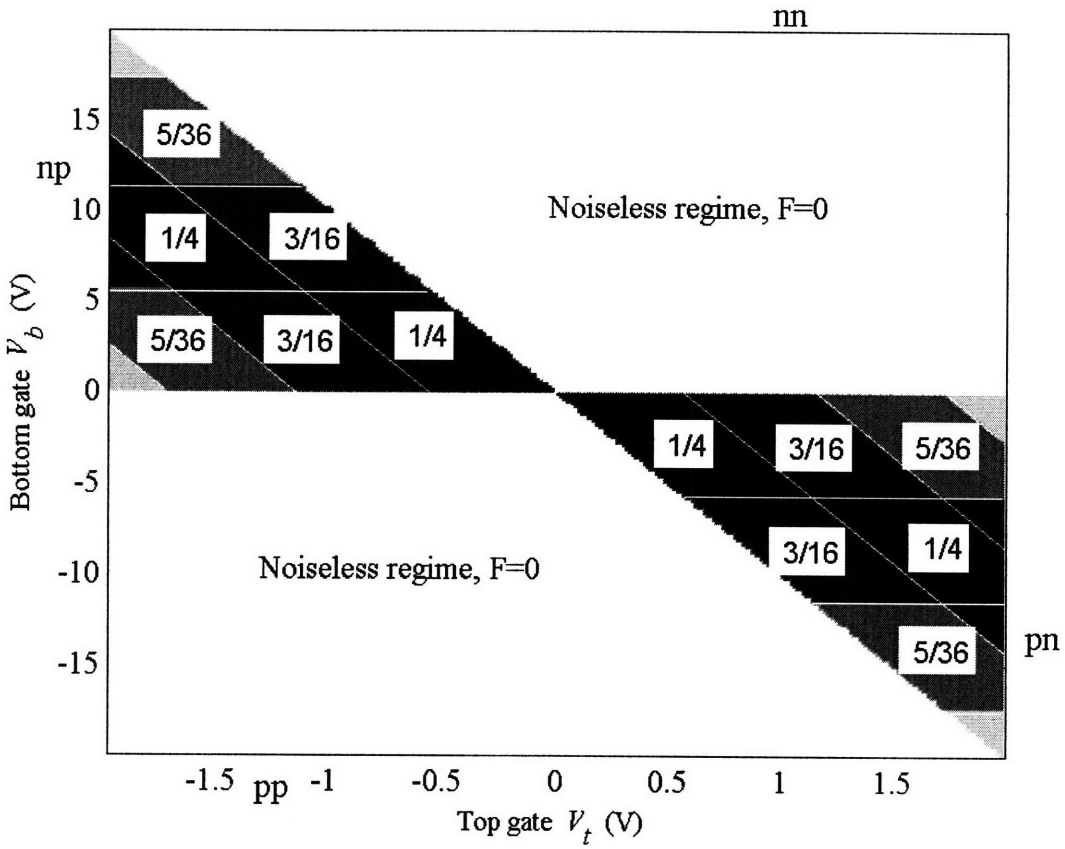

Figure 5-4: Shot noise Fano factor, Eq. (5.8), plotted *vs.* gate voltages for the same parameter values as in Fig.5-3. Noise is zero in the unipolar regime (*pp* or *nn*) due the absence of current partition at the junction interface, but finite in the bipolar regime due to edge mode mixing at the pn interface.

suppression relative to Poisson noise. We find

$$F = \frac{|\nu_1||\nu_2|}{(|\nu_1| + |\nu_2|)^2} = \frac{1}{4}, \frac{3}{16}, \frac{5}{36}..., \tag{5.8}$$

where $\nu_{1,2} = 2, 6, 10....$ The result (5.8) is identical in form to the shot noise Fano factors predicted for chaotic cavities [126], which were tested and confirmed experimentally [130]. The Fano factors in Eq. (5.8) are to be contrasted with the Fano factor $F \approx 0.29$ in the absence of magnetic field [131].

Another regime for noise is possible if electrons, while traveling along the p-n interface, have enough time to transfer energy to each other via inelastic processes. This will occur if $\tau_{el} \ll L/v$, where τ_{el} is the characteristic electron energy relaxation time, v is drift velocity and L is the p-n interface length. (A similar regime was analyzed for diffusive [129] and chaotic [130] transport.) In this case, the electron energy distribution is characterized by an effective temperature T_{eff} which is determined by the balance of the energy supplied from reservoirs and electron thermal energy flowing out:

$$\frac{1}{2}\frac{|\nu_1||\nu_2|}{|\nu_1| + |\nu_2|} V_{sd}^2 = \zeta(2)(|\nu_1| + |\nu_2|) k_{\text{B}}^2 T_{\text{eff}}^2 \tag{5.9}$$

The extraneous fluctuations, Eq. (5.6), evaluated for the Fermi distribution with $T = T_{\text{eff}}$, give $J = k_{\text{B}} T_{\text{eff}}$. Repeating the reasoning that has led to Eq. (5.8) we find the noise intensity $S = g k_{\text{B}} T_{\text{eff}}$. This expression resembles the Nyquist formula, except for the factor of two missing because the fluctuations (5.6) occur only in the p-n region but not in the leads. Since $T_{\text{eff}} \propto V_{sd}$, this noise is linear in V_{sd}. Similar to the $T = 0$ shot noise, we characterized it by Fano factor $\tilde{F} = (3F)^{1/2}/\pi$, with F given by Eq.5.8.

We finally note that noise can be used to test which of the UCF suppression mechanisms discussed above, self-averaging or dephasing, occur in experiment [9]. For coherent transport noise exhibits mesoscopic fluctuations similar to UCF which can be analyzed within RMT framework. In the absence of time reversal symmetry,

RMT yields ensemble-averaged Fano factor

$$\bar{F} = \frac{|\nu_1||\nu_2|}{(|\nu_1| + |\nu_2| + 1)(|\nu_1| + |\nu_2| - 1)} \tag{5.10}$$

(see Eq. 11 in Ref. [128]). For $\nu_{1,2} = 2, 4, 6...$ this gives $\bar{F} = 4/15, 12/63, 36/143....$ These values, expected when transport is coherent but self-averaged, are different from Eq. (5.8) obtained from incoherent mixing model.

5.5 Conductance quantization in *p-n-p* junctions

In this Section we consider edge states in *p-n-p* junctions, demonstrating that there are three different edge states transport regimes, depending on the relation between the filling factors in the locally gated central region (LGR) (ν) and ungated parts, referred to as graphene leads (GLs) (ν'). The edge states mixing gives rise to the conductance quantization, similarly to the *p-n* junctions considered above. We compare the theoretical conductance pattern to the experimental observations [10], finding a good qualitative agreement, but also some important differences, which are studied in the subsequent Section.

From the point of view of the edge states structure, there are three possibilities. The simplest possibility is when the polarity of GLs and LGR is the same (either *p-p'-p* or *n-n'-n*), and the LGR density is lower that the GLs density: $|\nu'| < |\nu|$. In this case, as shown in Fig. 5-5a, the number of QH edge modes is larger in the GLs than in the LGR. THe modes existing only in the GLs are fully reflected at the GLs-LGR interfaces, while those present in both regions exhibit full transmission, giving rise to the net conductance

$$g = |\nu'|\frac{e^2}{h} = 2, 6, 10, \ldots \frac{e^2}{h} \quad (|\nu'| < |\nu| \text{ and } \nu\nu' > 0). \tag{5.11}$$

This regime is similar to the unipolar regime in *p-n* junctions.

A more interesting situation occurs when the LGR density is higher than the GLs density, with the LGR and GLs polarities still the same. In this case the number

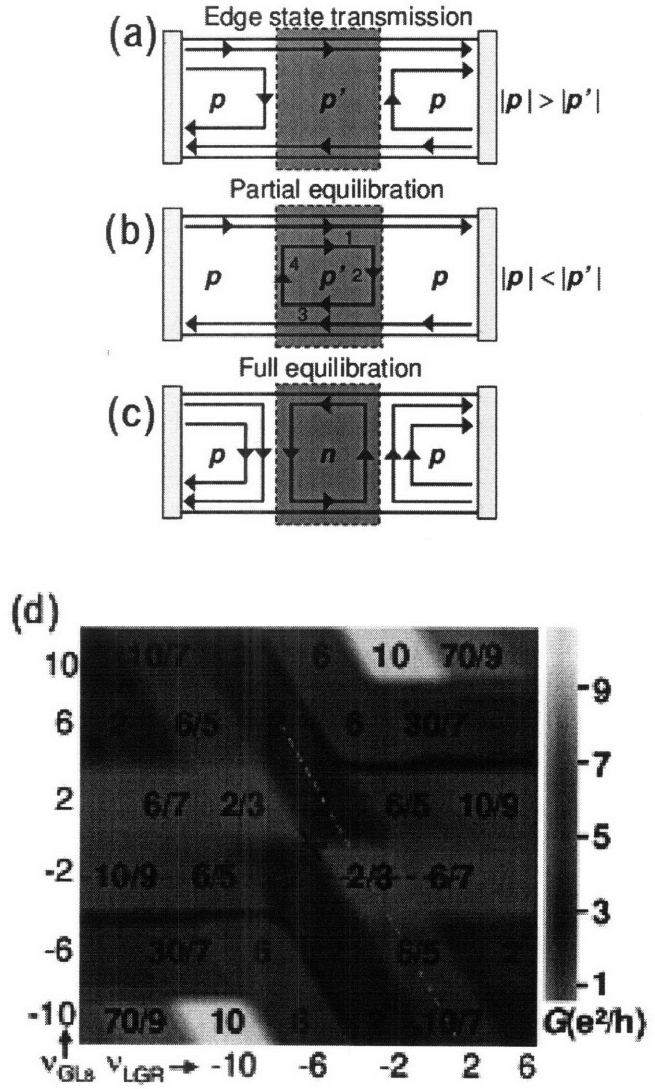

Figure 5-5: Edge states (a) to (c) and the quantized conductance values in a p-n-p junction (d). (a) to (c): different edge states diagrams representing possible equilibration processes taking place at different charge densities in the GLs and LGR. The purple region indicates the LGR, yellow boxes indicate contact electrodes. (d) Simulated color map of the theoretical conductance plateaus expected from the mechanisms shown in (a)-(c) for different filling factors in the GLs and LGR. The numbers in the rhombi indicate the conductance at the plateau.

of the edge states is smaller in the GLs than in the LGR (see Fig. 5-5b). Crucially, the states circulating in LGR can produce partial equilibration among the different channels, because they couple modes with different electrochemical potentials. To analyze this regime, we suppose that current I is injected from the left lead, while no current is injected from the right lead. Then the conservation of current yields $I + I_4 = I_1$, $I_2 = I_3$ (the LGR edges are labeled by 1, 2, 3,4 as shown in Fig. 5-5b). Assuming that the current at the upper and lower LGR edges is partitioned equally among available edge modes, we obtain the relations for the current flowing out of these edges: $I_2 = rI_1$, $I_4 = rI_3$, $(r = 1 - |\nu'|/|\nu|)$. Solving these equations for $I_{1...4}$, we determine the current flowing in the drain lead as $I_{out} = I_1 - I_2$ and find the net conductance

$$g = \frac{|\nu'||\nu|}{2|\nu'| - |\nu|}\frac{e^2}{h} = \frac{6}{5}, \frac{10}{9}, \frac{30}{7}, \ldots \frac{e^2}{h} \quad (|\nu'| \geq |\nu| \text{ and } \nu\nu' > 0), \tag{5.12}$$

where $\nu, \nu' = \pm 2, \pm 6, \ldots$. We emphasize that this *partial equilibration* regime can only occur in the presence of two *n-n'* or *p-p'* interfaces and would not occur in a single *n-n'* or *p-p'* junction [9, 101].

The last, but most unique case is when the GLs and LGR have opposite carrier polarity. In this case, the edge states counter-circulate in the p and n areas, propagating together along the *p-n* interface (see Fig. 5-5c). Such propagation, leading to mixing among edge states, results in full equilibration at the *p-n* interfaces: $I_1 = rI_2$, $I_3 = rI_4$, $(r = |\nu'|/(|\nu| + |\nu'|))$. Combining this with the current conservation, in this case written as $I + I_1 = I_4$, $I_2 = I_3$, we find the currents and obtain the conductance

$$g = \frac{|\nu'||\nu|}{2|\nu'| + |\nu|}\frac{e^2}{h} = \frac{2}{3}, \frac{6}{5}, \frac{6}{7}, \ldots \frac{e^2}{h} \quad (\nu\nu' < 0), \tag{5.13}$$

where $\nu, \nu' = \pm 2, \pm 6, \ldots$. The net conductance in this *full equilibration regime* is described by three quantum resistors in series.

The summary of all possible conductance values for the three regimes discussed above is shown as a color map in Fig. 5-5d. This color map corresponds to Fig. 5-2 for *p-n* junction case, the only difference being that in Fig. 5-5d the axes show filling

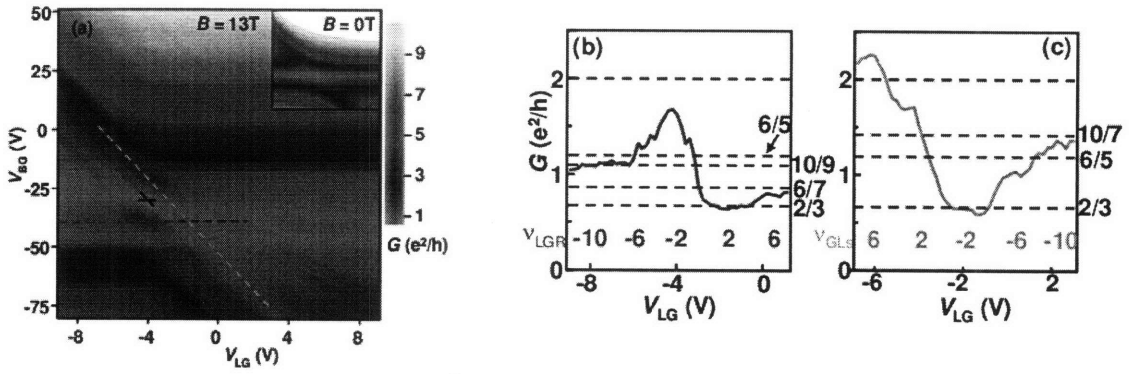

Figure 5-6: (a) Color map of conductance as a function of top and back gate voltages at magnetic field $B = 13T$ and $T = 4.2\,\mathrm{K}$. The black cross indicates the location of filling factor zero in LGR and GLs. Inset: Conductance at zero B in the same range of gate voltages and the same color map as the main figure (white denotes $g > 10.5e^2/h$). (b) $g(V_t)$ extracted from (a), red trace, showing fractional values of the conductance. Numbers on the right indicate expected fractions for the various filling factors (red numbers indicate the filling factor, ν', in LGR). (c) $g(V_t)$ (projection of orange trace from (a) onto V_t axis). Orange numbers indicate filling factor, ν, in the GLs. From Ref. [10].

factors in the GLs and LGR, and not the top and back gate voltages, as in Fig. 5-2. Comparing the two color maps, we see that the sequence of quantized values is very different in the p-n-p and p-n junctions.

How do our predictions, Eqs. (5.11),(5.12),(5.13), compare to the experiment? Fig. 5-6a shows the experimentally observed conductance g as a function of local and back gate voltages. Qualitatively, the structure of the experimental pattern qualitatively resembles the theoretical one, see Fig. 5-5d. For a quantitative analysis, we choose two cuts extracted from Fig. 5-6(a), showing conductance for fixed $\nu = -2$ (Fig. 5-6(b)) and $\nu' = -2$ (Fig. 5-6(c)). We notice reasonably good plateaus at $g = (2/3)e^2/h$, $g = (10/9)e^2/h$ as well as other fractions discussed above, with the only exception of a considerably more poor plateau with $g = 2e^2/h$ (see below). Of particular interest is the non-monotonic conductance behavior in Fig. 5-6(b) for $\nu' = 2, -2, -6, -10$ (with $\nu = -2$), which reflects the the full equilibration $\rightarrow$ edge states transmission $\rightarrow$ partial equilibration sequence. This is in contrast with the

monotonic behavior of g in Fig. 5-6(c) for $\nu = -2 \to 2 \to 6$ (with $\nu' = 2$), where only the full equilibration and full transmission regimes are expected.

To sum up, we have studied three possible edge states transport regimes which take place at different carrier densities in the GLs and LGR. Assuming edge states equilibration, we obtained a sequence of fractional and integer quantized conductance values, most of which are observed in the experiment [10]. However, at $\nu = \nu' = \pm 2$ instead of the theoretically predicted plateau with $g = 2e^2/h$ experiment finds a broadened peak with the maximal value of about $1.7e^2/h$. In the next Section we present a possible explanation of this discrepancy.

5.6 Stability of the QHE in *p-n-p* junctions

In this Section, in an attempt to explain the absence of the $\nu = \nu' = \pm 2$ plateaus in the experiment, we study the sensitivity of the conductance quantization to the edge states backscattering in the locally gated region. The enhanced backscattering in the central region may be caused by density inhomogeneities introduced by the top gate, which is just 30 nm away from the sample. We analyze the effect of backscattering in the bulk conduction framework, finding that the robustness of quantization at different filling factors strongly depends on the LGR geometry. For the experimental geometry [10] our model predicts that the plateaus with $\nu = \nu'$ should be most sensitive to the backscattering, thus explaining the observations [10].

We employ bulk conductivity approach and model the *p-n-p* junction as a conductor with a spatially inhomogeneous conductivity tensor, as illustrated in Fig.5-7. Left and right regions correspond to ungated regions in the experiment and are assumed to be incompressible, with quantized Hall conductivity $\sigma'_{xy} = \nu' e^2/h$ and vanishing diagonal conductivity. The gated central region is dissipative, with $\sigma_{xx} \neq 0$, which accounts for the edge states backscattering. Below we reduce the conduction problem in the inhomogeneous conductor to that in a homogeneous conductor [103] with a modified conductivity tensor, which allows us to find the two-terminal conductance of *p-n-p* device as a function of σ_{xx} and the central region's aspect ratio $\ell = L/W$

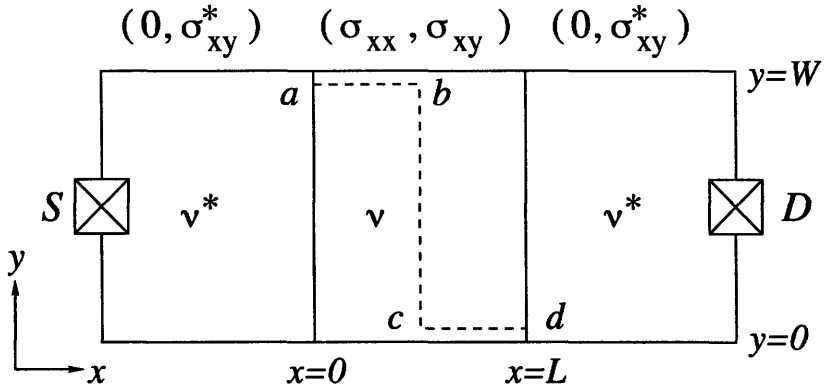

Figure 5-7: The schematic of our model: left and right regions are incompressible with the Hall conductivity σ'_{xy}, the central region of width W and length L is compressible and has a conductivity tensor $(\sigma_{xx}, \sigma_{xy})$.

(see Fig.5-7).

In the limit of vanishing σ_{xx} our model predicts quantized values which coincide with the results of the edge states model described in the previous Section. The sensitivity of the quantized conductance values to non-zero σ_{xx} strongly depends on the aspect ratio $\ell = L/W$: (i) for small aspect ratio $\ell \ll 1$, the quantization at equal densities in p and n regions is most robust, while the quantization at nonequal densities is extremely sensitive to non-zero σ_{xx}; (ii) for aspect ratio $\ell \gtrsim 1$, the quantization at large densities in the central region is more robust than the quantization at small densities in the central region; (iii) for a square central region, $\ell = 1$, we evaluate the conductance analytically using the duality argument [108] and find the quantization at $\nu \neq \nu'$ is especially robust, because, the first order in σ_{xx} correction to the quantized conductance value vanishes.

Below we also analyze the conductance as a function of carrier density in the central region, which can be directly compared to the experimental data [10]. To model the filling factor dependence of the conductivity tensor $(\sigma_{xx}, \sigma_{xy})$, we employ the semicircle law [109, 104], describing the transition between neighboring integer QHE plateuas. The semicircle law is known to be sufficiently general and it was recently noticed to hold in graphene [110, 48].

The conductivity tensor $(\sigma_{xx}, \sigma_{xy})$ obtained from the semicircle model was defined in Chapter 2, see Eqs. (2.7),(2.8),(2.9), and below we will use those expressions. For

simplicity sake, throughout this Chapter we shall assume that the LL broadening parameter λ is the same for all LL. Then it follows from Eqs. (2.7),(2.8),(2.9) that the value of σ_{xy} at the center of the k-th plateau is given by

$$\sigma_{xy} = \nu_k e^2/h \tag{5.14}$$

The current distribution in the central region can be found from the continuity equation for the current density $\mathbf{j} = (j_x, j_y)$ and zero-curl condition for the in-plane electric field component $\mathbf{E} = (E_x, E_y)$,

$$\nabla \cdot \mathbf{j} = 0, \quad \nabla \times \mathbf{E} = 0, \tag{5.15}$$

supplemented by proper boundary conditions and a relation between the current density and the electric field,

$$\mathbf{j} = \sigma_{xx}\mathbf{E} - \sigma_{xy}\hat{\mathbf{z}} \times \mathbf{E}, \tag{5.16}$$

where $\hat{\mathbf{z}}$ is a unit vector normal to the xy plane. Following Ref. [132], we introduce a stream function ψ via

$$\mathbf{j} = \hat{\mathbf{z}} \times \nabla\psi, \tag{5.17}$$

which ensures the current continuity requirement (5.15). From Eqs.(5.15),(5.16) it follows that the stream function in the central region satisfies the Laplace equation,

$$\nabla^2\psi = 0. \tag{5.18}$$

Boundary conditions for the stream function at the interfaces $x = 0, L$ can be obtained from the requirement that the current component j_x perperdicular to the interface and the electric field component E_y parallel to the interface are continuous. This gives a relation between j_x and j_y current components in the central region,

$$\frac{j_x}{j_y} = \frac{\rho_{xx}}{\rho_{xy} - \rho'_{xy}}, \quad x = 0, L, \tag{5.19}$$

where ρ_{xx}, ρ_{xy} are the longitudinal and Hall resistivities in the central region, and ρ'_{xy} is the Hall resistivity in the left and right regions. At the edges of the sample $y = 0, W$ the boundary condition is that no current flows out of the sample,

$$j_y = 0, \quad y = 0, W. \tag{5.20}$$

To make further progress, we notice that the limit of vanishing ρ'_{xy} corresponds to a perfectly conducting p regions, which then play a role of ideal contacts. Therefore, the problem of current flow in the n region, Eqs.(5.17),(5.18),(5.19),(5.20) is formally equivalent to that in a rectangle with spatially uniform resistivity tensor $(\tilde{\rho}_{xx}, \tilde{\rho}_{xy}) = (\rho_{xx}, \rho_{xy} - \rho'_{xy})$ and contacts situated at $x = 0, L$. Such problem was solved in Refs. [106, 103]. This observation allows us to express the conductance of the p-n-p junction in terms of the resistance of a homogeneous rectangle with dimensions (L, W).

Without loss of generality, below we assume the filling factor ν' to be positive, which corresponds to the edge states circulating clockwise. The source-drain bias V_{SD} can then be evaluated between any point at the upper edge of the left region and any point at the lower edge of the right region. Because there is no voltage drop along the edges of the incompressible regions, V_{SD} equals the voltage drop between the corners of the central regions, a and d (see Fig. 5-7). Therefore V_{SD} can be written in terms of current components integrated along the contour $abcd$, illustrated in Fig. 5-7,

$$V_{SD} = \int_{ab,cd} \rho_{xx} j_x dx - \int_{cb} (\rho_{xx} j_y - \rho_{xy} j_x) dy. \tag{5.21}$$

Writing ρ_{xy} in the above expression as $\tilde{\rho}_{xy} + \rho'_{xy}$, we express V_{SD} via the source-drain bias in the equivalent conduction problem for a homogeneous rectangle,

$$V_{SD} = \tilde{V}_{SD} + \int_{cb} \rho'_{xy} j_x dy = \tilde{V}_{SD} + \rho'_{xy} I, \tag{5.22}$$

where I is the total current. From this we can obtain the relation between the conductance $G = I/V_{SD}$ of the p-n-p junction and resistance $\tilde{R} = \tilde{V}_{SD}/I$ of the

homogeneous rectangle,

$$G = \frac{1}{\rho'_{xy} + \tilde{R}}. \tag{5.23}$$

When the central region is incompressible, which corresponds to no backscattering, $\rho_{xy} = h/\nu e^2$ is quantized and $\tilde{R} = |\rho_{xy} - \rho'_{xy}|$, independent of the aspect ratio ℓ. Therefore the conductance is quantized,

$$G = \frac{1}{\rho'_{xy} + |\rho_{xy} - \rho_{xy}|}. \tag{5.24}$$

Using relations $\rho_{xy} = h/\nu e^2$, $\rho'_{xy} = h/\nu' e^2$, we express G in terms of filling factors,

$$G_0 = \frac{\nu\nu'}{\nu' + |\nu' - \nu|}\frac{e^2}{h}. \tag{5.25}$$

This is in agreement with the predictions of the edge states model discussed in the previous Section.

When $\rho_{xx} \neq 0$, the quantization is destroyed, and below we study the sensitivity of the quantization to ρ_{xx} as a function of filling factors ν, ν' and aspect ratio ℓ. An analytical result for arbitrary ρ_{xx} can be obtained for a square central region, $\ell = 1$. In this case the resistance $\tilde{R}_{sq} = \sqrt{\rho_{xx}^2 + (\rho_{xy} - \rho'_{xy})^2}$, as follows from the duality argument [108]. Therefore, the p-n-p conductance is given by,

$$G_{sq} = \frac{1}{\rho'_{xy} + \sqrt{\rho_{xx}^2 + (\rho_{xy} - \rho'_{xy})^2}}. \tag{5.26}$$

An interesting implication of this results is that the linear term in the expansion of G_{sq} in powers of ρ_{xx} vanishes, and therefore the conductance quantization it this case should be especially robust, at least at weak backscattering.

For an arbitrary aspect ratio, $\tilde{R}$ cannot be found analytically, and we evaluate it numerically using the approach of Ref. [103]. The detailed description of our numerical procedure can be found in Chapter 2. We start with evaluating conductance G as a function of σ_{xx} at the centers of the plateaus, where the filling factor ν is quantized and the Hall conductivity is given by $\sigma_{xy} = \nu e^2/h$, see Eq.(5.14). The

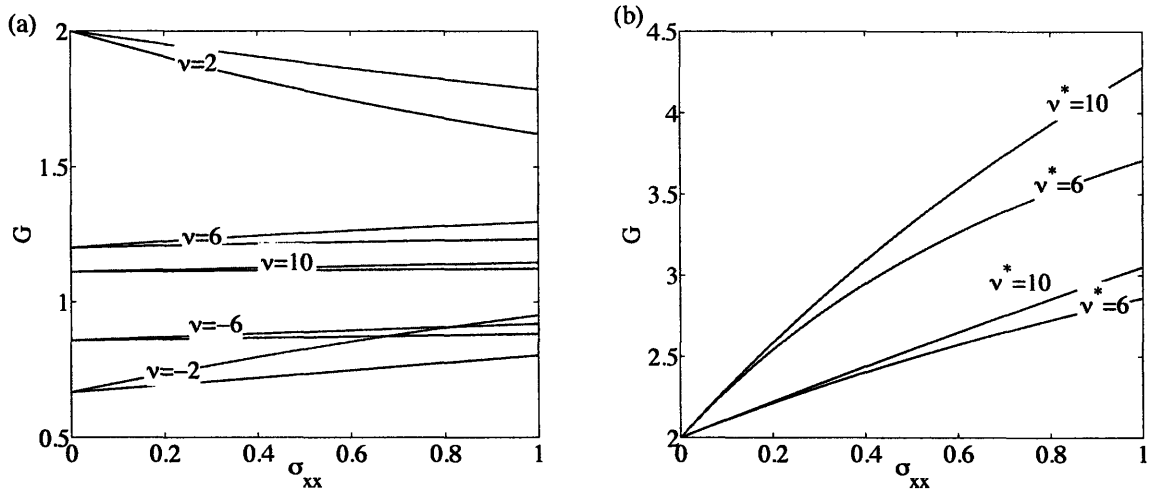

Figure 5-8: Conductance at the centers of various plateaus as a function of the longitudinal conductivity σ_{xx} in the central region, (a) plateaus with $\rho'_{xy} > \rho_{xy}$ and (b) plateaus with $\rho'_{xy} < \rho_{xy}$. Red curves correspond to central region's aspect ratio $\ell = 0.25$, blue curves to $\ell = 0.5$.

resulting behavior for several plateaus (characterized by two numbers ν, ν' from the sequence (1.13)) and aspect ratios $\ell = 0.25, 0.5$ is illustrated in Fig.5-8. In Fig.5-8a we show the conductance for filling factors $\nu' = 2$, $\nu = -6, -2, 2, 6, 10$, which corresponds to the case $\rho'_{xy} \geq \rho_{xy}$, and in Fig.5-8b we show the conductance for filling factors $\nu = 2$, $\nu' = 6, 10, 14$, corresponding to the case $\rho'_{xy} < \rho_{xy}$.

Examining Fig.5-8 we find that the behavior of the conductance $G(\sigma_{xx})$ is quite different in the two cases, $\nu' = \nu = -2$ and $\nu' \neq \nu$. For $\nu' = \nu = 2$ the conductance is less sensitive to σ_{xx} for the smaller aspect ratio $\ell = 0.25$. For $\nu' \neq \nu$ the situation is opposite: the conductance is more sensitive to σ_{xx} for the smaller aspect ratio $\ell = 0.25$. Another interesting feature is that for large $\nu \gg 1$ the conductance is almost insensitive to σ_{xx}, and remains very close to its value at $\sigma_{xx} = 0$ even at $\sigma_{xx} \sim e^2/h$.

Combining the numerical procedure with the semicircle law (2.9),(2.7),(2.8) we now analyze the conductance as a function of the filling factor in the central region. The function $G(\nu)$ for the aspect ratio $\ell = 5/7$ from the experiment [10], and $\nu' = -2$ is pictured in Fig.5-9. The two curves in Fig.5-9 correspond to narrow LLs (solid curve, parameter $\lambda = 1.7$) and broadened LLs (dashed curve, $\lambda = 0.5$). For the narrow

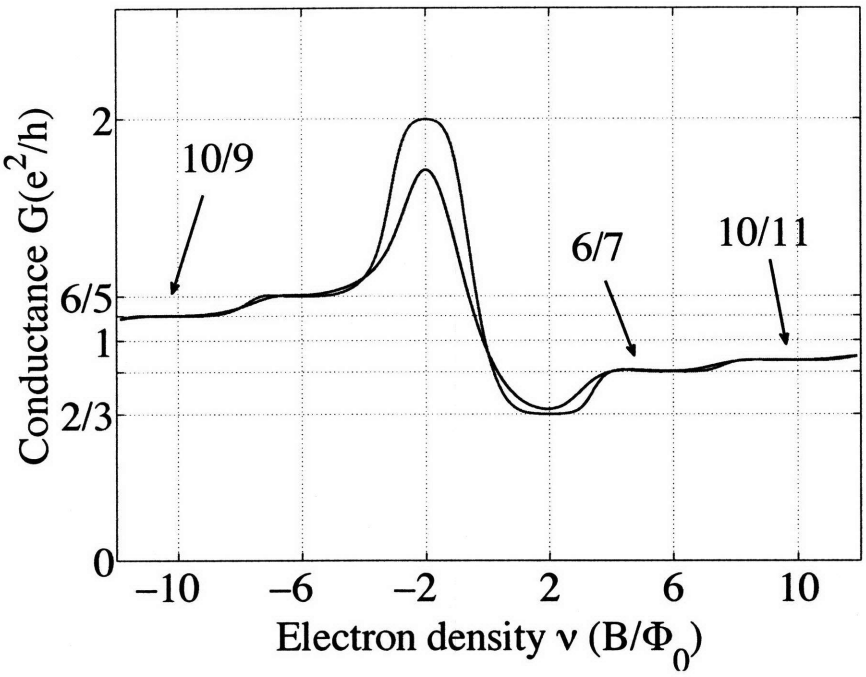

Figure 5-9: Conductance G as a function of the filling factor ν in the central region. The filling factor in the left and right regions is $\nu' = -2$, the aspect ratio $L/W = 5/7$ is taken from the experiment [10]. For narrow LLs ($\lambda = 1.7$, top curve) all the plateaus are well developed, while for broadened LLs ($\lambda = 0.5$, bottom curve) the plateau with $\nu = -2$ is destroyed, while all the others are still preserved. The bottom curve models experimental data displayed of Ref. [10] displayed in Fig. 5-6b.

LLs, all the plateaus are well developed. For the broadened LLs, the quantization is destroyed only at $\nu = \nu' = -2$, while all the other plateaus persist despite the relatively large value of $\sigma_{xx} \approx 0.5e^2/h$ at the plateaus centers.

Fig.5-9 can be directly compared to the experiment. The dashed curve in Fig.5-9 models the experimental data shown from Ref. [10] shown in Fig. 5-6b. We chose the value of the parameter $\lambda = 0.5$ in such a way that the peak value of the conductance at $\nu = -2$ matches the experimentally observed value $G \approx 1.7$ (see Fig. 5-6b). This allows us to achieve a good qualitative agreement with the experiment [10] in the whole range of filling factors $-12 < \nu < 12$.

To gain further insight into the sensitivity of various plateaus to σ_{xx}, we now analyze the conductance at the center of each plateau in the limit of small $\sigma_{xx} \ll e^2/h$, corresponding to weak backscattering. We shall be interested in the first in σ_{xx}

correction to the quantized values given by Eq.(5.25) at the center of the plateau. This correction, δG, can be expressed via the first-order term in the expansion of $\tilde{R}$,

$$\delta G = -G_0^2 \delta \tilde{R}. \tag{5.27}$$

The behavior of $\delta\tilde{R}$ is different in the two cases, (i) $\nu = \nu'$, and (ii) $\nu \neq \nu'$. In the first case, due to the fact that at the center of the plateau $\sigma_{xy} = \sigma'_{xy} = \nu e^2/h$, effective Hall resistivity $\tilde{\rho}_{xy} = O(\sigma_{xx}^2)$ (to see this, one needs to express $\tilde{\rho}_{xy}$ in terms of σ_{xy}, σ_{xx}). Therefore, the current flow in the central region is that for a conductor with zero Hall angle and resistivity $\rho_{xx} \approx \sigma_{xx}/\sigma_{xy}^2$, which gives $\delta\tilde{R} = \ell\sigma_{xx}/\sigma_{xy}^2$, This allows us to obtain δG,

$$\delta G = -\sigma_{xx}\ell. \tag{5.28}$$

The second case, $\nu \neq \nu'$, corresponds to the limit of large effective Hall angles, $|\tilde{\theta}| = |\arctan(\tilde{\rho_{xy}}/\tilde{\rho}_{xx})| \approx \pi/2$. The behavior of $\delta\tilde{R}$ for large Hall angles was analyzed in Ref. [106],

$$\delta\tilde{R} = -\rho_{xx}\kappa(\ell), \tag{5.29}$$

where $\kappa(\ell)$ is defined as follows,

$$\kappa(\ell) = \ln\frac{1-k}{2\sqrt{k}}, \quad \ell = \frac{K(\sqrt{1-k^2})}{2K(k)}, \tag{5.30}$$

with K being the complete elliptic integral of the first kind. Combining Eqs.(5.29) and (5.27), we obtain the correction δG,

$$\delta G = -\left(\frac{\nu'}{\nu' + |\nu - \nu'|}\right)^2 \sigma_{xx}\kappa(\ell). \tag{5.31}$$

The dependence $\kappa(\ell)$ is illustrated in Fig. 5-10. Notice that $\kappa(\ell)$ vanishes for the square case, $\ell = 1$, in agreement with the analytic formula (5.26).

The limiting behavior of the function $\kappa(\ell)$ at $\ell \gg 1$ is approximately linear, $\kappa(\ell) \approx$ $\ell \gg 1$, which is due to the fact that a homogeneous current flow sets in the central region with large aspect ratio. In the opposite limit of small $\ell \ll 1$ the function $\kappa(\ell)$

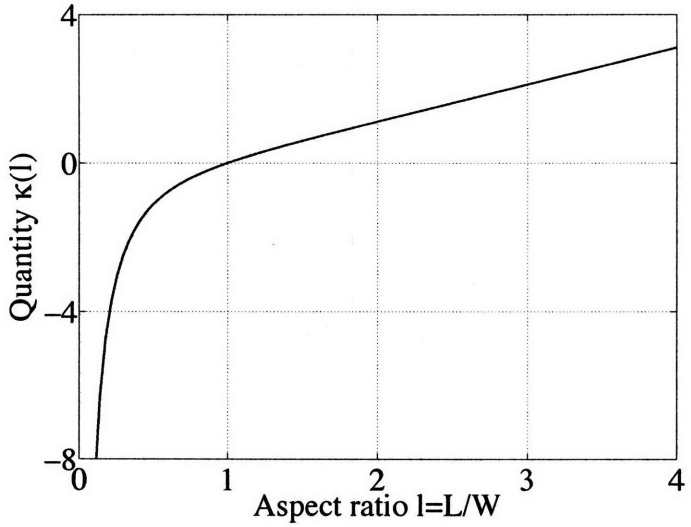

Figure 5-10: Quantity κ, defined in Eq. (5.30), as a function of the aspect ratio ℓ.

has a divergence, which can be qualitatively understood as follows. Since the central region is very narrow, it becomes well conducting at relatively small $\sigma_{xx} \gtrsim \sigma_{xx}^{\ell} = \ell e^2/h$ and essentially behaves as an ohmic contact. Therefore for $\sigma_{xx} \gtrsim \sigma_{xx}^{\ell}$ the resistance of the *p-n-p* junction can be obtained as a series resistance of the left and right regions, which gives the conductance $G_s = \nu' e^2/2h$. Then the derivative of the conductance with respect to σ_{xx} can be estimated as $dG/d\sigma_{xx} \sim (G_s - G_0)/\sigma_{xx}^{\ell} \propto 1/\ell$. Since $\kappa \propto dG/d\sigma_{xx}$, we obtain $\kappa \propto 1/\ell$, which explains the divergence of κ at $\ell \to 0$.

Examining Eqs.(5.28),(5.31), we find that at small aspect ratios $\ell \ll 1$ the quantization for $\nu = \nu'$ is very robust, while the quantization at $\nu \neq \nu'$ is destroyed even by weak backscattering. For aspect ratios $\ell \gtrsim 1$ the quantization is most robust at large filling factors in the central region, $\nu \gg \nu'$.

In conclusion, in this Section we have found that the relative sensitivity of various plateaus in *p-n-p* junctions with respect to the edge states backscattering in the LGR strongly depends on the LGR geometry. For narrow LGR ($\ell \ll 1$), plateaus with $\nu = \nu'$ are most robust, while for wide LGR ($\ell \gtrsim 1$) plateaus with $\nu \gg \nu'$ are most robust. Our results agree the experimental observations of Ozyilmaz et al. [10] where samples with $\ell \sim 1$ were studied. Samples with narrow LGR, $\ell < 0.5$, were studied recently by J. Lau group, see Ref. [100]. Lau et al. found that in such samples the plateau at $G = 2e^2/h$ is recovered, as we would expect from our model. However,

the observation of Lau et al. is most likely due to the fact that in their experiment the LGR was less disordered than LGR in the experiment of Ozyilmaz et al. [10] (the two experiments used different procedures to fabricate top gates). Because of that, we cannot attribute the observation of the $G = 2e^2/h$ plateau to the LGR geometry effect. Thus we conclude that although predictions of our model agree with both experiments, a more detailed experimental study of the quantization in samples with different LGR geometries is required.

Chapter 6

Spin and Charge Transport near the Dirac Point

6.1 Abstract

In this Chapter we exlplore spin and charge transport phenomena at the quantum Hall edge of $\nu = 0$ state. First, we compare valley- and spin-polarized $\nu = 0$ states, finding that, while the former is insulating, the latter features a pair of spin-filtered counter-circulating edge states, which give rise to a metallic behavior of transport coefficients.

The spin-filtered edge state lead to a rich variety of spin transport effects, including quantized spin Hall effect, spin filtering and injection, and detection of spin-polarized currents. The estimated Zeeman gap, enhanced by exchange, of a few hundred Kelvin, makes $\nu = 0$ state in graphene an attractive candidate for spintronics.

Furthermore, by introducing and solving a model, where transport along the edge is accompanied by weak transport through the bulk, we study density dependence of the transport coefficients for the spin-polarized $\nu = 0$ state. We find, in agreement with the experiment (see Section 1.4), that the Hall conductivity exhibits a smeared plateau, while the longitudinal resistivity exhibits a broadened peak with a maximal value of a few h/e^2; depending on the model parameters, the Hall resistivity may either smoothly change sign at $\nu = 0$, or have a smeared plateau. Most of the results

presented in this Chapter are published in Refs. [11, 6, 64].

6.2 Introduction and outline

As we have already discussed above in Section 1.4, QHE state at the Dirac point exhibits unusual behavior of transport coefficients [5, 6]. While the Hall conductivity has a plateau at the Dirac point, similarly to other QHE states, the Hall resistivity often does not exhibit any features. Furthermore, the longitudinal resistivity at the Dirac point has a metallic temperature dependence, and at low temperatures saturates at a value of the order of a few h/e^2.

Theoretically, several possible $\nu = 0$ QH state have been proposed [11, 81, 93, 82, 5]. Refs. [11, 81] considered a QHFM scenario, where the $\nu = 0$ state is spin-polarized, in Refs. [5, 80] valley-polarized QHFM state was suggested. An alternative scenario of dynamically generated Dirac fermion mass was proposed in Ref. [?], while Ref. [82] put forward a possibility of a spontaneous sublattice symmetry breaking due to the interaction with substrate.

The primary goal of this Section is to theoretically compare transport properties of different $\nu = 0$ states. We argue that the spin-polarized state [11, 81] has a peculiar edge state structure, which makes its transport characteristics distinctly different from those of the valley-polarized state [5],and states proposed in Refs. [93, 82].

More specifically, the spin-polarized state features a pair of edge states of opposite chirality and opposite spin polarization [11]. The unique property of these *spin-filtered* edge states is that they carry spin-up and spin-down excitations in the opposite directions, and therefore backscattering cannot happen without a spin flip. In graphene, as we discuss below, spin flips are strongly suppressed due to the smallness of the spin-orbit interaction. Thus the spin-filtered edge states do not localize down to low temperatures, in contrast to the counter-propagating surface states discussed in Chapter 4. Conducting spin-filtered edge states lead to a metallic behavior of the resistivity for the spin-polarized $\nu = 0$ state.

Below we provide a general argument, showing that gapless edge states can only

occur in the spin-polarized $\nu = 0$ state, and are absent in other proposed states. Therefore, spin-unpolarized states [5, 93, 82] are gapped both in the bulk and at the edge, and thus exhibit an insulating behavior, with an activated temperature dependence of resistivity. Therefore, experimentally observed metallic behavior [6] (see Section 1.4) suggests that the $\nu = 0$ state is spin-polarized.

Can edge states explain the intriguing behavior of the Hall resistivity observed in the experiment? To answer this question, we consider a model, where transport at opposite edges is shunted by a weakly conducting bulk. Remarkably, we find, in agreement with the experiment, that for a wide range of model parameters ρ_{xy} smoothly changes sign at the Dirac point; for other parameter values it exhibits a smeared feature at $\nu = 0$. Our analysis lends further support to the picture of spin-polarized $\nu = 0$ state.

Furthermore, we address spin transport properties of the $\nu = 0$ state. The spin-filtered character of the edge states gives rise to a quantum spin Hall effect; furthermore, these edge states can be employed to realize and explore interesting new spin transport phenomena, such as spin filtering and spin injection, whereas the spin Hall effect provides a natural tool for the detection of spin current.

The rest of this Chapter is organized as follows. In Section 6.3 we demonstrate that the gapless edge states at $\nu = 0$ are specific to the spin-polarized $\nu = 0$ state; if the $\nu = 0$ state is valley-polarized, the edge states are inevitably gapped. We point out that the difference in the edge states leads to very different transport properties of the two states . In Section 6.4 we study the spin transport properties of the spin filtered edge states, suggesting that they may be used for spin filtering and spin-polarized current detection. Section 6.5 is a detailed study of the charge transport properties near $\nu = 0$. We start it with the estimate of the mean free path at the edge, finding it to be comparable to the typical sample size. To explore the density dependence of the transport coefficients in detail, we introduce and solve a model where edge and bulk transports are coupled. Our model is capable of reproducing all the qualitative features observed in the experiment [6].

6.3 Spin polarization *versus* valley polarization

In this Section we compare the edge states spectra for the spin-polarized and valley-polarized states at $\nu = 0$. We find that while the spin-polarized state supports a pair of counterpropagating gapless edge modes, for the valley-polarized state the valley mixing at the edge opens up a gap in the edge states spectrum. Therefore, the two states should exhibit very different transport properties, most notably, at low temperatures the spin-polarized state should remain metallic, while the valley-polarized states is insulating. In the high-filed experiments [5, 6] σ_{xx} is of the order of e^2/h down to 4 K, which suggests that the spin-polarized state is realized in the experiment.

We start with the spin-polarized case. The Zeeman splitting modifies the edge states spectrum illustrated in Fig. 4-1 by shifting spin-up LLs upwards, and spin-down LLs downwards. The spin-split spectrum shown in Fig. 6-1 features a pair of counter-propagating edge states in the vicinity of the zero energy. Remarkably, these edge states carry opposite spins, which makes them fundamentally different, for example, from the counter-propagating surface states discussed in Chapter 4.

Fig. 6-1 illustrates the single-particle spectrum of excitations. However, taking the Coulomb interaction into account does not change the main feature of the spectrum, the presence of the gapless modes propagating in both directions along the edge [98]. There is also an important modification: the edge states become interacting and form a Luttinger liquid. This, in principle, should affect their transport properties compared to the non-interacting model. However, at relatively high temperatures the Luttinger-type effects, such as backscattering amplitude enhancement are rather small and can be safely neglected. Therefore, below we shall treat the edge modes as non-interacting; this assumption, although it inevitably breaks down at very low temperatures, should provide a qualitatively correct picture of transport at the experimental temperatures ranging between 4 K and hundreds of Kelvin [5, 6].

Can gapless edge states occur in a valley-polarized $\nu = 0$ state? To answer this question, we notice that for gapless edge states to occur, at least one of the zeroth

Landau sub-levels should be empty in the bulk, giving rise to a hole-like edge mode. (This is the case for the spin-polarized case, see Fig. 6-1: two spin-up Landau sub-levels are empty in the bulk, and they split near the edge into one hole and one electron mode.) To explore the valley-polarized case, we recall the valley structure of the edge modes found in Chapter 4: for an armchair edge, the edge modes consist of an equal-weight superposition of the two valleys, while for the zigzag edge the edge states come from one of the valleys. In the bulk, one valley state determined by the order parameter is empty. Because the edge of graphene has zigzag as well as armchair parts, the hole edge mode will be different from the empty Landau sub-level at least in some regions along the boundary. Therefore, the valley-polarized $\nu = 0$ state does not support gapless edge modes.

From a general symmetry viewpoint advanced by Kane and Mele [133] the existence of counter-circulating gapless excitations is controlled by Z_2 invariants, protecting the spectrum for gap opening at the branch crossing.In the spin-polarized state [11] such invariant is provided by the z spin projection, σ_z. Thus when the σ_z conservation is violated (this can occur, for example, when spin-orbit of the Rashba type is present), a gap should open up at the branch crossing.

We point out that Z_2 invariant cannot be an operator in the valley space, because the two valleys are mixed by the edge disorder, which breaks any valley symmetry. This consideration confirms our argument above explaining the absence of gapless excitations in the valley-polarized state.

Thus the possible states near $\nu = 0$ can be broadly classified in two groups, as illustrated in Fig.6-2. The transport properties in these two situations are quite different. A pair of gapless edge excitations (Fig. 6-2a) provides dominant contribution to σ_{xx} when transport in the bulk is suppressed by an energy gap. Such systems will have $\sigma_{xx} \sim e^2/h \gg \sigma_{xy}$, i.e. nominally small Hall angle and apparently no QHE; no strong temperature dependence of the transport coefficients is expected. In addition, the longitudinal transport should have a *one-dimensional* character. Paradoxically, in such *dissipative QHE state* the roles of bulk and edge in transport interchange: the longitudinal response is due to edge states, while the transverse response is determined

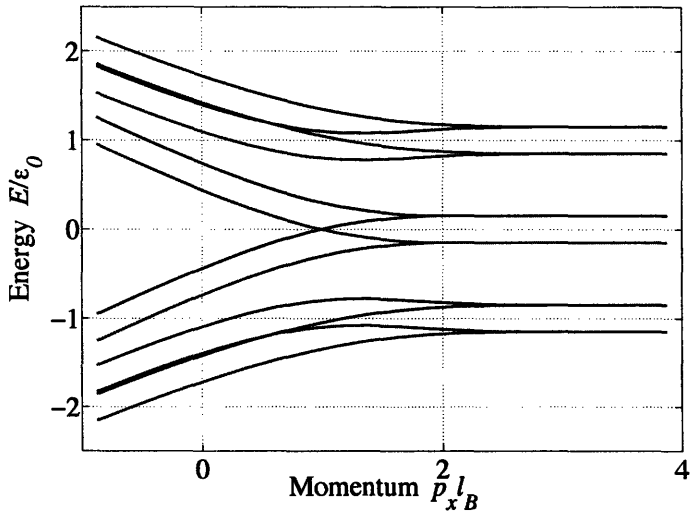

Figure 6-1: The spin-split graphene edge states, propagating in opposite directions at zero energy: the blue (red) curves represent the spin up (spin down) states.

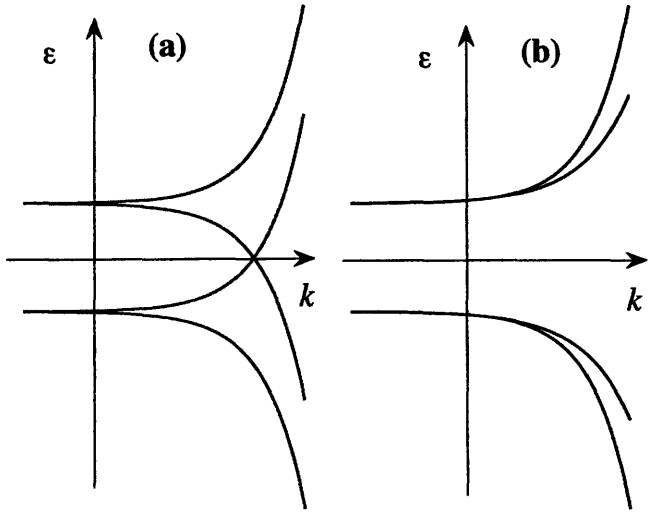

Figure 6-2: Excitation dispersion in $\nu = 0$ graphene QH state in a system with gapless chiral edge modes (a) and in the situation when gapless edge modes are not protected by symmetry or do not exist (b). Case (a) is realized in spin-polarized $\nu = 0$ state, described in Ref.[11], while case (b), for example, occurs in valley-polarized $\nu = 0$ state conjectured in Ref.[5]. In the latter a gap opens up at branch crossing due to valley mixing at the sample boundary.

mainly by the bulk properties.

In contrast, when there is a gap at the edge (Fig. 6-2(b)), longitudinal conductivity, being due to the bulk contribution, has a *two-dimensional* character. Since the bulk is gapped, σ_{xx} exhibits strong activated temperature dependence, vanishing in the limit of zero temperature. Naively, one expects the Hall conductivity σ_{xy} to behave similarly in both cases, exhibiting a flat plateau near $\nu = 0$. However, as we shall see below, in the gapless case this is not necessarily correct: the coupling between edge and bulk transport can change the flat plateau to a tilted feature.

To sum up, the two possible $\nu = 0$ QH states, spin-polarized and valley-polarized, exhibit very different edge states spectra. The spin-polarized state supports a pair of gapless counter-propagating edge states, which are absent in the valley-polarized state. This leads to a drastic difference in the behavior of σ_{xx}, which provides a tool to study the nature of the $\nu = 0$ state.

6.4 Spin transport properties

As we noted above, at the neutrality point, $\nu = 0$, graphene hosts gapless spin-polarized edge states (see Fig.6-1). In this Section we discuss interesting spin transport properties which arise due to the unusual edge states structure.

The Zeeman energy gap in the bulk,

$$E_Z = g\mu_B B \approx 45\,\mathrm{K} \text{ at } B = 30\,\mathrm{T}, \tag{6.1}$$

is enhanced by the Coulomb interaction. A Hartree-Fock estimate of this enhancement [11] is very similar to that in the QH bilayer systems (1.12), and gives a gap

$$\Delta = \frac{\pi^{1/2} e^2}{4\kappa\hbar v_0}(1-\alpha)\varepsilon_0 \approx 0.456 \cdot (1-\alpha)\varepsilon_0, \tag{6.2}$$

where $\kappa = 1 + \pi e^2/2\hbar v_0 \approx 5.24$ is RPA screening function, and the parameter $0 < \alpha < 1$ describes relative strength of Coulomb and exchange correlations (In our discussion of QH bilayers we took $\alpha = 0$). Assuming $\alpha = 0$, i.e. ignoring correlations of

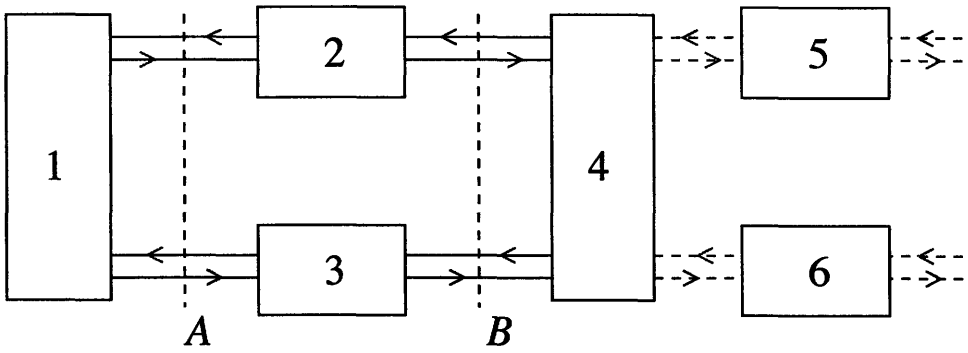

Figure 6-3: A Hall bar at $\nu = 0$ can be used to generate and detect spin currents. Blue and red lines represent edge currents with up and down spins. Contacts 1 and 4 are source and drain, which may be used to inject spin polarized current. Contacts 2, 3 are voltage probes with full spin mixing. The measured Hall voltage is directly related to spin current flowing in the system. An asymmetry between the upper and lower edges, e.g., introduced by removing voltage probe 3 or by gating, creates spin filtering effect: an unpolarized current injected from source 1 induces a spin-polarized current flowing into drain 4. Hall probes 5 and 6 downstream can serve as detectors of spin currents.

electrons with opposite spin, we obtain a spin gap $\Delta \sim 400\,\mathrm{K}$ for $B = 30\,\mathrm{T}$. Taking into account the substrate dielectric constant, $e^2 \to \frac{2}{\varepsilon+1}e^2$, changes the result only slightly ($\frac{2}{\varepsilon+1} = 0.36$ for SiO_2). This approximation, while pointing at a correct order of magnitude of a few hundred Kelvin, probably somewhat overestimates the spin gap since it ignores correlations and disorder effects.

The chiral spin-polarized edge states offer a unique setting to study spin transport. In particular, the spin-split state $\nu = 0$ may be used to generate and detect spin-polarized currents. This spin transport regime seems attractive due to the large bulk gap (6.2) and high stability of the edge states. Moreover, increased quality of samples should allow existence of spin polarized edge states even at relatively low magnetic fields.

The purpose of this section is mostly illustrative, and we will keep our discussion as simple as possible. In particular, we shall ignore transport in the bulk, leaving the discussion of its role for Sec. 6.5. We also first neglect spin flip backscattering between edge states within one edge. Estimates of the spin flip rate wil be given below, Eq.(6.4). A general approach, based on the Landauer-Büttiker formalism [125], which can be used to calculate spin and charge currents at the edge for any configuration

of current and voltage leads, was presented in Ref. [11].

In this approach, transport is described by a scattering matrix [125], with the edge states playing the role of scattering channels, and the reservoirs supplying in-states and absorbing out-states. Current in each mode is described by the relation $I_{\uparrow(\downarrow)} = \frac{e^2}{h}\varphi_{\uparrow(\downarrow)}$, where $\varphi_{\uparrow(\downarrow)}$ is the reservoir chemical potential for given spin projection. We consider the Hall bar geometry with four contacts 1-4 (see Fig.6-3), where the contacts 1 and 4 serve as current source and drain. For these two contacts we do not assume spin mixing, so that the injected and drained current may be spin polarized. The contacts 2, 3 are voltage probes, which means that they do not drain current from the system. Furthermore, we assume that the probes provide full spin mixing, i.e. chemical potentials of outgoing spin-up and spin-down electrons are equal.

The simplest situation arises when unpolarized current is injected through contact 1. Then the up- and down-spins spatially separate in a symmetric way, flowing along the opposite edges of the bar. This can be interpreted as circulating spin current, and described as spin-Hall effect with quantized spin conductance $\sigma_{xy}^{(\mathrm{spin})} = e^2/h$. No electric voltage will be induced between the voltage probes 2, 3 in this case (zero charge-Hall effect).

This device can be used as a detector of spin polarized current, made possible by the reciprocal of the spin Hall effect, in which the electric Hall voltage is directly related to spin rather than charge current. Suppose the up-spin and down-spin electrons, injected through contact 1, have unequal chemical potentials, $\varphi_\uparrow \neq \varphi_\downarrow$. Then the currents flowing into the probes 2 and 3, $I_{\uparrow(\downarrow)} = \frac{e^2}{h}\varphi_{\uparrow(\downarrow)}$, after equilibration and spin mixing in the probes, induce voltages $V_{2(3)} = \varphi_{\uparrow(\downarrow)}/2$. The resulting Hall voltage $V_{xy} = (\varphi_\downarrow - \varphi_\uparrow)/2$ is directly proportional to *spin current.* At the same time, an unpolarized current (for which $\varphi_\downarrow = \varphi_\uparrow$) flows symmetrically in the upper and lower edges without generating Hall voltage.

Spin transport at $\nu = 0$ also allows to realize spin filter. Suppose that the upper and lower edges of the device in Fig.6-3 are made asymmetric, which can be achieved, for example, simply by removing probe 3. Then we inject unpolarized current $2I$ through contact 1. The injected current will be distributed equally between the

upper and lower edges in cross section A. In cross section B, however, the net current will be spin polarized due to spin mixing in probe 2. The down-spin current reaching the drain in the upper edge equals $I/2$ while the up-spin current in the lower edge is I. Therefore, the total drained current becomes spin polarized. The spin polarized current can be fed into another system (see Fig.6-3), where it can be detected using Hall probes 5 and 6 as discussed above.

More complicated circuits can be assembled which generate spin currents and detect them elsewhere. Note that the important principle is that as long as backscattering is not allowed, the edge current can travel long distances and the circuit is nonlocal, just as in the integer QHE [125]. In this case the current-voltage relationship is obtained by solving the circuit equations as described in Ref.[11]. The spatial scale of nonlocality is controlled by spin relaxation which can be due to spin-orbit interaction or due to magnetic impurities near graphene edge.

Since the system is in strong magnetic field, the magnetic impurities will likely be polarized; this suggests that the primary source of spin relaxation is the spin-orbit interaction. There are two main spin-orbit terms in the graphene Hamiltonian [134, 135], the so called intrinsic and Rashba interaction, given by

$$H_{\rm SO} = \lambda_{\rm SO}\sigma_z\tau_z s_z, \quad H_{\rm R} = \lambda_{\rm R}(\sigma_x\tau_z s_y - \sigma_y s_x), \tag{6.3}$$

where Pauli matrices σ_i act in the sublattice space (two components of the Weyl spinor), while τ_i act in the valley space, and s_i represent physical spin. Estimates from band calculations [135] give $\lambda_{\rm R} \approx 0.1\,{\rm K}$ and a negligibly small $\lambda_{\rm SO} \approx 6\,{\rm mK}$.

To estimate the backscattering rate due to the spin-orbit interaction, we note that for an ideal atomically sharp edge the spin-orbit would couple the left and right states with the same momentum, opening a minigap at branch crossing: $\tilde{\varepsilon} = \pm\sqrt{\varepsilon^2 + {\lambda_{\rm R}}^2}$. However, this momentum-conserving interaction alone cannot backscatter edge states, and we need to take disorder into account. Edges of graphite monolayers have been imaged using STM probes [73, 72], where it was found that typically edge disorder can be viewed as patches of missing atoms of characteristic size $d \sim 1\,{\rm nm}$. Taking

into account the left-right branch mixing by spin-orbit $H_{\rm R}$, characterized by small mixing ratio of $\lambda_{\rm R}/|\varepsilon| \ll 1$ away from branch crossing, we obtain an estimate of the backscattering mean free path:

$$\ell(\varepsilon) \sim (\varepsilon/\lambda_{\rm R})^2(\ell_B/d)^2 d, \quad |\varepsilon| \gtrsim \lambda_{\rm R}, \tag{6.4}$$

which gives $\ell \sim 10\,\mu$m for typical $\varepsilon \sim 10\,$K. The factor $(\ell_B/d)^2 \gtrsim 1$ accounts for the magnetic field dependence of disorder matrix elements.

The quadratic energy dependence in (6.4), with spin flip rate having a sharp peak near branch crossing, suggests [11] the possibility to control backscattering using local gate. By tuning local chemical potential to and from the branch crossing, where the spin flip rate has a sharp peak, Eq.(6.4), we can induce or suppress backscattering in a controlled way. Spin filtering is achieved by controlling local gates on opposite sides of the Hall bar asymmetrically.

6.5 Dissipative QHE

We start this Section with briefly reminding the basic experimental observations near $\nu = 0$, which were already discussed in Section 1.4. Fig. 1-7 shows typical behavior of monolayer graphene samples [6] at 30 T where, besides the standard half-integer QHE sequence, the $\nu = 0$ plateau becomes clearly visible as an additional step in σ_{xy}. We note, however, that the step is not completely flat, and is not accompanied by a corresponding zero-resistance plateau in R_{xy}. Instead, R_{xy} exhibits a fluctuating feature away from zero (see Fig. 1-7). (In some devices R_{xy} can pass through zero in a smooth way without additional fluctuating features.) Moreover, R_{xx} does not exhibit a zero-resistance state either. Instead, it has a pronounced peak near the neutrality point which does not split at zero ν in any field. The value at the peak grows from $R_{xx} \approx h/4e^2$ in zero B (7.5 kΩ for the shown devices) [1] to $R_{xx} > 45\,$kΩ at 30 T (see inset of Fig. 1-7).

Spin flip backscattering (6.4) can be incorporated in the edge transport model,

described by coupled equations for particle density in the two spin-polarized modes:

$$\begin{aligned} &\partial_t n_1 + \partial_x \varphi_1 = \gamma(\varphi_2 - \varphi_1) \\ &\partial_t n_2 - \partial_x \varphi_2 = \gamma(\varphi_1 - \varphi_2), \quad n_i = \nu_i \varphi_i, \end{aligned} \tag{6.5}$$

where $\gamma^{-1} = \ell$ is the backscattering mean free path (6.4) taken for ε at the Fermi level, and $\nu_{1,2}$ are compressibilities of the modes. (For brevity, we use 1 and 2 instead of $\uparrow$ and $\downarrow$.) In writing Eqs.(6.5) we implicitly assume that fast energy relaxation maintains local equilibrium of each of the modes, which is consistent with metallic temperature dependence of transport coefficients [6].

In a stationary state, Eqs.(6.5) have an integral $\tilde{I} = \varphi_1 - \varphi_2$ which expresses current conservation at the edge. [In this section we use the units of $e^2/h = 1$.] The general solution in the stationary current-carrying state is

$$\varphi_{1,2}(x) = \varphi^*_{1,2} - \mathcal{E}x, \quad \mathcal{E} = \gamma \tilde{I} \tag{6.6}$$

Taking into account that $\tilde{I}$ is the current in one edge, we calculate the total current as

$$I = 2\tilde{I} = \frac{2}{\gamma}\mathcal{E} \tag{6.7}$$

To describe the longitudinal resistance in the four-terminal geometry, one must add potential drop on voltage probes [6], which gives $R = \frac{1}{2}(\gamma L + 1)$, where L is the distance between the probes. Comparing to the data for ρ_{xx} at $\nu = 0$ we estimate [6] $\ell \approx 0.5\,\mu$m. This mean free path value, which is relatively small on the scale predicted by Eq.(6.4), can be explained if spin flip processes are dominated by nonintrinsic effects, such as magnetic impurities localized near the edge.

It is crucial that the edge transport model (6.5) treats both edges of a Hall bar in an identical way, thus predicting zero Hall effect. In order to understand the observed density dependence of Hall coefficient [5, 6], which changes sign smoothly at $\nu = 0$ without exhibiting a plateau, and of ρ_{xx} which has a sharp peak at $\nu = 0$, we need to incorporate transport in the bulk in our model. In the full edge+bulk model, the

density dependence of transport coefficients arises from bulk currents short-circuiting edge currents away from $\nu = 0$. This explains, as we shall now see, the Hall effect, the peak of ρ_{xx}, the resistance fluctuations near $\nu = 0$, as well as the behavior of σ_{xx} and σ_{xy}.

We describe the transport problem in the bulk by the current-field relation, separately for each spin projection:

$$\mathbf{j}_i = -\hat{\sigma}_i \nabla \psi_i, \quad \hat{\sigma}_i = \left(\sigma_{xx}^{(i)} \sigma_{xy}^{(i)} - \sigma_{xy}^{(i)} \sigma_{xx}^{(i)}\right), \quad i = 1, 2,$$

where $\psi_{1,2}$ are electrochemical potentials for two spin states. We assume that the bulk conductivities $\sigma_{xx}^{(1,2)}$, as a function of density ν, are peaked at the spin-split Landau levels. For simplicity, here we ignore possible valley splitting, in which case the spin up and down Landau levels occur at $\nu = \pm 1$ around the Dirac point. As a simplest model, below we use Gaussians

$$\sigma_{xx}^{(1)}(\nu) = e^{-A(\nu-1)^2}, \quad \sigma_{xx}^{(2)}(\nu) = e^{-A(\nu+1)^2} \tag{6.8}$$

with the parameter A describing the width of the levels. The Hall conductivities $\sigma_{xy}^{(1,2)}$ exhibit plateaus on either side of the peak in $\sigma_{xx}^{(1,2)}$. The dependence of $\sigma_{xy}^{(1,2)}$ on ν can be modeled with the help of the semicircle relation $\sigma_{xy}^{(1,2)}(\sigma_{xy}^{(1,2)} \mp 2) + (\sigma_{xx}^{(1,2)})^2 = 0$ which often provides a good description of conventional QHE systems [104], and more recently has been demonstrated to hold in graphene [110].

The condition of charge continuity, $\nabla \mathbf{j}_i = 0$, gives a 2d Laplace's equation for the potentials, $\nabla^2 \psi_i = 0$. This equation must be solved together with the boundary conditions phenomenologically describing bulk-edge coupling:

$$\mathbf{n}.\mathbf{j}_i = g(\psi_i - \varphi_i) \tag{6.9}$$

where $\mathbf{n}$ is a normal vector to the boundary, and $g(\psi_i - \varphi_i)$ represents the edge-bulk leakage current density.

Although a general solution of this problem can be given with the help of Fourier

method, here we consider only the case when the potentials $\psi_i(\mathbf{x})$ are varying slowly on the scale of the bar width w, which will suffice for our analysis of a homogeneous current flow. In this case, linearizing $\psi_i(\mathbf{x})$ in the direction transverse to the bar, we can write Eqs.(6.9) for both edges of the bar as

$$\begin{aligned} -\sigma_{xy}\partial_x\psi_i + \sigma_{xx}(\psi_{i'} - \psi_i)/w &= g(\psi_i - \varphi_i) \\ \sigma_{xy}\partial_x\psi_{i'} + \sigma_{xx}(\psi_i - \psi_{i'})/w &= g(\psi_{i'} - \varphi_{i'}), \end{aligned} \tag{6.10}$$

$i = 1, 2$, where the primed and unprimed quantities denote variables at opposite edges of the bar.

Equations for the edge variables φ_i are obtained by adding the bulk-edge leakage term to Eqs.(6.5), giving

$$\begin{aligned} \partial_x\varphi_1 &= \gamma(\varphi_2 - \varphi_1) + g(\psi_1 - \varphi_1), \\ -\partial_x\varphi_2 &= \gamma(\varphi_1 - \varphi_2) + g(\psi_2 - \varphi_2), \end{aligned} \tag{6.11}$$

along with a similar pair of equations for $\varphi_{1'}$, $\varphi_{2'}$ at the opposite edge.

The solution of these eight equations, describing uniform current, is of the form $\varphi_i = \varphi_i^* - \mathcal{E}x$, $\psi_i = \psi_i^* - \mathcal{E}x$, etc., with the same linear part $-\mathcal{E}x$ for all quantities. Using the algebraic structure of this linear system and the symmetry between the edges, we reduce the number of equations from eight to two. First, it is convenient to express the parameters φ_i^* through ψ_i^* using Eqs.(6.11), which gives

$$\begin{aligned} \varphi_1^* &= \tfrac{\gamma+g}{2\gamma+g}\psi_1^* + \tfrac{\gamma}{2\gamma+g}\psi_2^* + \tfrac{\mathcal{E}}{2\gamma+g} \\ \varphi_2^* &= \tfrac{\gamma+g}{2\gamma+g}\psi_2^* + \tfrac{\gamma}{2\gamma+g}\psi_1^* - \tfrac{\mathcal{E}}{2\gamma+g} \end{aligned} \tag{6.12}$$

Writing similar equations for the variables at the opposite edge to express $\varphi_{1'}$, $\varphi_{2'}$ through $\psi_{1'}$, $\psi_{2'}$, and substituting the result in Eqs.(6.10), we obtain four equations

for ψ_i and $\psi_{i'}$ which have the form

$$\begin{aligned}
-\tilde{\sigma}_{xy}^{(1)} w\mathcal{E} &= \sigma_{xx}^{(1)}(\psi_{1'}^* - \psi_1^*) + \lambda(\psi_2^* - \psi_1^*) \\
\tilde{\sigma}_{xy}^{(1)} w\mathcal{E} &= \sigma_{xx}^{(1)}(\psi_1^* - \psi_{1'}^*) + \lambda(\psi_{2'}^* - \psi_{1'}^*) \\
-\tilde{\sigma}_{xy}^{(2)} w\mathcal{E} &= \sigma_{xx}^{(2)}(\psi_{2'}^* - \psi_2^*) + \lambda(\psi_1^* - \psi_2^*) \\
\tilde{\sigma}_{xy}^{(2)} w\mathcal{E} &= \sigma_{xx}^{(2)}(\psi_2^* - \psi_{2'}^*) + \lambda(\psi_{1'}^* - \psi_{2'}^*)
\end{aligned} \tag{6.13}$$

where the coefficients in this linear system are defined as

$$\tilde{\sigma}_{xy}^{(1,2)} = \sigma_{xy}^{(1,2)} \pm \frac{g}{2\gamma + g}, \quad \lambda = \frac{w\gamma g}{2\gamma + g}. \tag{6.14}$$

The quantities $\tilde{\sigma}_{xy}^{(1,2)}$ represent the sum of the bulk and edge contributions to Hall conductivity for each spin.

Symmetry between the edges allows to further reduce the number of independent variables. For that we add the first two equations to obtain $\psi_1^* + \psi_{1'}^* = \psi_2^* + \psi_{2'}^*$. Also we note that all potentials can be changed by the same constant that can be chosen so that the new quantities ψ_i^* and $\psi_{i'}^*$ satisfy $\psi_i^* = -\psi_{i'}^*$. After that Eqs.(6.13) yield

$$\begin{aligned}
\tilde{\sigma}_{xy}^{(1)} w\mathcal{E} &= 2\sigma_{xx}^{(1)}\psi_1^* - \lambda(\psi_2^* - \psi_1^*) \\
\tilde{\sigma}_{xy}^{(2)} w\mathcal{E} &= 2\sigma_{xx}^{(2)}\psi_2^* - \lambda(\psi_1^* - \psi_2^*)
\end{aligned} \tag{6.15}$$

These two equations can be solved to find $\psi_{1,2}^*$.

Now we can find the current as a sum of the edge and bulk contributions, $I = I_{\text{edge}} + I_{\text{bulk}}$, where

$$I_{\text{edge}} = \varphi_1 - \varphi_2 + \varphi_{2'} - \varphi_{1'} = 2(\varphi_1^* - \varphi_2^*)$$

and

$$I_{\text{bulk}} = \sigma_{xy}^{(1)}(\psi_1 - \psi_{1'}) + \sigma_{xx}^{(1)} w\mathcal{E} + \sigma_{xy}^{(2)}(\psi_2 - \psi_{2'}) + \sigma_{xx}^{(2)} w\mathcal{E}$$

After expressing φ_i through ψ_i with the help of Eqs.(6.12) and using the solution of

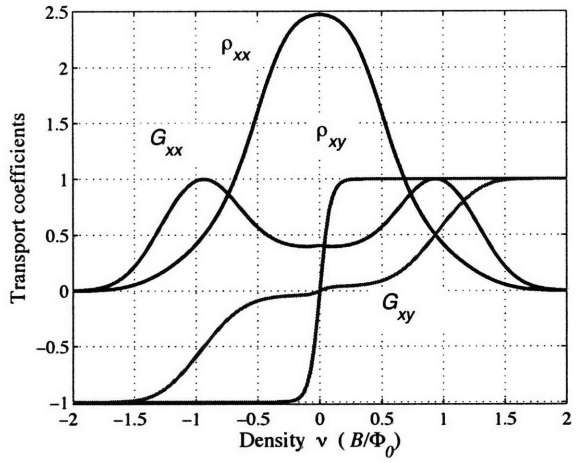

Figure 6-4: Density dependence of transport coefficients $\rho_{xx} = \tilde{\gamma}w/2$, $\rho_{xy=\tilde{\gamma}\xi/2}$ and $G_{xx} = \rho_{xy}/({\rho_{xy}}^2 + {\rho_{xx}}^2)$, $G_{xy} = \rho_{xy}/({\rho_{xy}}^2 + {\rho_{xx}}^2)$, obtained from the edge transport model (6.11) augmented with bulk conductivity, Eqs.(6.10) (see Eqs.(6.16),(6.17) and text). Parameter values: $A = 6$, $\gamma w = 5$. Note the peak in ρ_{xx}, the smooth behavior of ρ_{xy} near $\nu = 0$, a quasi-plateau in G_{xy}, and a double-peak structure in G_{xx}.

Eqs.(6.15), we obtain a relation $I = 2\mathcal{E}/\tilde{\gamma}$, where

$$\frac{2}{\tilde{\gamma}} = \frac{4}{2\gamma + g} + \frac{w}{\rho_{xx}^{(1)}} + \frac{w}{\rho_{xx}^{(2)}} - \frac{\lambda w \left(\tilde{\sigma}_{xy}^{(1)}/\sigma_{xx}^{(1)} - \tilde{\sigma}_{xy}^{(2)}/\sigma_{xx}^{(2)}\right)^2}{2 + \lambda/\sigma_{xx}^{(1)} + \lambda/\sigma_{xx}^{(2)}}. \tag{6.16}$$

The quantities $\rho_{xx}^{(1,2)}$ are defined as $\rho_{xx}^{(i)} = \sigma_{xx}^{(i)}/(\tilde{\sigma}_{xy}^{(i)2} + \sigma_{xx}^{(i)2})$. The quantity $\tilde{\gamma}$, Eq.(6.16), replaces γ in Eq.(6.7). In the absence of bulk conductivity, $\sigma_{xx}^{(1,2)} \to 0$, we recover the result for pure edge transport, $\tilde{\gamma} = \gamma$.

The Hall voltage can be calculated from this solution as $V_H = \frac{1}{2}(\varphi_1 + \varphi_2 - \varphi_{1'} - \varphi_{2'})$, where φ_i, $\varphi_{i'}$ are variables at opposite edges. We obtain $V_H = \xi\mathcal{E}$, where

$$\xi = 2w \frac{\tilde{\sigma}_{xy}^{(1)}\left(\lambda + \sigma_{xx}^{(2)}\right) + \tilde{\sigma}_{xy}^{(2)}\left(\lambda + \sigma_{xx}^{(1)}\right)}{2\sigma_{xx}^{(1)}\sigma_{xx}^{(2)} + \lambda\sigma_{xx}^{(2)} + \lambda\sigma_{xx}^{(1)}}. \tag{6.17}$$

This quantity vanishes at $\nu = 0$, since $\sigma_{xy}^{(1)} = -\sigma_{xy}^{(2)}$ and $\sigma_{xx}^{(1)} = \sigma_{xx}^{(2)}$ at this point due to particle-hole symmetry.

Transport coefficients, obtained from this model for typical parameter values, are displayed in Fig.6-4 which reproduces many of the key features of the data (see Fig.1

in Ref.[6]). In particular, the peak in ρ_{xx} is due to edge transport near $\nu = 0$. The suppression of ρ_{xx} at finite ν is due to the bulk conductivity short-circuiting the edge transport. The bulk and edge contributions to transport can be discerned from the double peak structure in G_{xx} in Fig.6-4. The peaks correspond to the bulk Landau level contributions, Eq.(6.8), whereas the part of G_{xx} between the peaks, exceeding the superposition of two Gaussians, Eq.(6.8), is the edge contribution. The Hall resistance ρ_{xy} is nonzero due to imbalance in $\sigma_{xy}^{(1,2)}$ for opposite spin polarizations away from $\nu = 0$. Interestingly, ρ_{xy} in Fig.6-4 exhibits no plateau, while G_{xy} calculated from ρ_{xy} and ρ_{xx} displays an under-developed plateau-like feature. Overall, this behavior resembles that of the experimentally measured transport coefficients [5, 6].

Another notable feature of the measured ρ_{xy} and ρ_{xx} is enhanced fluctuations near zero ν. These fluctuations are found to be strong in Ref.[5], where ρ_{xy} changes sign several times near $\nu = 0$. They are also present, although are not as dramatic, in Ref.[6]. In the latter case, both ρ_{xy} and ρ_{xx} exhibit noisy behavior in the interval near $\nu = 0$ comparable to the ρ_{xx} peak width. As Ref.[6] points out, this behavior is consistent with the edge transport model. In the absence of bulk transport, the distribution of potential along the edge depends on the local backscattering rate $\gamma(x)$, whereby Eq.(6.6) is replaced by

$$\varphi_{1,2}(x) = \varphi_{1,2}(0) - \tilde{I} \int_0^x \gamma(x')dx'.$$

Fluctuations of γ arise due to its sensitivity to the local value of Fermi energy in the spin-orbit scattering model, Eq.(6.4), and, similarly, for the magnetic impurity scattering mechanism. Assuming that the random part of γ is of a white noise character, we obtain strong fluctuations $\delta\varphi_{1,2}(x)$ along the edge of magnitude that scales as a square root of the edge length. These fluctuations will contribute equally to the longitudinal and transverse voltage, since they are uncorrelated on the opposite sides of the Hall bar. The absence of fluctuations away from $\nu = 0$ can be understood as a result of bulk conductivity short-circuiting the edge current, which will equilibrate potentials on the opposite sides of the Hall bar.

The above discussion summarizes the results drawn from an attempt to model quantum Hall transport in graphene at $\nu = 0$ by counter-circulating edge states. By taking into account backscattering within one edge as well as conduction in the bulk which short-circuits edge transport away from the neutrality point, this model accounts for the observed behavior of transport coefficients. Still, since no direct evidence for spin polarization has yet been found, more experimental and theoretical work will be needed to confirm the chiral spin-polarized edge picture of the $\nu = 0$ state. If proven to exist in graphene, these states will provide a unique setting to study spin transport as well as other interesting phenomena.

Chapter 7

Order from Disorder in Graphene Quantum Hall Ferromagnet

7.1 Abstract

Valley-polarized quantum Hall states in graphene are described by a Heisenberg O(3) ferromagnet model, with the ordering type controlled by the strength and sign of valley anisotropy. A mechanism resulting from electron coupling to strain-induced gauge field, giving leading contribution to the anisotropy, is described in terms of an effective random magnetic field aligned with the ferromagnet z axis. We argue that such random field stabilizes the XY ferromagnet state, which is a coherent equal-weight mixture of the K and K' valley states. The implications such as the Berezinskii-Kosterlitz-Thouless ordering transition and topological defects with half-integer charge are discussed. The results presented in this Chapter are published in Ref. [48].

7.2 Introduction

As we have discussed in Section 1.4, the Landau levels (LL) in graphene split [5] in strong magnetic fields of about 15 T, with the $n = \pm 1$ and $n = 0$ levels forming two and four sub-levels, respectively, as illustrated in Fig.7-1a. The observed splittings

were attributed to spin and valley degeneracy lifted by the Zeeman and exchange interactions.

The physics of the interaction-induced gapped quantum Hall state is best understood by analogy with the well-studied quantum Hall bilayers realized in double quantum well systems [17]. In the latter, the interaction is nearly degenerate with respect to rotations of pseudospin describing the two wells. The states with odd filling factors exhibit pseudospin O(3) ordering, the so-called quantum Hall ferromagnet (QHFM) [17]. The pseudospin z component describes density imbalance between the wells, while the x and y components describe the inter-well coherence of electron states. Several different phases [77, 76] are possible in QHFM depending on the strength of the anisotropic part of Coulomb interaction, controlled by well separation.

In the case of graphene, with all electrons moving in a single plane, the valleys K and K' play the role of the two wells in the pseudospin representation with the lattice constant replacing the inter-well separation. To assess the possibility of QHFM ordering, we note that the magnetic length at the $10-30\,\mathrm{T}$ field is much greater than the lattice constant. Thus graphene QHFM can be associated with the double-well systems with nearly perfect pseudospin symmetry of Coulomb interaction [81, 84, 83]. Our estimate [136] (see below) yields anisotropy magnitude of about $10\,\mu\mathrm{K}$ at $B \sim 30\,\mathrm{T}$, which is very small compared to other energy scales in the system.

What else can break pseudospin symmetry? Coupling to disorder seems an unlikely candidate at first glance. However, there is an interesting effect that received relatively little attention, which is strain-induced random gauge field introduced by Iordanskii and Koshelev [12]. To clarify its origin, let us consider the tight-binding model with spatially varying hopping amplitudes. Physically, such variation can be due to local strain, curvature [137, 138] or chemical disorder. With hopping amplitudes t_i for three bond orientations varying independently, we write

$$\varepsilon \begin{pmatrix} u \\ v \end{pmatrix} = \begin{bmatrix} 0 & \tau_{\mathbf{q}} \\ \tau_{\mathbf{q}}^* & 0 \end{bmatrix} \begin{pmatrix} u \\ v \end{pmatrix}, \quad \tau_{\mathbf{q}} = \sum_{i=1,2,3} t_i e^{i\mathbf{q}\cdot\mathbf{e}_i}, \tag{7.1}$$

where $\mathbf{e}_i$ are vectors connecting a lattice site to its nearest neighbors, and u and v

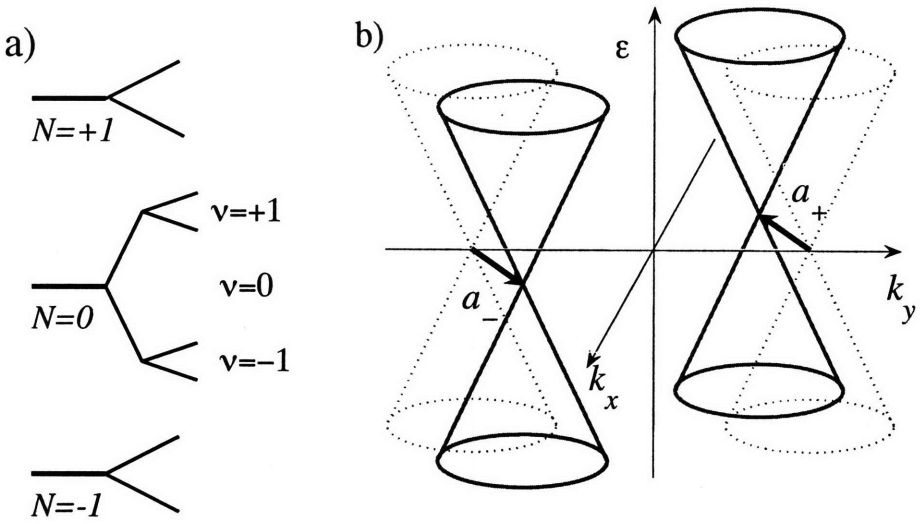

Figure 7-1: a) Graphene Landau level splitting, Ref.[5], attributed to spin and valley polarization. When the Zeeman energy exceeds valley anisotropy, all $n = 0$ states are spin-polarized, with the $\nu = \pm 1$ states valley-polarized and the $\nu = 0$ state valley-unpolarized. b) The effect of uniform strain on electron spectrum, Ref.[12], described by Dirac cones shift in opposite directions from the points K and K'. Position-dependent strain is described as a random gauge field, Eq.(7.2).

are wavefunction amplitudes on the two non-equivalent sublattices, A and B. The low-energy Hamiltonian for the valleys K and K' is obtained at $\mathbf{q} \approx \pm\mathbf{q}_0$, the non-equivalent Brillouin zone corners:

$$H_\pm = v \begin{bmatrix} 0 & ip_x \mp p_y + \frac{e}{c}a_\pm \\ -ip_x \mp p_y + \frac{e}{c}a_\pm^* & 0 \end{bmatrix} \tag{7.2}$$

with $a_\pm = \frac{c}{e}\sum_{i=1,2,3} \delta t_i e^{\pm i\mathbf{q}_0 \cdot \mathbf{e}_i}$, where the subscript $+(-)$ corresponds to $K(K')$ valley. In writing Eq.(7.2) we use Cartesian coordinates with the x axis in the armchair direction. Decomposing $a_\pm = a_y \mp i a_x$, we see that the effective vector potential in the two valleys is given by $\pm(a_x, a_y)$. Notably, the gauge field a_μ is of opposite sign for the two valleys, thus preserving time-reversal symmetry (see Fig.7-1b).

Here we assume that the gauge field has white noise correlations with a correlation length ξ,

$$\langle a_i(k) a_j(k) \rangle_{k\xi \ll 1} = \alpha^2, \quad a_i(k) = \int e^{-ikr} a_i(r) d^2 r, \tag{7.3}$$

as appropriate for white noise fluctuations of δt_i. The fluctuating effective magnetic

field can be estimated as

$$\delta h(x) = \partial_x a_y - \partial_y a_x \sim \alpha/\xi^2, \tag{7.4}$$

whereby the correlator of Fourier harmonics $\langle \delta h_k \delta h_{-k} \rangle$ behaves as k^2 at $k\xi \ll 1$.

Recently, strain-induced effective magnetic field was employed to explain anomalously small weak localization in graphene [29]. A direct observation of graphene ripples [29] yields typical corrugation length scale ξ of a few tens of nanometers. Estimates from the first principles [29] gave $\delta h \sim 0.1 - 1\,\mathrm{T}$, consistent with the observed degree of weak localization suppression.

Valley anisotropy of coupling to the gauge field, Eq.(7.2), generates a uniaxial random Zeeman-like interaction $\delta h \sigma_3$ for the K-K' pseudospin order parameter. We shall see that, somewhat counterintuitively, weak δh induces ordering in the system, acting as an easy plane anisotropy which favors the XY state. This behavior can be understood by noting that the transverse fluctuations in a ferromagnet are softer than the longitudinal fluctuations, making it beneficial for the spins to be polarized, on average, transversely to the field, as illustrated in Fig.7-2. This *random field-induced ordering* maximizes the energy gain of the spin system coupled to δh.

For magnets with uniaxial random field this behavior has been established [139, 140] in high space dimension. The situation in dimension two is considerably more delicate [141, 142] due to competition with the Larkin-Imry-Ma (LIM) [143, 144] disordered state. We shall see that the anisotropy induced by random gauge field is more robust than that due to random magnetic field. (This scenario of randomness-induced order is also relevant for the two-valley QH in AlAs system [75].)

The field-induced easy-plane anisotropy completely changes thermodynamics, transforming an O(3) ferromagnet, which does not order in 2d, to the XY model which exhibits a Berezinskii-Kosterlitz-Thouless transition to an ordered XY state. The transition temperature T_{BKT} is logarithmically renormalized by the out-of-plane fluctuations [145],

$$T_{BKT} \sim J/\ln(l_{XY}/\ell_B), \quad \ell_B = (\hbar c/eB)^{1/2}, \tag{7.5}$$

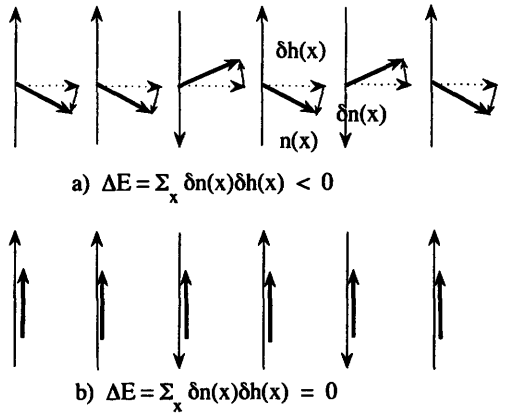

Figure 7-2: Random field-induced order in a ferromagnet. The energy gained from the order parameter tilting opposite to the field is maximal when the spins and the field are perpendicular (a), and minimal when they are parallel (b). Uniaxial random field induces XY ordering in the transverse plane.

where l_{XY} is the correlation length. For fields $B \sim 30\,\mathrm{T}$, with l_{XY} given by Eq.(7.16) below, we obtain T_{BKT} in the experimentally accessible range of a few Kelvin.

The XY-ordered QHFM state hosts fractional $\pm e/2$ charge excitations, so-called merons [76]. Merons are vortices such that in the vortex core the order parameter smoothly rotates out of the xy plane. There are four types of merons [76], since a meron can have positive or negative vorticity and the order parameter inside the core can tilt either in $+z$ or $-z$ direction. A pair of merons with the same charge and opposite vorticity is topologically equivalent to a skyrmion of charge $2(e/2) = e$ [76].

7.3 Random vector potential and valley anisotropy

In graphene QHFM, the hierarchy of the spin- and valley-polarized states is determined by relative strength of the Zeeman energy and the randomness-induced anisotropy. Our estimate below obtains the anisotropy of a few Kelvin at $B \sim 30\,\mathrm{T}$. This is smaller than the Zeeman energy in graphene, $\Delta_z = g\mu_B B \sim 50\,\mathrm{K}$ at $B \sim 30\,\mathrm{T}$. Therefore we expect that $\nu = 0$ state is spin-polarized, with both valley states filled. (This was assumed in our previous analysis [11] of edge states in $\nu = 0$ state.) In contrast, in highly corrugated samples, when the anisotropy exceeds the Zeeman energy,

an easy-plane valley-polarized $\nu = 0$ state can be favored.

While the character of $\nu = 0$ state is sensitive to the anisotropy strength, the $\nu = \pm 1$ states (see Fig.7-1a) are always both spin- and valley-polarized. Below we focus on $\nu = \pm 1$ states, keeping in mind that for strong randomness our discussion also applies to $\nu = 0$ state.

Zeeman-split free Dirac fermion LL are given by

$$E_n = \mathrm{sgn}(n)\sqrt{|2n|}\frac{\hbar v}{\ell_B} \pm \Delta_z, \tag{7.6}$$

with n integer and $v \approx 8 \times 10^7$ cm/s. Each LL is doubly valley-degenerate. Random field (7.4) couples to electron orbital motion in the same way as the external field B, producing a local change in cyclotron energy and in the LL density. While the random field splits the $n \neq 0$ LL, for $n = 0$, it does not affect the the single-particle energy (7.6) and couples to electron dynamics via exchange effects only. To estimate this coupling, we note that the field (7.4) leads to valley imbalance in exchange energy per particle:

$$E_{\mathrm{K(K')}} = E_{\mathrm{exch}}(B \pm \delta h) = \frac{Ae^2}{\kappa \ell_{B\pm\delta h}}, \quad A = \left(\frac{\pi}{8}\right)^{1/2}, \tag{7.7}$$

where κ is the dielectric constant of graphene.

Let us analyze the graphene QHFM energy dependence on the gauge field. We consider a fully spin- and valley-polarized $\nu = -1$ state, described by a ferromagnetic order parameter $\mathbf{n} = (n_1, n_2, n_3)$ in the K, K' valley space. The valley-isotropic exchange interaction gives rise to a sigma model, with the gradient term only [77]:

$$E_0(n) = \frac{1}{2}\int J(\nabla \mathbf{n})^2 d^2x, \quad J = \frac{e^2}{64\kappa\ell_B}. \tag{7.8}$$

The valley-asymmetric coupling to δh in Eq.(7.7) generates a Zeeman-like Hamiltonian with a uniaxial random field.

$$E_1(n) = \int g\delta h(x) n_3(x) d^2x, \quad g = n\frac{dE_{\mathrm{exch}}}{dB} = \frac{Ane^2}{2B\kappa\ell_B}, \tag{7.9}$$

where $n = 1/2\pi\ell_B^2$ is the electron density.

We estimate the energy gain from the order parameter $\mathbf{n}(x)$ correlations with the random field, treating the anisotropy (7.9) perturbatively in δh. Decomposing $\mathbf{n}(x) = \bar{\mathbf{n}} + \delta\mathbf{n}(x)$ and taking variation in $\delta\mathbf{n}$, we obtain

$$J\nabla^2\delta\mathbf{n} = g\delta\mathbf{h}_\perp, \quad \delta\mathbf{h}_\perp = (\mathbf{z} - \bar{\mathbf{n}}(\bar{\mathbf{n}}\cdot\mathbf{z}))\delta h.$$

Substituting the solution for $\delta\mathbf{n}$ into the energy functional (7.8), (7.9), we find an energy gain for $\bar{\mathbf{n}}$ of the form

$$\delta E = -\lambda\int(1-\bar{n}_3^2(x))d^2x, \quad \lambda = \sum_k \frac{g^2\langle\delta h_{-k}\delta h_k\rangle}{2Jk^2}, \tag{7.10}$$

where averaging over spatial fluctuations of δh is performed. This anisotropy favors the XY state, $\bar{n}_3 = 0$. As illustrated in Fig.7-2, the fluctuations due to $\delta\mathbf{n}$ tilting towards the z-axis minimize the energy of coupling to the uniaxial field when $\bar{\mathbf{n}}$ is transverse to it.

Now, let us compare the energies of the XY and the Larkin-Imry-Ma state [143, 144]. In LIM state the energy is lowered by domain formation such that the order parameter in each domain is aligned with the average field in this domain. Polarization varies smoothly between domains, and the typical domain size L is determined by the balance between domain wall and magnetic field energies. In our system, the LIM energy per unit area is

$$\varepsilon_{LIM} \sim -\frac{g\Phi(L)}{L^2} + \frac{J}{L^2}, \tag{7.11}$$

where $\Phi(L)$ is typical flux value through a region of size L. To estimate $\Phi(L)$ we write the magnetic flux through a region of size L as an integral of the vector potential over the boundary, which gives

$$\Phi(L) = \oint a_i(x)\,dx_i \sim \alpha\sqrt{L/\xi}. \tag{7.12}$$

Minimizing the LIM energy (7.11), we find

$$\varepsilon_{LIM} \sim -\frac{g^4\alpha^4}{J^3\xi^2}. \tag{7.13}$$

Comparison to the XY anisotropy $\lambda \sim -g^2\alpha^2/J\xi^2$ gives

$$\frac{\lambda}{\varepsilon_{LIM}} \sim \frac{J^2}{g^2\alpha^2} \sim \left(\frac{\Phi_0}{\Phi(\xi)}\right)^2, \quad \Phi_0 = hc/e, \tag{7.14}$$

where $\Phi(\xi) \sim \alpha$ is the flux through a region of size ξ. Interestingly, the ratio (7.14) does not depend on the external magnetic field. Therefore, at weak randomness, when the random field flux through an area ξ^2 is much smaller than Φ_0, the ordered XY state has lower energy than the disordered LIM state.

In the opposite limit of strong randomness spins align with the local δh, forming a disordered state. It is instructive to note that for a model with white noise correlations of magnetic field, rather than of vector potential, the ratio (7.14) is of order one. In this case the competition of the LIM and the ordered states is more delicate.

A different perspective on the random-field-induced ordering is provided by analogy with the classical dynamics of a pendulum driven at suspension [146]. The latter, when driven at sufficiently high frequency, acquires a steady state with the pendulum pointing along the driving force axis. As discussed in Ref. [147], this phenomenon can be described by an effective potential U_{eff} obtained by averaging the kinetic energy over fast oscillations, with the minima of U_{eff} on the driving axis and maxima in the equatorial plane perpendicular to it. This behavior is robust upon replacement of periodic driving by noise [148]. Our statistical-mechanical problem differs from the pendulum problem merely in that the 1d time axis is replaced by 2d position space, which is inessential for the validity of the argument. The resulting effective potential is thus identical to that for the pendulum, with the only caveate related to the sign change $U_{\text{eff}} \to -U_{\text{eff}}$ in the effective action, as appropriate for transition from classical to statistical mechanics. Thus in our case the minima of U_{eff} are found in the equatorial plane, in agreement with the above discussion.

The easy-plane anisotropy (7.10) can be estimated as

$$\lambda/n \sim \frac{\delta h^2}{B^2} \times \frac{\xi^2}{\ell_B^2} \times \frac{e^2}{\kappa \ell_B} \approx 0.1 - 10 \text{ K/particle}, \tag{7.15}$$

where $\delta h \sim 0.1 - 1\,\mathrm{T}$, $\xi \sim 30\,\mathrm{nm}$ and $B \sim 30\,\mathrm{T}$ was used. Since this is smaller than the Zeeman energy, we expect that the easy-plane ferromagnet in the valley space is realized at $\nu = \pm 1$, while $\nu = 0$ state is spin polarized with both valley states filled.

The out-of-plane fluctuations of the order parameter are characterized by the correlation length

$$l_{XY} \sim \sqrt{J/\lambda} \approx 1 - 10\,\ell_B \tag{7.16}$$

for the above parameter values. The length l_{XY} sets a typical scale for order parameter change in the core of vortices (merons) as well as near edges of the sample and defects which induce non-zero z-component.

To measure the correlation length l_{XY} one may use the spatial structure of $\nu = 0$ wavefunction. Since the $K(K')$ electrons reside solely on either B or A sublattice, the order parameter z-component is equal to the density imbalance between the two sublattices. The latter can be directly measured by STM imaging technique. For the temperature of XY ordering, Eq.(7.5), with J estimated from (7.8), we obtain T_{BKT} on a few Kelvin scale.

This should be compared to the intrinsic QHFM valley anisotropy of a pure graphene sheet. In the zeroth LL, the K-K' superposition states have a somewhat different density distribution than the valley-polarized states, since for each valley the zeroth LL occupies just one sublattice (A for K', B for K). In particular, electrons occupy both sublattices equally in the state with the order parameter in the xy plane. This leads to a dependence of the QHFM Coulomb energy on the orientation of the order parameter. This anisotropy, estimated using the Hartree-Fock approximation [136], was found to be

$$\Delta E \approx -\frac{27}{512\pi^3} \times \left(\frac{a}{\ell_B}\right)^3 \times \frac{e^2}{\kappa \ell_B} \sim 10\,\mu\mathrm{K} \tag{7.17}$$

indicating that the anisotropy is negligible.

We note that the situation is completely different for higher LL. Goerbig et al. [84] pointed out that the Coulomb interaction can backscatter electrons of K and K' type at LL with $n \neq 0$, which leads to a much stronger lattice anisotropy of the order a/l_B. This effect is absent for the zeroth LL due to the fact that K and K' states occupy different sublattices

7.4 Summary

In summary, we studied the valley symmetry breaking of graphene QHFM. We considered the coupling of the strain-induced random magnetic field and found that it generates an easy-plane anisotropy, which is much stronger than the symmetry-breaking terms due to lattice. The estimates of the field-induced anisotropy suggest that the random field may be a principal mechanism of K-K' QHFM symmetry breaking. The easy-plane ordered state is expected to exhibit BKT transition at experimentally accessible temperatures and half-integer charge excitations.

Chapter 8

Summary and outlook

8.1 Summary

In conclusion, we have considered new effects arising in graphene due to the Dirac spectrum of its low-energy excitations. We have focused on the QHE regime, where many interesting phenomena occur. First in Chapter 2 we have studied the general properties of the two-terminal conductance as a function of sample shape. Employing conformal invariance of the conductance, we were able to classify all possible shapes by a single parameter, the aspect ratio of an equivalent rectangular sample. Solving the conduction problem for the rectangular case, we have identified conductance features in the QHE regime which can be used as a tool for sample diagnostics. Furthermore, in Chapter 3 we have illustrated the use of our model for the characterization of experimental devices.

A microscopic picture of edge states in the anomalous QHE in graphene has been presented in Chapter 4. There we have also discussed how STM can be used to probe properties of the edge states. In Chapter 5, we have found that the electron-hole symmetry of the Dirac spectrum gives rise to new edge states transport regimes in the locally gated graphene devices, p-n and p-n-p, junctions resulting in fractional and integer conductance quantization.

In Chapter 6, we pointed out a possibility of counter-circulating spin-polarized edge states near the Dirac point, which exhibit unusual charge transport properties

and may allow realization of interesting spin transport phenomena. Finally, in Chapter 7 we studied graphene valley QHFM, arguing that coupling of the ferromagnetic order parameter to the strain-induced random vector potential, an interesting disorder type present in graphene, leads to an easy-plane ordering of the QHFM. This gives rise to a BKT transition at low, but experimentally accessible temperatures, and to fractionally charged vortices appearing below the BKT transition temperature.

8.2 Outlook

Because the very productive and promising is still at its infancy, many interesting phenomena are still yet to be understood. This applies to some of the phenomena in the QHE regime which we have studied in this thesis as well. While most of our findings presented in Chapters 2-5 have been confirmed by experiments, the ferromagnetic states described in Chapters 6 and 7 are still under investigation and debate [6, 80, 99]. In particular, the nature of the $\nu = 0$ state which we have considered in Chapter 6 remains a subject of controversy [11, 81, 93, 82, 80], and further theoretical and experimental efforts are needed to elucidate its character. Furthermore, very few experimental facts regarding the QH states at fillings $\nu = \pm 1$ are available. While it is clear that those states have an interacting nature and are of QHFM type [79], their order parameter has not been studied experimentally yet. Therefore, the relevance of the order-from-disorder mechanism proposed in Chapter 7 for the valley QHFM ordering remains unclear. The results presented in Chapters 6 and 7 thus should be viewed as a basis for more detailed studies.

Our analysis in Chapters 6 and 7 also poses several interesting questions and suggests several directions for future work. In particular, to better understand the transport properties at $\nu = 0$, we have to extend the spin-filtered edge model to include the effects of interactions. This will give rise to an unusual type of Luttinger liquid at the edge [98], which at low temperatures may have transport properties quite different from those obtained in Chapter 6 in the framework of non-interacting model. It would be especially interesting to explore the possibility of localization of

the edge Luttinger liquid by various disorder types.

The characteristic feature of the $\nu = 0$ state is non-local transport [149]. In principle, the non-local transport is consistent with the picture of the spin-polarized $\nu = 0$ state, where non-locality occurs naturally as a result of the counter-circulating edge states. However, the non-local transport can also arise due to an increased density of carriers at the edge, which may have a purely electrostatic origin [150]. Understanding the nature of the non-local signal may help to elucidate the character of the $\nu = 0$ state. Theoretically, it would be helpful to analyze the non-local transport effects for the spin-polarized $\nu = 0$, which can probably be done in the framework of the bulk-edge model considered in Section 6.5.

One of the main challenges in the study of the valley QHFM is to find tools to explore the nature of the valley order parameter. While the transport measurements [79] signal the opening of a gap, they do not provide any information regarding the order in the QHFM. In other QHFM systems the means to study order parameter orientation are provided by the possibility to independently couple to the two pseudospin or spin species. For instance, in QH bilayers [14] the two pseudospins correspond to the spatially separated quantum wells; one can attach separate contacts to the two wells [14], and measure the inter-layer current, which gives an insight into the properties of the pseudospin order parameter [76]. In graphene, however, such a measurement would be nearly impossible, because the two valley species reside in the same layer. Therefore, completely new ways to probe the valley order parameter are needed.

A whole new research direction is the study of the QHE in bilayer graphene. The LLs there [60], as well as the form of effective electron-electron interactions, are very different from those in monolayers. This may give rise to an interesting hierarchy of ferromagnetic QH states in bilayers, which are likely to exhibit multiple phase transitions as a function of external magnetic field and other parameters (e.g., electric field perpendicular to the bilayer plane, which is known to induce a gap in the spectrum [114]).

Looking beyond the QHE regime, one of the most important problems in the field

of graphene is understanding transport of disordered Dirac electrons. Theoretically, several models of disorder have been considered, which provided an explanation of certain experimentally observed transport characteristics [26]. However, the transport mechanism near the Dirac point, as well as the temperature dependence of the transport coefficients, remain a mystery, and further experimental and theoretical efforts are necessary.

Yet another interesting direction is to study the role of electron-electron interactions in transport phenomena. This topic remains largely unexplored, partially because of its complexity; another reason is the wealth of new single-particle phenomena in graphene, which needed to be understood before attacking the problem of interacting electrons.

Evidently, what we don't know about graphene by far exceeds what we have learned in the past four years. Only the future will tell us what other surprises electrons in graphene hold; however, there is little doubt that there will be many.

Bibliography

[1] A. Castro Neto, Francisco Guinea, and N. M. Peres. Drawing conclusinons from graphene. *Physics World*, 1986.

[2] K. von Klitzing anf G. Dorda and M. Pepper. New method for high-accuracy determination of the fine-structure based on quantized Hall resistance. *Physical Review Letters*, 45:494, 1980.

[3] E. McCann and V. I. Falko. Landau level degeneracy and quantum Hall effect in a graphite bilayer. *Physical Review Letters*, 96:086805, 2006.

[4] K. S. Novoselov, A. K. Geim, S. V. Morozov, D. Jiang, M. I. Katsnelson, I. V. Grigorieva, S. V. Dubonos, and A. A. Firsov. Two-dimensional gas of massless Dirac fermions in graphene. *Nature*, 438:197, 2005.

[5] Y. Zhang, Z. Jiang, J. P. Small, M. S. Purewall, Y.-W. Tan, M. Fazlollahi, J. D. Chudow, J. A. Jaszczak, H. L. Stormer, and P. Kim. Landau level splitting in graphene in high magnetic fields. *Physical Review Letters*, 96:136806, 2006.

[6] D. A. Abanin, K. S. Novoselov, U. Zeitler, P. A. Lee, A. K. Geim, and L. S. Levitov. Dissipative quantum Hall effect in graphene near the Dirac point. *Physical Review Letters*, 98:196806, 2007.

[7] D. A. Abanin and L. S. Levitov. Conformal invariance and shape-dependent conductance of graphene samples. *Physical Review B*, 78:035416, 2008.

[8] N. M. R. Peres, F. Guinea, and A. H. Castro Neto. *Physical Review B*, 73:125411, 2006.

[9] J. R. Williams, L. DiCarlo, and C. M. Marcus. Quantum Hall effect in graphene *p-n* junction. *Science*, 317:638, 2007.

[10] B. Ozyilmaz, P. Jarillo-Herrero, D. Efetov, D. A. Abanin, L. S. Levitov, and P. Kim. Electronic transport and quantum Hall effect in bipolar graphene *p-n-p* junction. *Physical Review Letters*, 99:166804, 2007.

[11] D. A. Abanin, P. A. Lee, and L. S. Levitov. Spin-filtered edge states and quantum Hall effect in graphene. *Physical Review Letters*, 74:235443, 2006.

[12] S. V. Iordanskii and A. E. Koshelev. Dislocations and localization effects in multivalley conductors. *JETP Letters*, 41:574, 1985.

[13] T. Ando, A. B. Fowler, and F. Stern. Electronic properties of two-dimensional systems. *Reviews of Modern Physics*, 54:1, 1982.

[14] S. Das Sarma and A. Pinczuk, editors. *Perspectives in the Quantum Hall Effect.* Wiley, New York, 1997.

[15] D. C. Tsui, H. L. Stormer, and A. C. Gossard. Two-dimensional magnetotransport in the extreme quantum limit. *Physical Review Letters*, 48:1559, 1982.

[16] R. B. Laughlin. Anomalous quantum Hall effect: an incompressible quantum fluid with fractionally charged excitations. *Physical Review Letters*, 50:1395, 1983.

[17] S. M. Girvin and A. H. MacDonald. Multicomponent quantum Hall systems: the sum of their parts and more. In S. Das Sarma and A. Pinczuk, editors, *Perspectives in quantum Hall effect.* Wiley, New York, 1997.

[18] Frank Wilczek. Magnetic flux, angular momentum, and statistics. *Physical Review Letters*, 48:1144, 1982.

[19] M. P. Lilly, K. B. Cooper, J. P. Eisenstein, L. N. Pfeiffer, and K. W. West. Evidence for an anisotropic state of two-dimensional electrons in high Landau levels. *Physical Review Letters*, 82:394, 1999.

[20] A. A. Koulakov, M. M. Fogler, and B. I. Shklovskii. Charge density wave in two-dimensional electron liquid in weak magnetic field. *Physical Review Letters*, 76:499, 1996.

[21] R. Moessner and J. T. Chalker. Exact results for interacting electrons in high Landau levels. *Physical Review B*, 54:5006, 1996.

[22] L. V. Butov. Cold exciton gases in coupled quantum well structures. *Journal of Physics: Condensed Matter*, 19:295202, 2007.

[23] D. Kahng and M. M. Atalla. *US Patent 3,102,230*, 1960.

[24] R. Dingle, H. L. Stormer, A. C. Gossard, and W. Wiegmann. Electron mobilities in modulation-doped semiconductor heterojunction superlattices. *Applied Physics Letters*, 33:665, 1978.

[25] K. S. Novoselov, A. K. Geim, S. V. Morozov, D. Jiang, Y. Zhang, and S. V. Dubonos. Electric field effect in atomically thin carbon films. *Science*, 306:666, 2004.

[26] A. H. Castro Neto, F. Guinea, N. M. Peres, K. S. Novoselov, and A. K. Geim. The electronic properties of graphene. *Reviews of Modern Physics, to appear.*

[27] K. I. Bolotin, K. J. Sikes, Z. Jiang, M. Klima, G. Fudenberg, J. Hone, P. Kim, and H. L. Stormer. Ultrahigh electron mobility in suspended graphene. *Solid State Communications*, page 351, 2008.

[28] M. I. Katsnelson, K. S. Novoselov, and A. K. Geim. Chiral tunneling and the Klein paradox in graphene. *Nature Physics*, 2:620, 2006.

[29] S. V. Morozov, K. S. Novoselov, M. Katsnelson, F. Schedin, D. Jiang, and A. K. Geim. Strong suppression of weak localization in graphene. *Physical Review Letters*, 97:016801, 2006.

[30] Y. Zhang, Y.-W. Tan, H. L. Stormer, and P. Kim. Experimental observation of quantum Hall effect and Berry's phase in graphene. *Nature*, 438:201, 2005.

[31] K. S. Novoselov, Z. Jiang, Y. Zhang, S. V. Morozov, H. L. Stormer, U. Zeitler, J. C. Maan, G. S. Boebinger, P. Kim, and A. K. Geim. Room-temperature quantum Hall effect in graphene. *Sicence*, 315:1379, 2007.

[32] A. K. Geim and K. S. Novoselov. The rise of graphene. *Nature Materials*, 6:183, 2006.

[33] R. B. Laughlin. Quantized Hall conductivity in two dimensions. *Physical Review B*, 23:5632, 1981.

[34] B. I. Halperin. Quantized Hall conductance, current-carrying edge states, and the existence of extended states in a two-dimensional disordered potential. *Physical Review B*, 25:2185, 1982.

[35] R. T. Morrison, R. N. Boyd, and R. K. Boyd. *Organic Chemistry.* Benjamin-Cummings, 1992.

[36] H. W. Kroto, J. R. Heath, S. C. O'Brien, R. F. Curl, and R. E. Smalley. C^{60}: Buckminsterfullerene. *Nature*, 318:162, 1985.

[37] S. Iijima. Helical microtubules of graphitic carbon. *Nature*, 354, 1991.

[38] M. Bockrath, D. H. Cobden, J. Lu, A. G. Rinzler, R. E. Smalley, L. Balents, and P. L. McEuen. Luttinger-liquid behavior in carbon nanotubes. *Nature*, 397:598, 1999.

[39] S. Iijima. Helical microtubules of graphitic carbon. *Nature*, 354, 1991.

[40] P. Jarillo-Herrero, J. Kong, H. S. V. van der Zant, C. Dekker, L. P. Kouwenhoven, and S. De Franceschi. Orbital Kondo effect in carbon nanotubes. *Nature*, 434:484, 2005.

[41] R. E. Peierls. Quelques properties typiques des corpses solides. *Annals of Henry Poincare Institute*, 5:177, 1935.

[42] L. D. Landau. Zur theorie der phasenumwandlungen. *Phys. Z. Sowjetunion*, 11:26, 1937.

[43] D. R. Nelson, T. Piran, and S. Weinberg. *Statistical Mechanics of Membranes and Surfaces.* World Scientific, Singapore, 2004.

[44] H. Petroski. *The Pencil: a history of design and circumstance.* Alfred Knopf, New York, 1989.

[45] Y. Ohashi, T. Koizumi, T. Yoshikawa, T. Hironaka, and T. Shiiki. Size effects in the in-plane electrical resistivity of very thin graphite crystals. *TANSO*, page 235, 1997.

[46] A. C. Ferrari, J. C. Meyer, V. Scardaci, C. Casiraghi, Michele Lazzeri, Francesco Mauri, S. Piscanec, Da Jiang, K. S. Novoselov, S. Roth, and A. K. Geim. Raman spectrum of graphene and graphene layers. *Physical Review Letters*, 97:187401, 2006.

[47] J. C. Meyer, A. K. Geim, M. I. Katsnelson, K. S. Novoselov, T. J. Booth, and S. Roth. The structure of suspended graphene sheets. *Nature*, 446:60, 2007.

[48] D. A. Abanin, P. A. Lee, and L. S. Levitov. Spin-filtered edge states and quantum Hall effect in graphene. *Physical Review Letters*, 74:235443, 2006.

[49] X. Wang, Y. Ouyang, X. Li, H. Wang, J. Guo, and H. Dai. Room-temperature all semiconducting sub-10nm graphene nanoribbon field-effect transistor. *Physical Review Letters*, 100:206803, 2008.

[50] C. Berger, Z. Song, T. Li, X. Li, A. Y. Ogbazghi, R. Feng, Z. Dai, A. N. Marchenkov, E. H. Conrad, P. N. First, and W. A. de Heer. Ultrathin epitaxial graphite: 2D electron gas properties and a route towards graphene-based nanoelectronics. *Journal of Physical Chemistry*, 108:19912, 2004.

[51] B. E. Kane. Silicon-based quantum computation. *Fortschritte der Physik*, 48:1023, 2000.

[52] R. Hanson, L. P. Kouwenhoven, J. R. Petta S. Tarucha, and L. M. K. Vandersypen. Spins in few-electron quantum dots. *Reviews of Modern Physics*, 79:1217, 2007.

[53] J. R. Petta, A. C. Johnson, J. M. Taylor, A. Yacoby, M. D. Lukin, C. M. Marcus, M. P. Hanson, and A. C. Gossard. Coherent manipulation of coupled electron spins in semiconductor quantum dots. *Science*, 309:2180, 2005.

[54] P. Strange. *Relativistic Quantum Mechanics.* Cambridge University Press, 1998.

[55] D. P. DiVincenzo and E. J. Mele. Self-consistent effective-mass theory for intralayer screening in graphite intercalation compounds. *Physical Review B*, 29:1685, 1984.

[56] N. Stander, B. Huard, and D. Goldhaber-Gordon. Observation of Klein tunneling in graphene *p-n* junctions. *available online as arXiv:08062319v1*, 2008.

[57] B. Huard, J. A. Sulpizio, N. Stander, K. Todd, B. Yang, and D. Goldhaber-Gordon. Transport measurements across a tunable potential barrier in graphene. *Physical Review Letters*, 98:236803, 2007.

[58] A. W. W. Ludwig, M. P. A. Fisher, R. Shankar, and G. Grinstein. Integer quantum Hall transition: an alternative approach and exact results. *Physical Review B*, 50:7526, 1994.

[59] P. A. Lee. Localized states in a *d*-wave superconductor. *Physical Review Letters*, 71:1887, 1993.

[60] E. McCann, K. Kechedzhi, Vladimir I. Falko, H. Suzuura, T. Ando, and B.L. Altshuler. Weak localisation magnetoresistance and valley symmetry in graphene. *Physical Review Letters*, 97:146805, 2006.

[61] P. M. Ostrovsky, I. V. Gornyi, and A. D. Mirlin. Electron transport in disordered graphene. *Physical Review B*, 74:235443, 2006.

[62] E. Mariani and F. von Oppen. Flexural phonons in free-standing graphene. *Physical Review Letters*, 100:076801, 2008.

[63] L. Brey and H. A. Fertig. Electronic states of graphene nanoribbons studied with the Dirac equation. *Physical Review B*, 73:235411, 2006.

[64] D. A. Abanin, P. A. Lee, and L. S. Levitov. Charge and spin transport at the quantum Hall edge of graphene. *Solid State Communications*, 143:77, 2007.

[65] L. A. Ponomarenko, F. Schedin, M. I. Katsnelson, R. Yang, E. H. Hill, K. S. Novoselov, and A. K. Geim. Chaotic Dirac billiard in graphene quantum dots. *Science*, 320:356, 2008.

[66] M. Fujita, K. Wakabayashi, K. Nakada, and K. Kusakabe. Peculiar localized states at zigzag graphite edge. *Journal of Physical Society of Japan*, 65:1920, 1996.

[67] M. Wimmer, I. Adagideli, S. Berber, D. Tomanek, and K. Richter. Spin currents in rough graphene nanoribbons: universal fluctuations and spin injection. *Physical Review Letters*, 100:177207, 2007.

[68] Young-Woo Son, M. V. Cohen, and S. G. Louie. Half-metallic graphene nanoribbons. *Nature*, 444:347, 2006.

[69] I. Martin. *Private communication*, 2008.

[70] T. Matsui, H. Kambara, Y. Niimi, K. Tagami, M. Tsukada, and H. Fukuyama. STS observation of Landau levels at graphite surfaces. *Physical Review Letters*, 94:226403, 2005.

[71] Y. Niimi, H. Kambara nd T. Matsui, D. Yoshioka, and H. Fukuyama. Real-space imaging of alternate localization and extension of quasi-two-dimensional electronic states at graphite surfaces in magnetic fields. *Physical Review Letters*, 97:236804, 2006.

[72] Y. Niimi, T. Matsui, H. Kambara, K. Tagami, M. Tsukada, and H. Fukuyama. Scanning tunneling microscopy and spectroscopy of the electronic local density of states of graphite surfaces near monoatomic step edges. *Physical Review B*, 73:085421, 2006.

[73] Y. Kobayashi, K. Fukui, T. Enoki, K. Kusakabe, and Y. Kaburagi. Observation of zigzag and armchair edges of graphite using scanning tunneling microscopy and spectroscopy. *Physical Review B*, 71:193406, 2005.

[74] V. Geringer, M. Liebmann, T. Echtermeyer, S. Runte, R. Ruckamp, M. Lemme, and M. Morgenstern. Intrinsic and extrinsic corrugation of monolayer graphene deposited on SiO_2. *Available online as arXiv:0806.1028v2*, 2008.

[75] Y. P. Shkolnikov, S. Misra, N. C. Bishop, E. P. De Poortere, and M. Shayegan. Observation of quantum Hall valley skyrmions. *Physical Review Letters*, 95:066809, 2005.

[76] K. Moon, H. Mori, K. Yang, S. M. Girvin, A. H. MacDonald, L. Zheng, D. Yoshioka, and S.-C. Zhang. *Physical Review B*, 51:5138, 1995.

[77] K. Yang, K. Moon, L. Zheng, A. H. MacDonald, S. M. Girvin, D. Yoshioka, and S.-C. Zhang. *Physical Review Letters*, 72:732, 1994.

[78] K. S. Novoselov, E. McCann, S. V. Morozov, V. I. Falko, M. I. Katsnelson, U. Zeitler, D. Jiang, F. Schedin, and A. K. Geim. Unconventional quantum Hall effect and Berry's phase of 2pi in bilayer graphene. *Nature Physics*, 2:177, 2006.

[79] Z. Jiang, Y. Zhang, H. L. Stormer, and P. Kim. The nature of quantum Hall states near the charge neutral Dirac point in graphene. *Physical Review Letters*, 99:106802, 2007.

[80] J. G. Checkelsky, Lu Li, and N. P. Ong. The zero-energy state in graphene in a high magnetic field. *Physical Review Letters*, 100:206801, 2008.

[81] K. Nomura and A. H. MacDonald. Quantum Hall ferromagnetism in graphene. *Physical Review Letters*, 96:256602, 2006.

[82] J.-N. Fuchs and P. Lederer. Spontaneous parity breaking of graphene in the quantum Hall regime. *Physical Review Letters*, 98:016803, 2007.

[83] J. Alicea and M. P. A. Fisher. *Physical Review B*, 74:075422, 2006.

[84] M. O. Goerbig, R. Moessner, and B. Doucot. Electron interactions in graphene in a strong magnetic field. *Physical Review B*, 74:161407, 2006.

[85] C.-H. Zhang and Yogesh N. Joglekar. Wigner crystal and bubble phases in graphene in the quantum Hall regime. *Physical Review B*, 75:245414, 2007.

[86] M. O. Goerbig and N. Regnault. Analysis of a SU(4) generalization of Halperin's wave function as an approach towards a SU(4) fractional quantum Hall effect in graphene sheets. *Physical Review B*, 75:241405, 2007.

[87] Vadim M. Apalkov and Tapash Chakraborty. The fractional quantum Hall states of Dirac electrons in graphene. *Physical Review Letters*, 97:126801, 2006.

[88] R. E. Girvin and editors S. M. Prange. *The quantum Hall effect.* Springer, New York, 1987.

[89] H. B. Heersche, P. Jarillo-Herrero, J. B. Oostinga, L. M. K. Vandersypen, and A. F. Morpurgo. *Nature*, 446:56, 2007.

[90] C. M. Marcus. *Private communication*, 2008.

[91] V. P. Gusynin and S. G. Sharapov. *Physical Review Letters*, 95:146801, 2005.

[92] R. Jackiw. Fractional charge and zero modes for planar systems in a magnetic field. *Physical Review D*, 29:2375, 1984.

[93] V.P. Gusynin, V.A. Miransky, S.G. Sharapov, and I.A. Shovkovy. Excitonic gap, phase transition, and quantum Hall effect in graphene. *Physical Review B*, 74:195429, 2006.

[94] V. P. Gusynin, V. A. Miransky, and I. A. Shovkovy. *Physical Review Letters*, 73:3499, 1994.

[95] D. V. Khveshchenko. *Physical Review Letters*, 87:206401, 2001.

[96] D. V. Khveshchenko. *Physical Review Letters*, 87:246802, 2001.

[97] V. P. Gusynin, V. A. Miransky, S. G. Sharapov, and I. A. Shovkovy. Edge states, mass and spin gaps, and quantum Hall effect in graphene. *Physical Review B*, 77:205409, 2008.

[98] H. A. Fertig and L. Brey. Luttinger liquid at the edge of undoped graphene in a strong magnetic field. *Physical Review Letters*, 97:116805, 2006.

[99] E. Shimshoni, H. A. Fertig, and G. V. Pai. Onset of an insulating zero-plateau quantum Hall state in graphene. *Available online as arXiv:0807.2867*, 2008.

[100] G. Liu, J. Valesco Jr, W. Bao, and C. N. Lau. Fabrication of graphene *p-n-p* junctions with contactless top gates. *Applied Physics Letters*, 92:203103, 2008.

[101] D. A. Abanin and L. S. Levitov. Quantized transport in graphene *p-n* junctions in magnetic field. *Science*, 317:641, 2007.

[102] Csaba Toke and Jainendra K. Jain. SU(4) composite fermions in graphene: new fractional quantum Hall states. *Physical Review B*, 75:245440, 2007.

[103] R. W. Rendell and S. M. Girvin. Hall voltage dependence on inversion-layer geometry in the quantum Hall-effect regime. *Physical Review B*, 23:6610, 1981.

[104] A. M. Dykhne and I. M. Ruzin. *Physical Review B*, 50:2369, 1994.

[105] C. W. Beenakker. Random-matrix theory of quantum transport. *Reviews of Modern Physics*, 69:731, 1997.

[106] H. J. Lippmann and R. Kuhrt. *Z. Naturf.*, 13:462, 1958.

[107] H. H. Jensen and H. Smith. *Journal of Physics C*, 5:2867, 1972.

[108] A. M. Dykhne. *Soviet Physics JETP*, 32:63, 1971.

[109] S. M. Murzin, M. Weiss, A. G. Jansen, and K. Eberl. *Physical Review B*, 66:233314, 2002.

[110] C. P. Burgess and B. P. Dolan. *Physical Review B*, 76:113406, 2007.

[111] J. Williams, D. A. Abanin, L. DiCarlo, L. S. Levitov, and C. M. Marcus. Two-terminal conductance of quantum Hall graphene samples. *To be published*, 2008.

[112] C. W. J. Beenakker and H. van Houten. In H. Ehrenreich and D. Turnbull, editors, *Solid State Physics*, number 44, page 1. Academic, New York, 1991.

[113] E. McCann. Asymmetry gap in the electronic band structure of bilayer graphene. *Physical Review B*, 74:161403, 2006.

[114] Eduardo V. Castro, K. S. Novoselov, S. V. Morozov, N. M. R. Peres, J.M.B. Lopes dos Santos, Johan Nilsson, F. Guinea, A. K. Geim, and A. H. Castro Neto. Biased bilayer graphene: semiconductor with a gap tunable by electric field effect. *Physical Review Letters*, 99:216802, 2007.

[115] L.Gradstein and M. Ryzhik. *Tables of Integrals, Series and Producst.* Academic, San Diego, 2002.

[116] G. Giovanetti et al. *Available online as arXiv:0802.2267*, 2008.

[117] J. R. WIlliams, D. A. Abanin, L. S. Levitov, and C. M. Marcus. *To appear*, 2008.

[118] J. Martin, N. Akerman, G. Ulbricht, T. Lohmann, J. H. Smet, K. von Klitzing, and A. Yacoby. Observation of electron-hole puddles in graphene using a scanning single electron transistor. *Nature Physics*, 4:086805, 2006.

[119] V. V. Cheianov, V. Fal'ko, and B. L. Altshuler. Veselago lens for electrons: focusing and caustics in graphene p-n junctions. *Science*, 315:1252, 2007.

[120] R. J. Haug. *Semicond. Sci. Technol.*, 8:131, 1993.

[121] R. J. Haug, A. H. MacDonald, P. Streda, and K. von Klitzing. *Physical Review Letters*, 61:2797, 1988.

[122] S. Washburn, A. B. Fowler, H. Schmid, and D. Kern. Quantized Hall effect in the presence of backscattering. *Physical Review Letters*, 61:2801, 1988.

[123] L. P. Kouwenhoven, B. J. van Wees, N. C. van der Vaart, C. J. Harmans, C. E. Timmering, and C. T. Foxon. Selective population and detection of edge channels in the fractional quantum Hall regime. *Physical Review Letters*, 64:685, 1990.

[124] H. U. Baranger and P. A. Mello. *Physical Review Letters*, 73:142, 1994.

[125] M Buttiker. *Physical Review B*, 38:12724, 1988.

[126] Ya. M. Blanter and M. Buttiker. *Physics Reports*, 2000.

[127] A. V. Khaetskii, V. I. Falko, and G. W. Bauer. *Physical Review B*, 50:4571, 1994.

[128] D. V. Savin and H.-J. Sommers. *Physical Review B*, 73:081307, 2006.

[129] K. E. Nagaev. *Physics Letters A*, 169:103, 1992.

[130] S. Oberholzer, E. V. Sukhorukov, C. Strunk, C. Schnenberger, T. Heinzel, and M. Holland. Shot noise by quantum scattering in chaotic cavities. *Physical Review Letters*, 86:2114, 2001.

[131] V. V. Cheianov and V. I. Falko. Selective transmission of Dirac electrons and ballistic magnetoresistance of *n-p* junctions in graphene. *Physical Review B*, 74:041403, 2006.

[132] R. Ilan, N. R. Cooper, and A. Stern. *Physical Review B*, 73:235333, 2006.

[133] C. L. Kane and E. J. Mele. Topological order and the quantum spin Hall effect. *Physical Review Letters*, 95:146802, 2005.

[134] C. L. Kane and E. J. Mele. Quantum spin Hall effect in graphene. *Physical Review Letters*, 95:226801, 2005.

[135] H. Min, J. E. Hill, N. A. Sinitsyn, B. R. Sahu, L. Kleinman, and A. H. MacDonald. Intrinsic and Rashba spin-orbit interactions in graphene sheets. *Physical Review B*, 74:165310, 2006.

[136] D. A. Abanin, P. A. Lee, and L. S. Levitov. Order from disorder in graphene quantum Hall ferromagnet. *Available online as arXiv:cond-mat/0611062*, 2006.

[137] C. L. Kane and E. G. Mele. *Physical Review Letters*, 78:1932, 1997.

[138] A. Morpurgo and F. Guinea. Intervalley scattering, long-range disorder, and effective time reversal symmetry breaking in graphene. *Physical Review Letters*, 97:196804, 2006.

[139] A. Aharony. *Physical Review B*, 18:3328, 1978.

[140] D. E. Feldman. *Journal of Physics A*, 31:177, 1998.

[141] J. Minchau and R. A. Pelcovits. *Physical Review B*, 32:3082, 1985.

[142] J. Wehr, A. Niederberger, L. Sanchez-Palencia, and M. Lewenstein. Disorder versus the Mermin-Wagner-Hohenberg effect: from classical spin systems to ultracold atomic gases. *Physical Review B*, 74:224448, 2006.

[143] A. I. Larkin. Effect of inhomogeneities on the structure of the mixed state of superconductors. *JETP*, 31:784, 1970.

[144] Y. Imry and S. K. Ma. Random-field instability of the ordered state of continuous symmetry. *Physical Review Letters*, 35:1399, 1975.

[145] S. Hikami and T. Tsuneto. *Progress in Theoretical Physics*, 63:387, 1980.

[146] P. L. Kapitza. *Zh. Exp. Teor. Fiz.*, 21:588, 1951.

[147] L. D. Landau and E. M. Lifshitz. *Mechanics.* Reed Educational and Pofessional Publ. Ltd, 2002.

[148] R. L. Stratonovich and Yu. M. Romanovsky. *Nauch. Dokl. Vys. Shk., ser. fiz.-mat.*, 3:221, 1958.

[149] A. K. Geim. *Private communication*, 2008.

[150] P. G. Silvestrov and K. B. Efetov. Charge accumulation at the boundaries of a graphene strip induced by a gate voltage: electrostatic approach. *Physical Review B*, 77:155436, 2008.